

**UNIVERSIDADE FEDERAL DE JUIZ DE FORA
INSTITUTO DE CIÊNCIAS EXATAS / FACULDADE DE ENGENHARIA
PROGRAMA DE PÓS-GRADUAÇÃO EM MODELAGEM
COMPUTACIONAL**

Johnny Moreira Gomes

Using delay differential equations in models of cardiac electrophysiology

Juiz de Fora

2019

Johnny Moreira Gomes

Using delay differential equations in models of cardiac electrophysiology

Tese apresentada ao Programa de Pós-graduação em Modelagem Computacional, da Universidade Federal de Juiz de Fora como requisito parcial à obtenção do grau de Doutor em Modelagem Computacional.

Advisor: Prof. Ph.D. Rodrigo Weber dos Santos

Co-Advisor: Prof. Ph.D. Elizabeth M. Cherry

Co-Advisor: Prof. Ph.D. Marcelo Lobosco

Juiz de Fora

2019

Ficha catalográfica elaborada através do programa de geração automática da Biblioteca Universitária da UFJF, com os dados fornecidos pelo(a) autor(a)

Gomes, Johnny Moreira.

Using delay differential equations in models of cardiac electrophysiology / Johnny Moreira Gomes. -- 2019.

112 p. : il.

Orientador: Rodrigo Weber dos Santos

Coorientadores: Elizabeth Cherry, Marcelo Lobosco

Tese (doutorado) - Universidade Federal de Juiz de Fora, ICE/Engenharia. Programa de Pós-Graduação em Modelagem Computacional, 2019.

1. Cardiac modeling. 2. Cardiac arrhythmia mechanisms. 3. Delay differential equations. 4. Electrical alternans. I. dos Santos, Rodrigo Weber, orient. II. Cherry, Elizabeth, coorient. III. Lobosco, Marcelo, coorient. IV. Título.

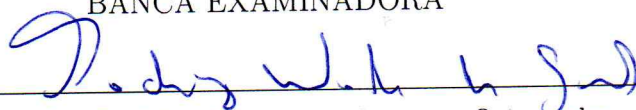
Johnny Moreira Gomes

Utilizando Equações Diferenciais com Atraso em Modelos de Eletrofisiologia
Cardíaca

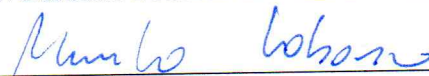
Tese apresentada ao Programa de Pós-graduação em Modelagem Computacional, da Universidade Federal de Juiz de Fora como requisito parcial à obtenção do grau de Doutor em Modelagem Computacional.

Aprovada em 19 de novembro de 2019.

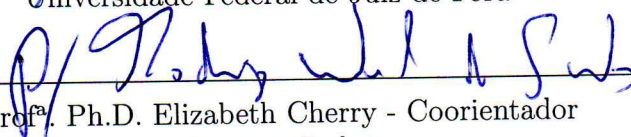
BANCA EXAMINADORA



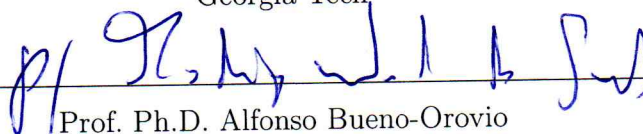
Prof. D.Sc. Rodrigo Weber dos Santos - Orientador
Universidade Federal de Juiz de Fora



Prof. D.Sc. Marcelo Lobosco - Coorientador
Universidade Federal de Juiz de Fora



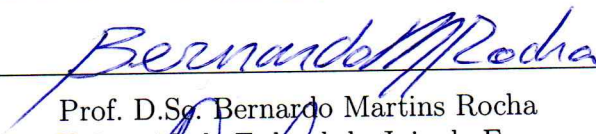
Prof^a. Ph.D. Elizabeth Cherry - Coorientador
Georgia Tech



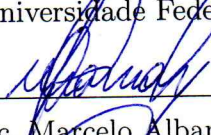
Prof. Ph.D. Alfonso Bueno-Orovio
University of Oxford



Prof. D.Sc. Abimael Fernando Dourado Loula
Laboratório Nacional de Computação Científica



Prof. D.Sc. Bernardo Martins Rocha
Universidade Federal de Juiz de Fora



Prof. D.Sc. Marcelo Albano Moret Simões Gonçalves
Universidade do Estado da Bahia

*I dedicate this work to God and
my beloved family.*

ACKNOWLEDGMENTS

First, I would like to thank God for providing me the necessary skills and perseverance to develop this work. I would also like to thank my beloved family for all the support. I also thank my advisors Rodrigo, Elizabeth, and Marcelo, for all the hard work and dedication to assisting me in this project. Finally, I thank the grant institutions that contributed to this research: FAPEMIG, CAPES, CNPq, Rochester Institute of Technology, and UFJF.

*'Our virtues and our failings are
inseparable, like force and matter.
When they separate, man is no
more.'*

Nikola Tesla

RESUMO

Em fisiologia cardíaca, *alternans* elétrica é um fenômeno caracterizado pela alternância entre potenciais de ação longos e curtos que dá origem a complexos comportamentos espaço-temporais em tecido. Experimentos e medições clínicas indicam que *alternans* pode ser um precursor de perigosas arritmias, como fibrilação ventricular ou morte súbita. Apesar da importância do *alternans* no estudo de doenças cardíacas, muitos modelos matemáticos para a eletrofisiologia de células cardíacas não são capazes de reproduzir este fenômeno. Como um potencial remédio para esta deficiência, introduzimos curtos atrasos de tempo em algumas formulações de modelos preexistentes para células cardíacas que são baseados em Equações Diferenciais Ordinárias (EDOs). Vários processos em células cardíacas envolvem atrasos de sensibilidade e de resposta a mudanças em variáveis fisiológicas. Além disso, equações diferenciais com atraso (DDEs) são conhecidas por dar origem a complexas propriedades dinâmicas em modelos matemáticos. Em modelagem biológica, DDEs têm sido aplicadas em epidemiologia, dinâmica populacional, imunologia e redes neurais. Portanto, DDEs podem representar mecanismos que resultam em dinâmicas complexas tanto no nível celular, quanto no nível do tecido. Nesta tese, propomos formulações baseadas em DDEs para modelos de canais iônicos descritos pelo formalismo de Hodgkin-Huxley. Tais formulações são capazes de induzir *alternans* em simulações celulares envolvendo vários modelos encontrados na literatura. Nós também mostramos que essas modificações podem desestabilizar e quebrar ondas espirais em simulações bidimensionais de propagação elétrica, o que é típico de fibrilação cardíaca. Entretanto, as formulações propostas introduzem novos desafios computacionais devido à necessidade de armazenar e recuperar valores passados de variáveis. Deste modo, nós apresentamos novos métodos numéricos para superar tais desafios e permitir a eficiente simulação de modelos baseados em DDEs no nível do tecido cardíaco. Os métodos propostos foram capazes de diminuir o uso de memória em até 95% em comparação aos algoritmos largamente utilizados na solução numérica de DDEs. Assim, os novos modelos baseados em DDEs e os eficientes métodos numéricos propostos nesta tese contribuem

para o estudo de arritmias cardíacas fatais através de modelagem computacional.

Palavras-chave: Modelagem Cardíaca. Mecanismos de Arritmia Cardíaca. Equações Diferenciais com Atraso. Alternans Elétrica.

ABSTRACT

In cardiac physiology, electrical alternans is a phenomenon characterized by long-short alternations in the action potential duration of cardiac myocytes that give rise to complex spatiotemporal dynamics in tissue. Experiments and clinical measurements indicate that alternans can be a precursor of life-threatening arrhythmias, such as cardiac fibrillation. Despite the importance of alternans in the study of cardiac disease, many mathematical models developed to describe cardiac electrophysiology at the cellular level are not able to produce this phenomenon. As a potential remedy to this deficiency, we introduce short time-delays in some formulations of existing cardiac cell models that are based on Ordinary Differential Equations (ODEs). Many processes within cardiac cells involve delays in sensing and responding to changes. In addition, delay differential equations (DDEs) are known to give rise to complex dynamical properties in mathematical models. In biological modeling, DDEs have been applied to epidemiology, population dynamics, immunology, and neural networks. Therefore, DDEs can potentially represent mechanisms that result in complex dynamics both at the cellular level and at the tissue level. In this thesis, we propose DDE-based formulations for ion channel models based on the Hodgkin-Huxley formalism that can induce alternans in single-cell simulations in many models found in the literature. We also show that these modifications can destabilize spiral waves and produce spiral breakups in two-dimensional simulations, which is a typical model of cardiac fibrillation. However, the new DDE-based formulations introduce new computational challenges due to the need for storing and retrieving past values of variables. Therefore, we present novel numerical methods to overcome these challenges and enable efficient DDE-based studies at the tissue level in standard computational environments. We find that the proposed methods decrease memory usage by up to 95% in cardiac tissue simulations compared to straightforward history management algorithms available in widely used DDE solvers.

Keywords: Cardiac Modeling. Cardiac Arrhythmia Mechanisms. Delay Differential Equations. Electrical Alternans.

TABLE OF CONTENTS

List of Abbreviations.....	20
1 Introduction.....	21
1.1 Objectives	23
1.2 Summary	23
2 Cardiac Electrophysiology.....	25
2.1 Electrophysiology of Cardiac Cells	26
2.1.1 <i>The action potential (AP)</i>	26
2.1.1.1 <i>Threshold potential</i>	27
2.1.1.2 <i>Refractory period</i>	27
2.1.2 <i>Modeling the membrane</i>	29
2.1.3 <i>Ion channel models</i>	31
2.1.3.1 <i>Markov-based Models</i>	32
2.1.4 <i>Calcium handling</i>	33
2.2 Electrical alternans	34
2.3 Restitution analysis	36
2.4 Tissue Models	37
3 Methods.....	41
3.1 Methods for ODE-based models	41
3.1.1 <i>Forward Euler method (FE)</i>	41
3.1.2 <i>Rush-Larsen method (RL)</i>	42
3.2 DDE-based formulations for ion channels	42
3.3 Methods for DDE-based single cell models	44
3.3.1 <i>Forward Euler adaptation for a DDE</i>	44
3.3.2 <i>Rush-Larsen method for DDE-based cardiac models</i>	45
3.4 Methods for wave propagation in tissue	47
3.4.1 <i>Initiation of spiral waves in 2D</i>	48
3.5 Handling historical data in DDE-based simulations	49

3.5.1	<i>Simple linear interpolation algorithm (SLIA)</i>	50
3.5.2	<i>Adaptive history management algorithm (AHMA)</i>	50
3.5.2.1	<i>Memory management implementations</i>	52
3.6	Parallel implementations	54
3.6.1	<i>OpenMP implementations</i>	55
3.6.2	<i>GPU implementations</i>	55
3.7	Metrics	57
3.7.1	<i>APD restitution analysis</i>	57
3.7.2	<i>Period distributions</i>	58
3.7.3	<i>Spiral wave tip tracking</i>	58
3.7.4	<i>Error calculation</i>	60
3.7.5	<i>Measuring performance</i>	61
4	Results	62
4.1	DDE-induced alternans in single cell models	62
4.1.1	<i>Alternans restoration in Hodgkin-Huxley-based models</i>	62
4.1.1.1	<i>DDE implementations for the Fox et al. model</i>	62
4.1.1.2	<i>Adding delays to other five HH-based models</i>	68
4.1.2	<i>DDE-induced alternans in cardiac myocyte models</i>	76
4.1.2.1	<i>ten Tusscher et al. model (2004)</i>	76
4.1.2.2	<i>Grandi et al. model (2010)</i>	82
4.2	DDE-based simulations of cardiac tissue	86
4.2.1	<i>History management algorithms in ring simulations</i>	86
4.2.2	<i>Spiral wave dynamics in 2D</i>	88
4.2.3	<i>Computational performance in 2D</i>	91
4.2.4	<i>DDE-induced alternans and spiral breakup</i>	93
5	Discussion	96
5.1	DDE-induced alternans and spiral wave breakup	96
5.2	Methods for DDE-based tissue simulations	97
5.3	Limitations and future work	98
5.3.1	<i>Numerical Methods</i>	98
5.3.2	<i>DDEs for cardiac models</i>	99

6	Conclusion.....	100
---	-----------------	-----

LIST OF FIGURES

2.1	Basic structure of the heart: chambers and blood flow. Adapted from Hall - Guyton (2006).	25
2.2	Basic structure of a cell membrane and a voltage-gated ion channel. Adapted from Campos (2008).	26
2.3	Phases of the action potential from a typical nonpacemaker heart cell (Saad <i>et al.</i> , 2015).	27
2.4	Plot of a membrane potential recording where stimulus currents fail to initiate a second action potential during the refractory period, which is highlighted by a gray dashed line (adapted from Commons (2007)).	28
2.5	Schematic of the mechanism of reentry in a heterogeneous media with an obstacle (adapted from Timour <i>et al.</i> (2012)).	29
2.6	Representation of the neuron membrane as an electrical circuit.	30
2.7	Three-state Markov model for a hypothetical ion channel.	33
2.8	Markov model for the Na^+ channel described in the model for the mouse ventricular action potential proposed by Bondarenko <i>et al.</i> (2004).	33
2.9	Schematic diagram of the ion fluxes described by the ten Tusscher - Panfilov (2006) mathematical model of the human ventricular myocyte.	34
2.10	Occurrence of alternans at a fast pacing rate in a cardiac fiber (adapted from Garzón <i>et al.</i> (2011)): (a) action potentials with constant duration for a pacing period of 270 ms; (b) action potentials with period-doubling for a constant pacing period of 250 ms.	35
2.11	Measurements for performing a restitution analysis: action potential duration (APD), diastolic interval (DI) and cycle length (CL).	36
2.12	Relation between a steep restitution curve and period-doubling (adapted from Fox <i>et al.</i> (2002)): (A) bifurcation diagram, where APD is plotted as a function of the basic cycle length (BCL); (B) restitution plot of APD as a function of the diastolic interval (DI) alongside with a solid line with a slope of 1.	37

2.13	Voltage snapshots of a 2D simulation of the Karma (1994) model. A single spiral wave (a) is destabilized by electrical alternans (b) and breaks up into multiple spiral segments (c) that evolve into spiral turbulence (d). Image adapted from Byrne <i>et al.</i> (2015)	40
3.1	S1-S2 protocol for initiating a spiral wave in 2D.	49
3.2	Values present in the history (blue dots) and newly computed value y_{n+1} with $ y_{n+1} - y_k > \phi_{push}$. The adaptive algorithm decides if y_k can be approximated with sufficient accuracy by a linear interpolation of y_l and y_{n+1}	50
3.3	Algorithm illustrating how the AHMA handles local histories updates.	51
3.4	Schematic of a DDE-based wave propagation simulation on a cable using the Dynamic Array Implementation (DAI) for the Adaptive History Management Algorithm (AHMA).	54
3.5	Microarchitecture of the NVIDIA Pascal (NVIDIA, 2016) streaming multiprocessor, including 64 single-precision units (cores), 16 special function units (SFUs), and 32 double-precision units (adapted from NVIDIA (2016)).	56
3.6	NVIDIA CUDA programming model and blocks scheduling (adapted from NVIDIA (2016)).	57
3.7	Two-dimensional simulation of 5 seconds of spiral wave activity from the model by ten Tusscher <i>et al.</i> (2004): (a) snapshot of membrane potentials at $t = 5$ s and (b) the obtained period distribution across the entire domain.	59
3.8	Spiral tip trajectories from simulations of the FitzHugh-Nagumo system (FitzHugh, 1961) with varying parameter β (adapted from Foulkes - Biktashev (2010)).	60
4.1	(A) Action potentials from the model by Fox <i>et al.</i> (2002) for 10s at a constant cycle length of 180 ms: original model versus version with doubled \bar{g}_{Kr} . (B) Bifurcation diagrams of the original Fox <i>et al.</i> (2002) model and of the version with alternans suppressed by doubling \bar{g}_{Kr}	63

4.2	Alternans promotion by introducing delays into the f and d gates of the Fox et al. model: (A,E) bifurcation diagrams from the original Fox et al. models against alternans-suppressed version with DDE implementation for the f gate (A) and the d gate (E); (B,F) steady-state successive action potentials at a cycle length of 180 ms; (C,G) I_{Ca} corresponding to the successive action potentials in panels (B) and (F); (D,H) gating variables from the original and alternans-suppressed versions compared to the versions using delays of 15 ms and 12 ms, respectively.	64
4.3	Alternans magnitude (A) and CL range exhibiting alternans (B) for delaying f , d , and f_{Ca} gates in Fox et al. model with doubled \bar{g}_{Kr} . The gray lines indicate the values for the original model.	65
4.4	Alternans magnitude (A) and CL range exhibiting alternans (B) for delaying groups of I_{Ca} gates in Fox et al. model with doubled \bar{g}_{Kr} . The gray lines indicate the values for the original model.	66
4.5	Bifurcation diagrams for the Fox <i>et al.</i> (2002) model comparing the original version with the an alternans-suppressed suppressed version using the DDE formulation for (A) I_{Ca} inactivation gate f ; (B) I_{Ca} activation gate d ; (C) I_{Ca} calcium-dependent inactivation gate f_{Ca} ; (D) I_{K1} gate K_1^∞ ; (E) I_{Na} gates m , h and j	66
4.6	Robustness of the DDE-based formulation to promote alternans for different alternans suppression methods. Delays were added to the f gate in the following alternans-suppressed versions: (A) doubled \bar{g}_{Kr} ; (B) \bar{g}_{to} increased by a factor of 1.22; (C) \bar{g}_{Ks} increased by a factor of 25; (D) \bar{g}_{K1} increased by a factor of 1.2; (E) \bar{g}_{Kp} increased by a factor of 9; and (F) doubled \bar{g}_{Na}	67
4.7	(a) Action potentials from the Noble model with a cycle length of 200 ms: original version (solid) and alternans suppressed version ($\bar{g}_{K2} \times 1.25$, dashed). (b) Bifurcation plots for the original and alternans-suppressed versions. (c) Action potentials for the original and suppressed version with a DDE for $K_{1\infty}$, with CL = 210 ms. (d) Bifurcation plots for the original Noble model and suppressed version with a DDE for $K_{1\infty}$	69

4.8	Alternans properties of the suppressed Noble model with a DDE for the $K_{1\infty}$ variable. (a) Maximum alternans magnitude as a function of delay. (b) Alternans CL range as a function of delay.	70
4.9	(a) Bifurcation plots for the Beeler-Reuter model using DDEs for the gating variables f and x_1 . (b) Maximum alternans magnitude as a function of delay. (c) Alternans CL range as a function of delay.	71
4.10	(a) Bifurcation plots of the alternans-suppressed mLR1 model with DDE formulations for the gating variable f , gating variable x , and gating variables f and d together. (b) Maximum alternans magnitude as a function of delay. (c) Alternans CL range as a function of delay.	72
4.11	(a) Bifurcation plots of the alternans-suppressed Li-Rudy model with delayed gates i and $K_{1\infty}$. (b) APs from the original model and the alternans-suppressed version with delayed $K_{1\infty}$ ($CL = 245$ ms) using a delay of 8 ms, which produced AP shapes very close to those of the original model. (c) Maximum alternans magnitude as a function of delay. (d) Alternans CL range as a function of delay. Action potential blocks occur when delaying $K_{1\infty}$ by values greater than 9 ms.	73
4.12	Bifurcation plots of the alternans-suppressed Tusscher - Panfilov (2006) model by using DDE formulations for f and for both f and f_2	74
4.13	Membrane potential, calcium inactivation gating variable f and calcium current during alternans in the suppressed Beeler-Reuter model with DDE for f , using $\delta = 20$ ms and $CL = 200$ ms.	75
4.14	(A) CL versus APD curves for the three original parameter settings of the ten Tusscher <i>et al.</i> (2004) model. (B) Action potential blocks that occur in the endocardial setting of the ten Tusscher <i>et al.</i> (2004) model for $CL = 250$ ms.	77
4.15	CL versus APD curves for assessing the APD sensitivity to ion current maximum conductivities. Each curve results from a single modification in the epicardial cell model by ten Tusscher <i>et al.</i> (2004): (A) Modifications to potassium maximum conductivities; (B) modifications to sodium and calcium maximum conductivities.	77

4.16	Delaying groups of gating variables in the ten Tusscher <i>et al.</i> (2004) model: (A) APD x CL diagrams of scenarios with DDEs applied to gates of the I_{Kr} current (x_{r1} and x_{r2}), the $I_{Ca,L}$ current (d , f , and f_{Ca}), and the I_{Na} current (m , h , and j); (B) action potentials exhibiting moderate steady-state alternans when sodium inactivation gates are delayed (CL = 224 ms).	79
4.17	Bifurcation diagrams from experiments associating delayed sodium inactivation gates with the use of delays for $I_{Ca,L}$ gates (A), I_{Kr} gates (B), and I_{to} gates (C) in the ten Tusscher <i>et al.</i> (2004) model. Action potentials from selected cases exhibiting steady-state alternans using stimulus periods of 242 ms (D), 252 ms (E), and 275 ms (F).	80
4.18	Original ten Tusscher <i>et al.</i> (2004) model for epicardial cells versus version with delayed sodium inactivation gates.	81
4.19	Bifurcation diagrams from DDE-based experiments with the ten Tusscher <i>et al.</i> (2004) model: version with delayed calcium gates d and f versus version with DDE implementation for sodium gates h and j and calcium gates d and f .	82
4.20	(A) CL versus APD curves for both original settings of the Grandi <i>et al.</i> (2010) model. (B) Action potential blocks and chaos that occur in the original setting of the Grandi <i>et al.</i> (2010) model, despite constant pacing at $CL = 252$ ms and a small integration step of 10^{-4} ms.	83
4.21	CL versus APD curves for assessing the APD sensitivity to maximum ion current conductivities of the Grandi <i>et al.</i> (2010) model (epicardial cell version): (A) Modifications to potassium maximum conductivities; (B) modifications to sodium and calcium maximum conductivities.	84
4.22	APD versus CL curves from experiments delaying groups of gating variables in the Grandi <i>et al.</i> (2010) model.	85
4.23	DDE-induced alternans from experiments delaying various combinations of gates in the Grandi <i>et al.</i> (2010) model. Bifurcation diagrams from experiments applying the DDE formulation to: (A) $I_{Na,f}$ and $I_{Ca,L}$ gates; (B) $I_{Na,f}$ gates and the I_{K1} activation gate; and (C) $I_{Na,f}$ and $I_{to,f}$ gates. Action potentials from selected cases exhibiting steady-state alternans using stimulus periods of 367 ms (D), 330 ms (E), and 254 ms (F).	85

4.24	<p>Snapshots of membrane potentials from simulations of a 30 cm × 30 cm tissue using of the Fox <i>et al.</i> model and a stable spiral wave as initial condition, in four different scenarios: (A) the original model; (B) the model with doubled g_{Kr}; (C) the model with doubled g_{Kr} and the f gate delayed by 20 ms; and (D) the model with doubled g_{Kr}, the f gate delayed by 20 ms, and the d gate delayed by 12 ms. The spiral wave tip trajectory is shown in white whenever there is a single spiral wave.</p>	89
4.25	<p>Period distributions across a 2D tissue for different configurations of the Fox <i>et al.</i> model: (a) DDE implementation for the f gate versus non-DDE versions and case D; (b) DDE implementation for the d gate versus non-DDE versions and case D.</p>	90
4.26	<p>Snapshots of membrane potentials from simulations of a 24 cm × 24 cm tissue using the ten Tusscher <i>et al.</i> (2004) model and a stable spiral wave as initial condition, in four different scenarios: (A) the original model for epicardial cells; (B) the model with the h gate delayed by 2 ms and the j gate delayed by 0.5 ms; (C) the model with the x_{r2} gate delayed by 15 ms; and (D) the model with the h gate delayed by 2 ms, the j gate delayed by 0.5 ms, and the x_{r2} gate delayed by 15 ms. The spiral wave tip trajectory is shown in white whenever there is a single spiral wave.</p>	94
4.27	<p>Period distributions obtained from simulations of the four scenarios presented in Figure 4.26. The period information was collected from $t = 5$ s to $t = 10$ s of each simulation.</p>	95

LIST OF TABLES

4.1	Number of values per node history (NVPNH) in simulations of a 12 cm ring using the Fox <i>et al.</i> model with delays used for different gating variables. Gating variable choices included the L-type calcium current activation gate d , the L-type calcium current voltage-dependent inactivation gate f , the combination of d and f , and the three gates of the sodium current with the same delay. The parameters Δt_{hist} , ϕ_{push} and ϕ_{lin} were chosen based on achieving a 2% tolerance for the gating variable and conduction velocity errors with respect to the reference solution. The highlighted numbers indicate the most memory-efficient results of each scenario in terms of maximum NVPNH, although the AHMA always exhibits the lowest average memory use.	87
4.2	Computation times and history memory usage of different memory management implementations for simulating 1 second of electrical activity of the Fox <i>et al.</i> model in a 2D tissue. The alternans-suppressed version with DDE implementation for the f and d gates was used in order to assess the algorithms in a situation of sustained chaos.	91

List of Abbreviations

AHMA	Adaptive History Management Algorithm
AP	Action Potential
API	Application Programming Interface
APD	Action Potential Duration
BCL	Basic Cycle Length
CL	Cycle Length
CPU	Central Processing Unit
DAI	Dynamic Array Implementation
DI	Diastolic Interval
DDE	Delay Differential Equation
FE	Forward Euler
GPU	Graphics Processing Unit
HH	Hodgkin-Huxley
IVP	Initial Value Problem
LLI	Linked List Implementation
MC	Markov Chain
ODE	Ordinary Differential Equation
RK	Runge-Kutta
RL	Rush-Larsen
SCAI	Simple Contiguous Array Implementation
SFU	Special Function Unit
SLIA	Simple Linear Interpolation Algorithm
SMPI	Shared Memory Pool Implementation

1 Introduction

Computational modeling of the electrical activity of the heart is an important tool for understanding heart function (Martin, 1968), since the involved mechanisms are highly complex and span multiple scales of space and time. After the publication of the groundbreaking mathematical model for excitable cells by Hodgkin - Huxley (1952), Noble (1962) published the first model for the cardiac action potential and pacemaker rhythm of Purkinje fibers. Since then, models of cardiac electrophysiology have constantly evolved, both in accuracy and complexity. Those models have been applied to reproduce different kinds of cardiac disease, *e.g.* arrhythmias and fibrillation (Fenton *et al.*, 2002; ten Tusscher - Panfilov, 2006; Göktepe *et al.*, 2009), myocardial fibrosis (Kazbanov *et al.*, 2016) and ischemia (Dutta *et al.*, 2017). They have also been applied to simulate the effects of drugs on the myocytes electrophysiology and have aided the development of pharmacological therapies (Amanfu - Saucerman, 2011). According to the World Health Organization (WHO), cardiac disorders are the leading cause of death in the world. A considerable number of them are related to cardiac arrhythmias.

Arrhythmias are often associated with instabilities at the cellular level. A number of mechanisms in the cardiac cell can produce instabilities that give rise to *electrical alternans*, which consists of long-short alternations in action potentials despite a constant pacing rate. This process is known as a potential precursor of severe arrhythmias that can lead to ventricular fibrillation (Christini *et al.*, 2006; Echebarria - Karma, 2002; Krogh-Madsen *et al.*, 2010; Muñoz *et al.*, 2010; Rappel *et al.*, 2009). In cardiac tissue, electrical alternans might cause a chaotic process of propagation (Garzón *et al.*, 2011) and lead to spiral breakup (ten Tusscher - Panfilov, 2006; Gani - Ogawa, 2014) or other forms of ventricular fibrillation.

A number of studies (Fenton *et al.*, 2002; Karma, 1994; Qu *et al.*, 2000; Watanabe *et al.*, 2001) suggest that the occurrence of alternans is directly related to the instability of fixed points of the restitution relation, which is a map relating the action potential

duration (APD) with the preceding diastolic interval (Nolasco - Dahlen, 1968). Other mechanisms for alternans have been observed both numerically and experimentally, *e.g.*, in intracellular calcium cycling (Restrepo - Karma, 2009; Sato *et al.*, 2013). Despite its importance, many cardiac models are not capable of reproducing it and the adaptations necessary for giving rise to alternans are often not simple or not known.

Delay Differential Equations (DDEs) are known to produce complex dynamics in many applications of mathematical modeling (Wolfrum *et al.*, 2010), *e.g.* control theory (Shampine - Gahinet, 2006) and population dynamics (Ruiz-Herrera, 2012). They have also been applied to cardiac electrophysiology, either to describe the wave propagation in an excitable medium with a ring geometry (Courtemanche *et al.*, 1996) or to model the intracellular calcium dynamics (Thompson, 2013). Most electrophysiological processes in excitable cells involve delays since ion channels are composed of subunits that are activated interdependently, which causes latency between changes in voltage and channel gating. These delayed processes are often modeled by Markov-chain formulations (Rudy - Silva, 2006). An investigation on the use of DDEs to describe these processes is promising, specially in studies that are focused on arrhythmias and complex dynamics, since the genesis of the instabilities responsible for generating alternans is not completely established.

In the present study we explore the application of DDEs to ion channel formulations of different cardiac cell models, specifically in terms of the potential for promoting and modulating electrical alternans. A number of models of different physiological properties and levels of complexity were modified with DDEs in order to assess the possibility of inducing alternans and how the restitution instabilities are sensitive to delays. We also perform DDE-based experiments at the tissue level and assess how the use of delays affects wave propagation properties and spiral wave dynamics.

Tissue level simulations are computationally expensive, since they involve the numerical solution of highly nonlinear reaction-diffusion models. The computation of DDEs requires the storage of a history for the delayed variables. The size of the history for a given variable is proportional to the magnitude of the associated delay, so the use

of delays in a spatio-temporal simulation with a large number of nodes might demand a considerable amount of memory. In a ventricle simulation the use of a single delay variable could require a considerably high amount of additional memory. Therefore, another main goal of this project is the development of efficient techniques for performing simulations of this nature, especially when stability requirements limit the size of the simulation time step.

1.1 Objectives

There are many possible applications for the use of DDEs in cardiac modeling, considering the number of physiological elements that involve delayed processes within the cell. The first objective of this work is to explore possible applications of DDEs to the ion channel models based on the Hodgkin-Huxley formulation and assess their potential for producing proarrhythmic instabilities, such as electrical alternans at the cellular-level and spiral wave breakup at the tissue-level.

Secondly, this work aims to provide a numerical framework for the efficient simulation of DDE-based experiments in cardiac models, specially at the tissue level, where memory and computational performance requirements play a significant role. We also intend to provide sufficiently general adaptive algorithms that could possibly be applied to other fields of study involving DDEs.

1.2 Summary

A total of four articles were developed during this Ph.D. research, three of which were already published. The first two papers show that DDEs are able to restore/enhance alternans in models of cardiac cells based on the Hodgkin-Huxley formalism (Eastman *et al.*, 2016; Gomes *et al.*, 2017). Our third manuscript extends these results to tissue-level cardiac simulations (Gomes *et al.*, 2019a), showing that DDEs can reproduce the transition from tachycardia to fibrillation. The most recently submitted paper is focused on numerical methods for stiff models based on the Markov formalism for ion channels

(Gomes *et al.*, 2019b).

In Chapter 2 we present background information about the basics of cardiac electrophysiology, action potentials, models of ion channels and calcium handling, restitution analysis, cardiac alternans and mathematical modeling of wave propagation in cardiac tissue.

Chapter 3 presents the existing numerical methods that were applied during this project, alongside with the numerical techniques that we developed for efficient simulation of stiff models and DDE-based experiments. The chapter also describes the phenomenological modifications that we applied to different cardiac models in order to assess the dynamics produced by DDEs in ion channel formulations.

The results of this research are presented and discussed in chapter 4. The chapter starts with the results from single-cell experiments involving DDE-based modifications applied to a number of different cardiac models. The following section includes experiments performed at the tissue-level, aiming for computational performance and memory management efficiency. We also discuss how the wave propagation dynamics is affected by the use of delays.

The fifth chapter of this document contains a discussion about the obtained results and limitations of the present work. The sixth chapter presents the conclusions and final remarks.

2 Cardiac Electrophysiology

The heart is composed of two separate pumps: the right heart, which pumps blood through the lungs, and the left heart, which pumps the blood through the rest of the body (Hall - Guyton, 2006). Each pump is composed of two chambers: the atrium and the ventricle, as shown in Fig. 2.1.

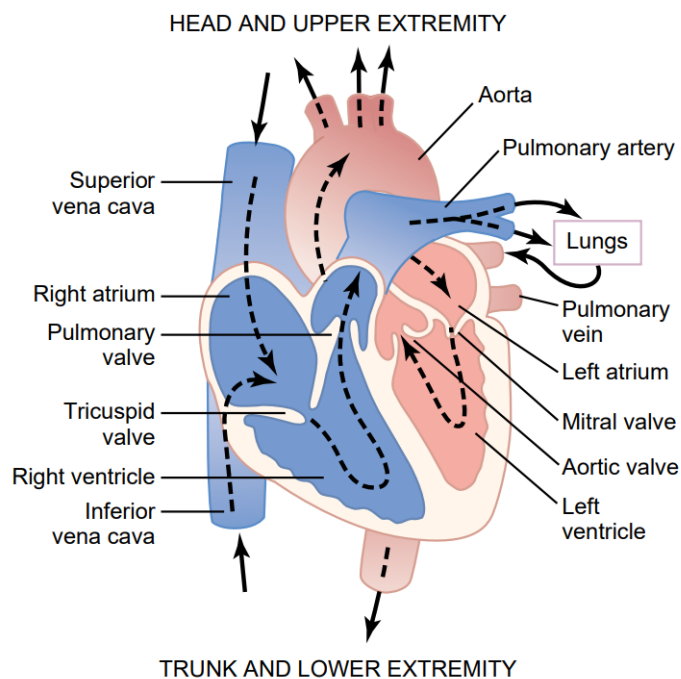


Figure 2.1: Basic structure of the heart: chambers and blood flow. Adapted from Hall - Guyton (2006).

The muscle fibers - or cardiac myocytes - within an atrium or ventricle must contract synchronously so the blood can be propelled properly. This synchronization is provided by the electrical signals that arise from the sinoatrial node and are conducted by specialized cells called *Purkinje fibers*. These electrical signals are propagated to the other cardiac myocytes, which undergo a process of electrical excitation that leads to mechanical contraction.

2.1 Electrophysiology of Cardiac Cells

A membrane potential is the difference of electrical potential between the intracellular and the extracellular media of a cell. Virtually all cells of the body exhibit a membrane potential of a few millivolts (Hall - Guyton, 2006), but some cells - known as *excitable cells* - are able produce dynamic changes in the membrane potential in response to external electrical signaling.

2.1.1 The action potential (AP)

Cardiac muscle cells are considered excitable because of their ability to produce action potentials in response to electrical stimuli. The action potential (AP) is a trajectory undergone by the membrane electrical potential, which consists of a rapid depolarization of the cell membrane (rise of the membrane potential) followed by a process of repolarization (membrane potential decreases to the resting value). The depolarization is caused by a rapid influx of sodium to the intracellular media, while the repolarization is mainly promoted by potassium efflux. The ion fluxes through the membrane are controlled by protein structures called *ion channels*, as shown in Fig. 2.2.

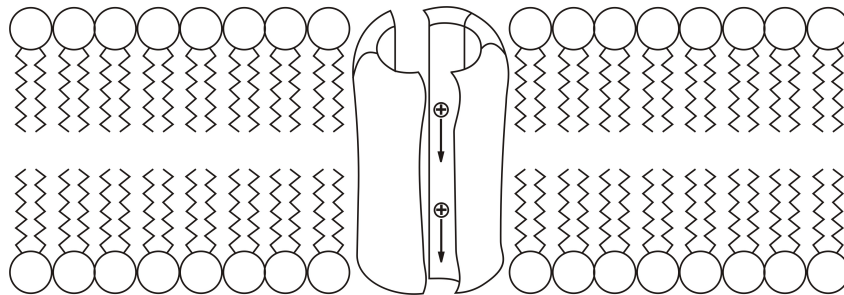


Figure 2.2: Basic structure of a cell membrane and a voltage-gated ion channel. Adapted from Campos (2008).

Figure 2.3 shows the main phases of a typical cardiac action potential. The repolarization is divided into phases 1, 2 and 3. The phase 2 - or *plateau* - is mainly sustained by calcium influx, and it is the phase that most contributes to the action potential duration (APD). Phase 3 is mainly characterized by outward potassium currents that lead the membrane potential back to its resting value. It is also worth noting that different types of potassium and calcium channels operate distinctively during the action

potential. That happens because each type of ion channel has a gating structure that responds differently to changes in voltage or ion concentration.

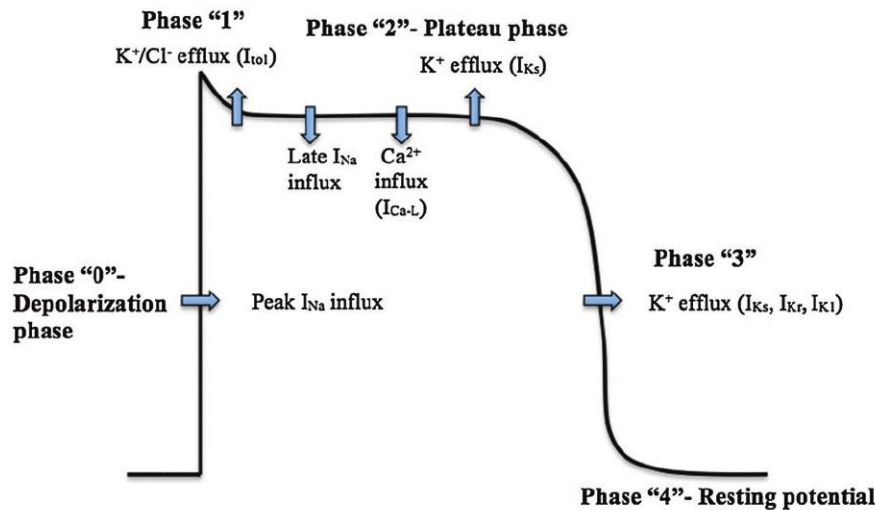


Figure 2.3: Phases of the action potential from a typical nonpacemaker heart cell (Saad *et al.*, 2015).

2.1.1.1 Threshold potential

The action potential of an excitable cell is initiated when the membrane is depolarized beyond a threshold, which usually corresponds to a membrane potential of a few tens of millivolts above the resting value, which varies with species and cell type. As an example, a typical human ventricular epicardial cell has a resting potential of about -87 mV and a threshold potential of -55 mV approximately (ten Tusscher *et al.*, 2004). If a stimulus current is not strong enough to drive the potential beyond the threshold, the membrane will rapidly repolarize to its resting state after the stimulus ceases. Otherwise, the sodium channels will be activated, and a massive influx of sodium will depolarize the membrane, initiating an action potential.

2.1.1.2 Refractory period

The cardiac refractory period is an interval of time after the initiation of an action potential in which it is impossible to initiate a subsequent action potential. Figure 2.4 illustrates this property of an excitable cell, where stimuli that would normally drive the

membrane potential above the threshold and initiate an action potential fail to produce a second AP during the refractory period. This period is slightly shorter than the action potential duration under normal conditions and it is essential to ensure the proper contraction of the heart through synchronous wave propagation across the cardiac fibers.

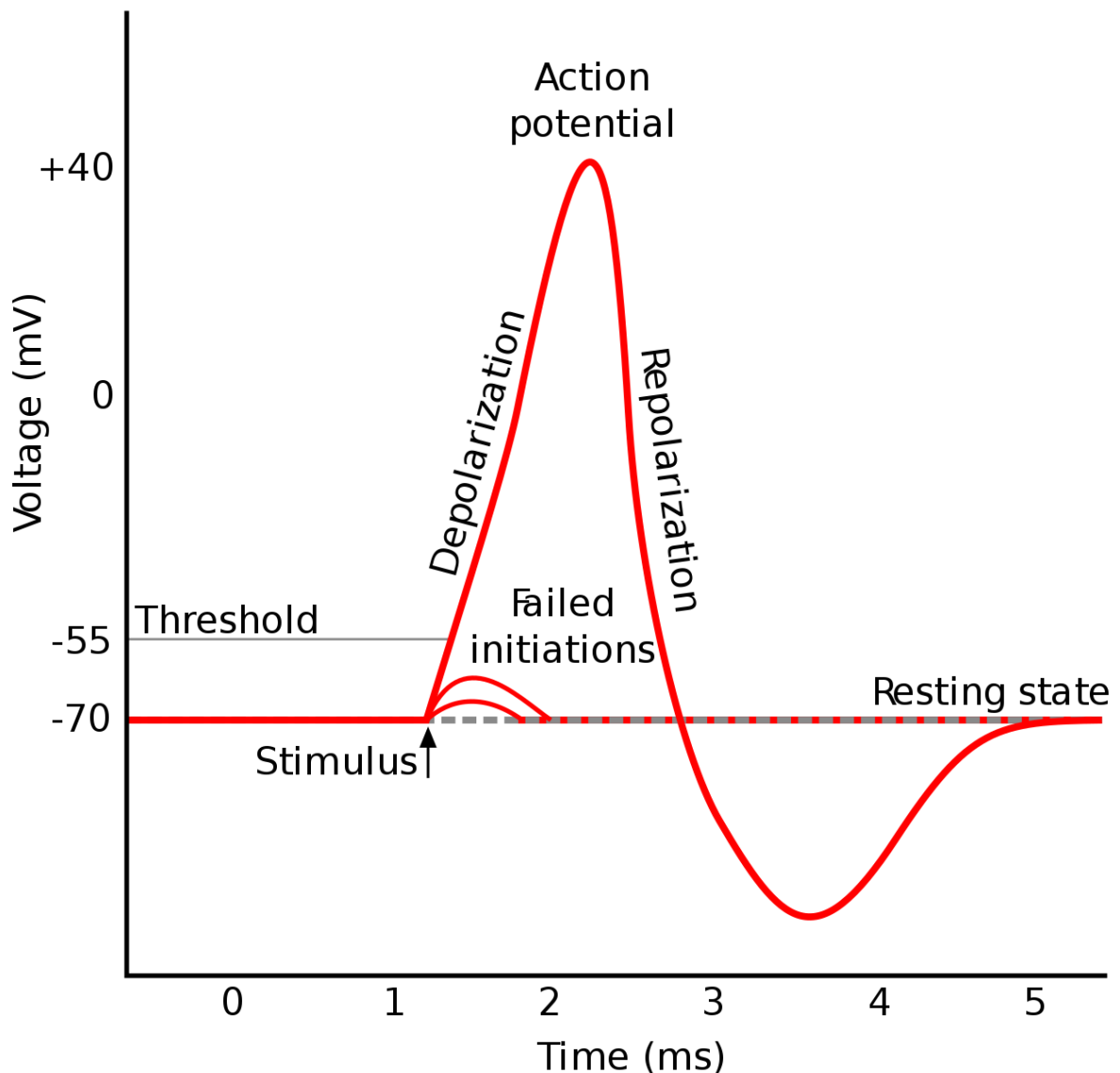


Figure 2.4: Plot of a membrane potential recording where stimulus currents fail to initiate a second action potential during the refractory period, which is highlighted by a gray dashed line (adapted from Commons (2007)).

Despite the refractory period being responsible for maintaining the proper functioning of the heart, it also plays an important role in the genesis of reentrant waves in cardiac tissue. Reentry is a phenomenon where an electrical wave continuously circulates a

specific region of cardiac tissue, generally associated with tachycardia and other types of arrhythmia (Hall - Guyton, 2006). Figure 2.5 illustrates the mechanism of reentry in a media with a fast conduction path on the left, an obstacle in the middle, and a slow conduction path on the right. The preexisting refractory period in the cells located at the right path blocks the signal coming from the top but allows a reentrant wave from the left path to travel in the retrograde direction and promote a continuous circulating wave of electrical excitation.

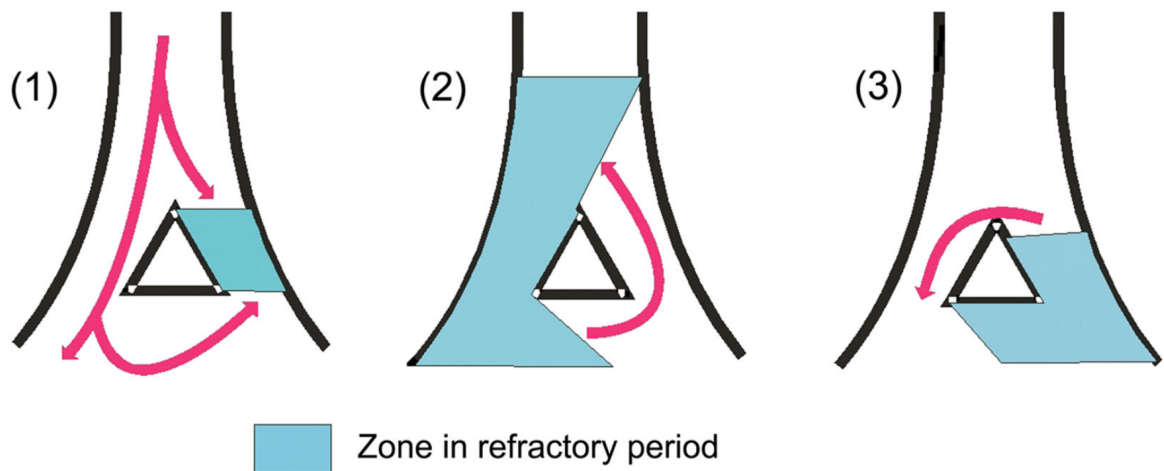


Figure 2.5: Schematic of the mechanism of reentry in a heterogeneous media with an obstacle (adapted from Timour *et al.* (2012)).

2.1.2 Modeling the membrane

The first model describing the action potential of an excitable cell was proposed by Hodgkin - Huxley (1952). Their model is capable of reproducing the action potential of the squid giant axon with a system of four ODEs. A decade of after its publication, Noble (1962) adapted the Hodgkin-Huxley model to develop the first model for the action potential of cardiac Purkinje cells. Nearly all modern cardiac cell models are somehow derived from the Hodgkin-Huxley neural model.

The Hodgkin-Huxley model describes the membrane as the circuit shown in Fig. 2.6, where V is the membrane potential, C_m is the membrane capacitance, I_{Na} is the sodium current, I_K is the potassium current and I_L is a leak current (composed by other ion

species that are not considered in the model). Each ion current computes all ion charges crossing through the corresponding population of ion channels in the membrane.

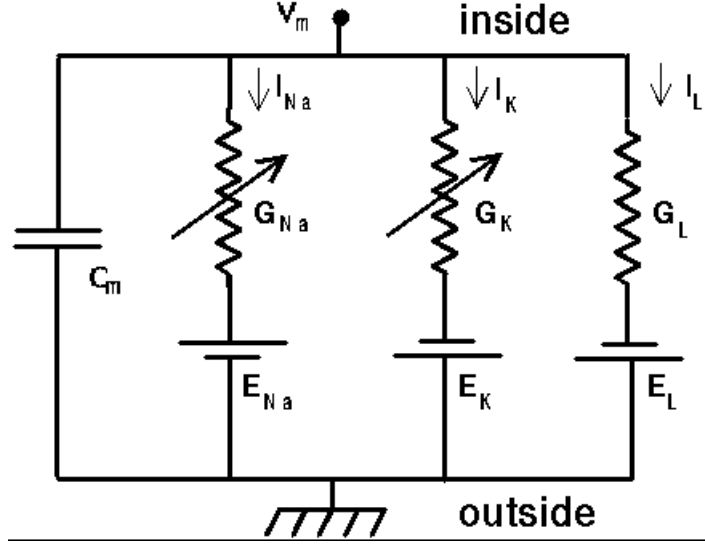


Figure 2.6: Representation of the neuron membrane as an electrical circuit.

The equation governing the membrane potential is obtained by the Kirchhoff's voltage law and it is given by

$$\frac{dV}{dt} = -\frac{1}{C_m} I_{ion}, \quad (2.1)$$

where I_{ion} is the sum of all ion currents, which are given by

$$I_{Na} = g_{Na}(V - E_{Na}), \quad (2.2)$$

$$I_K = g_K(V - E_K), \quad (2.3)$$

$$I_L = g_L(V - E_L). \quad (2.4)$$

The Nernst Potentials E_{Na} , E_K and E_L are functions of their associated ions' concentrations, but are considered as constants in this model. The conductances g_{Na} and g_K are determined by the voltage-gated dynamics of the sodium and potassium channels, respectively.

2.1.3 Ion channel models

Each sodium channel in the Hodgkin-Huxley model is considered to have three gates associated with its activation and one gate for its inactivation. Let m and h be the gating variables for the activation and inactivation gates, respectively. The sodium conductance is given by

$$g_{Na} = \bar{g}_{Na} m^3 h, \quad (2.5)$$

$$\frac{dm}{dt} = \frac{m_{\infty}(V) - m}{\tau_m(V)}, \quad (2.6)$$

$$\frac{dh}{dt} = \frac{h_{\infty}(V) - h}{\tau_h(V)}, \quad (2.7)$$

where \bar{g}_{Na} is the maximum sodium conductance (the conductance value when all sodium gates are fully open). The Equations (2.6) and (2.7) are called the *Hodgkin-Huxley formulations* for the gating variables m and h , respectively, where $m_{\infty}(V)$, $h_{\infty}(V)$, $\tau_m(V)$ and $\tau_h(V)$ are nonlinear functions of the membrane potential V , formulated to fit the voltage-clamp experimental data Hodgkin - Huxley (1952).

The potassium channels are assumed to have four identical activation gates, represented by the gating variable n . The conductance for the potassium current is given by

$$g_K = \bar{g}_K n^4, \quad (2.8)$$

$$\frac{dn}{dt} = \frac{n_{\infty}(V) - n}{\tau_n(V)}. \quad (2.9)$$

Many models for cardiac myocytes have been developed following the Hodgkin-Huxley formulation for ion kinetics. As an example, the model by ten Tusscher - Panfilov (2006) describes the electrical activity of the human ventricular cell and includes 12 gating variables for modeling 5 different types of ion channels.

2.1.3.1 Markov-based Models

Advances in genetics, molecular biology and electrophysiology experiments have provided new data and information related to the structure and function of ion channels (Wilde - Bezzina, 2005; Seo *et al.*, 2006) that cannot be represented using the Hodgkin-Huxley description. The continuous-time Markov Chain (MC) formalism has been increasingly used to describe both function and structure of ion channels, enabling the description of highly detailed physiological processes. MC-based models have enabled simulations of structural abnormalities due to genetic diseases and drug-binding effects on ion channels (Clancy - Rudy, 1999; Brennan *et al.*, 2009; Clancy *et al.*, January 2007).

The Hodgkin-Huxley formulation is based on the assumption of independent gating so it is not able, e.g., to describe the inactivation dependency on the activation of Na^+ channels, which was experimentally verified (Armstrong - Bezanilla, 1977b,a). As an example, consider a three-state Markov model for a hypothetical ion channel as represented in Figure 2.7. The model supposes an ion channel can be either open (O), closed (C) or inactive (I), and inactivation can only occur from the open state. In this case, a Hodgkin-Huxley formulation would not be applicable and the states must be described individually by the following equations:

$$\frac{dC}{dt} = -\alpha C - \beta O, \quad (2.10)$$

$$\frac{dO}{dt} = \alpha C - (\beta + \gamma)O + \delta I, \quad (2.11)$$

$$\frac{dI}{dt} = \gamma O - \delta I, \quad (2.12)$$

where C , O and I represent the proportion of channels in each corresponding state. Note that this system is overdetermined in that the algebraic equation $C + O + I = 1$ also must be satisfied.

Markov models for electrophysiology can vary in complexity from simple three-state models to complex chains containing up to 18 states, like the one for the L-type Ca^{2+} channel in the model by Bondarenko (2014). Figure 2.8 shows the 9-state Markov scheme for the Na^+ channel from the model by Bondarenko *et al.* (2004).

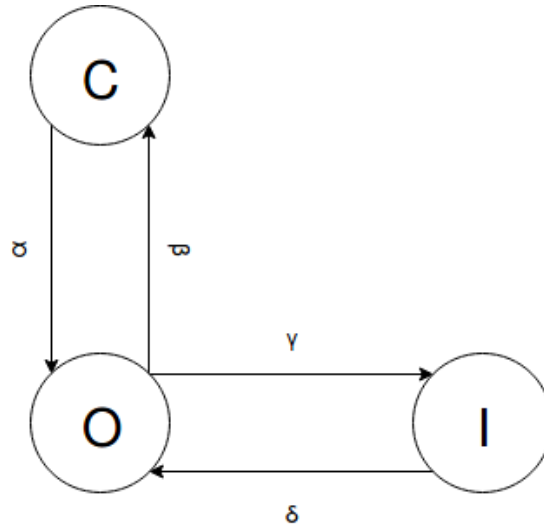


Figure 2.7: Three-state Markov model for a hypothetical ion channel.

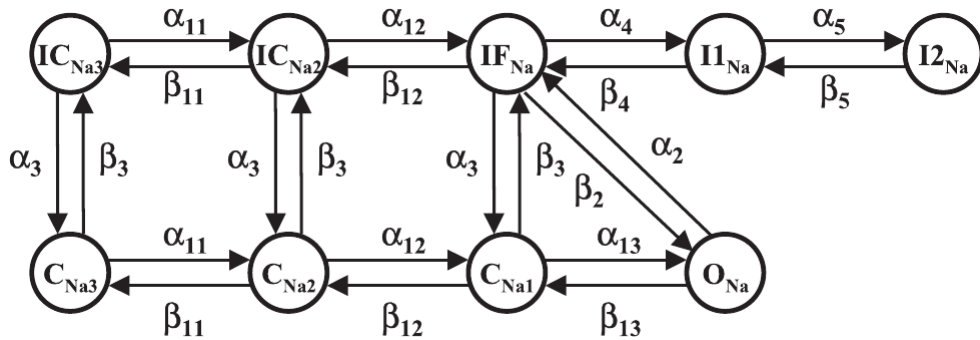


Figure 2.8: Markov model for the Na^+ channel described in the model for the mouse ventricular action potential proposed by Bondarenko *et al.* (2004).

2.1.4 Calcium handling

Intracellular processes mediated by calcium are directly responsible for proper myocyte contraction. The process of depolarization (excitation) triggers a considerable influx of calcium ions through the L-type channels into the intracellular medium. This inward calcium current not only prolongs the action potential duration, but also promotes a slight increase in the intracellular concentration of Ca^{2+} , which activates ryanodine receptors (RyR) that trigger a much larger release of Ca^{2+} from the sarcoplasmic reticulum (SR) (Hall - Guyton, 2006). The resulting transient increase in intracellular calcium concentration initiates the sarcomere contraction when cytosolic calcium binds to myofilaments called troponin, actin and myosin. As the cell membrane is repolarized, calcium ions are stored back into the SR by the SERCA pump and

intracellular/extracellular balance of Ca^{2+} is restored by the $Na^+ - Ca^{2+}$ exchanger located in the cell membrane.

Detailed modeling of calcium cycling had not been included in cardiac models until recently. As an example, the model proposed by ten Tusscher - Panfilov (2006) computes Ca^{2+} dynamics considering two different compartments in the SR: the JSR (junctional sarcoplasmic reticulum) and the NSR (network sarcoplasmic reticulum). They also consider a separated compartment for the region of the cytoplasm that is vicinal to the L-type calcium channels and the RyR receptors. Ions of calcium transit between adjacent compartments via simple diffusion. A schematic diagram of the model is shown in Figure 2.9.

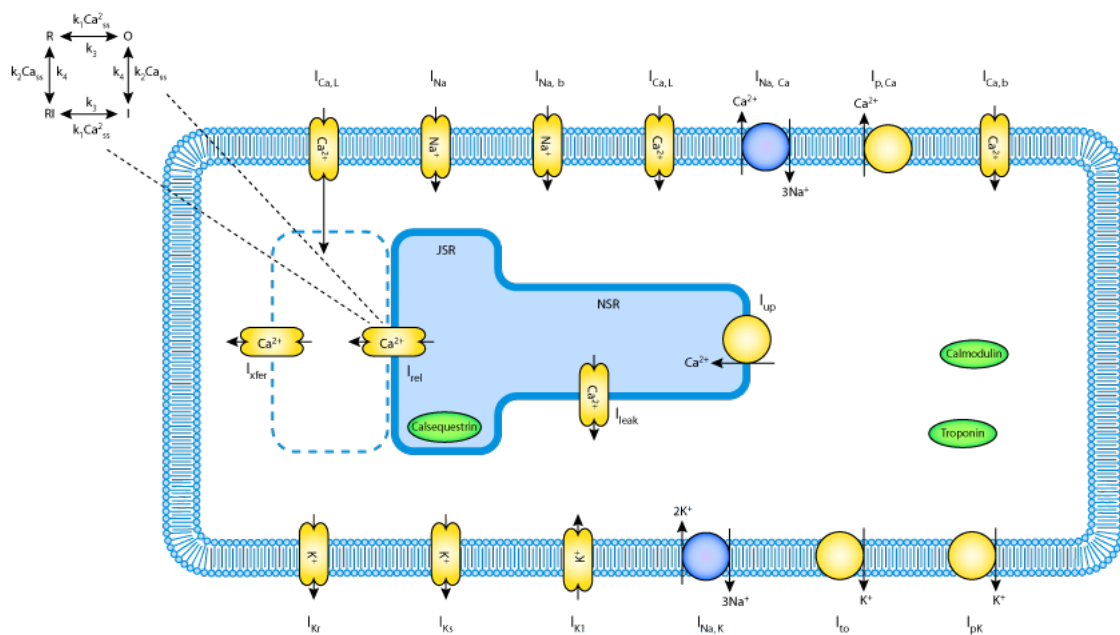


Figure 2.9: Schematic diagram of the ion fluxes described by the ten Tusscher - Panfilov (2006) mathematical model of the human ventricular myocyte.

2.2 Electrical alternans

Cardiac electrical alternans is a dynamical state where the action potential alternate between two periods despite a constant - and typically fast - pacing rate. The study of alternans is particularly important because it is frequently associated with dangerous

conditions such as myocardial ischemia (Kléber *et al.*, 1978; Kwofie *et al.*, 2011) and cardiac arrhythmia (Weiss *et al.*, 2011; Bayer *et al.*, 2016). This phenomenon is illustrated in Figure 2.10, where action potentials start to alternate between long and short in a cardiac fiber when the pacing period is reduced from 270 ms to 250 ms.

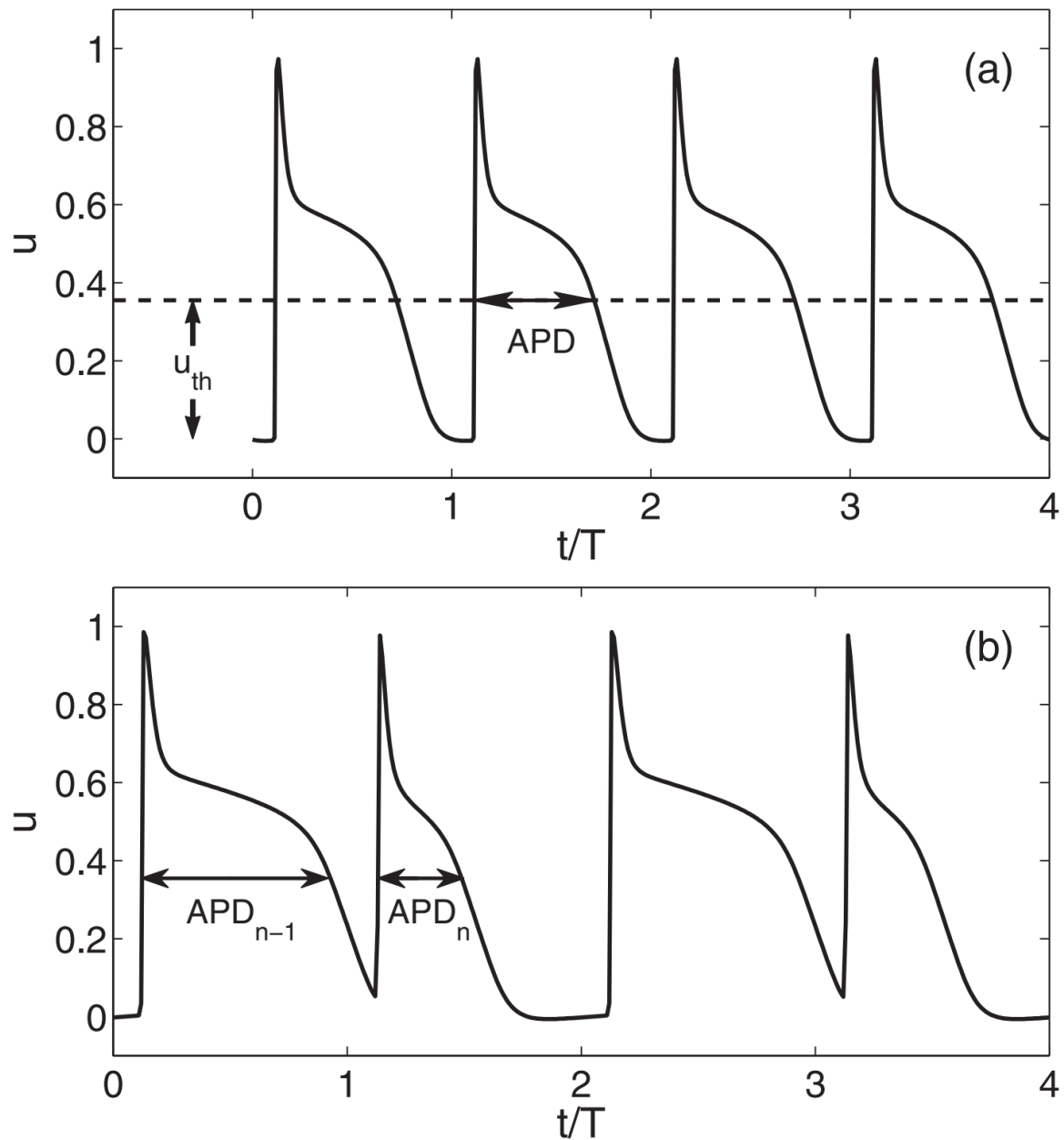


Figure 2.10: Occurrence of alternans at a fast pacing rate in a cardiac fiber (adapted from Garzón *et al.* (2011)): (a) action potentials with constant duration for a pacing period of 270 ms; (b) action potentials with period-doubling for a constant pacing period of 250 ms.

2.3 Restitution analysis

Restitution analysis - also known as APD restitution analysis - consists of determining a map that relates the action potential duration (APD) with the preceding diastolic (DI) interval by obtaining steady-state solutions using different pacing periods - cycle lengths (CL) or basic cycle lengths (BCL) - as originally described by Nolasco - Dahlen (1968). The APD is the time an action potential takes to repolarize the membrane after depolarization. The DI is the time elapsed from the end of an action potential to the beginning of the next one, *i.e.*, $DI = CL - APD$, as shown in 2.11.

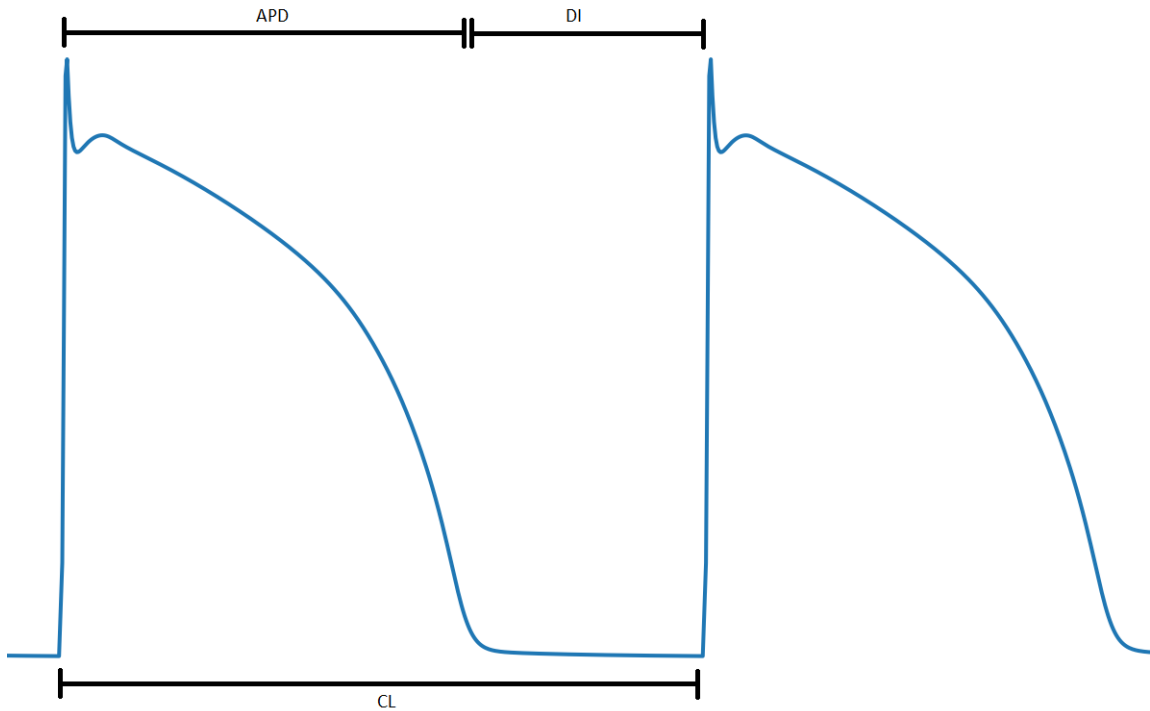


Figure 2.11: Measurements for performing a restitution analysis: action potential duration (APD), diastolic interval (DI) and cycle length (CL).

Restitution curves with APD as a function of DI can be utilized to analyze the conditions for occurring alternans. A number of studies indicate that a restitution curve with slope greater than 1 is somehow associated with the occurrence of instabilities and voltage-driven alternans (Guevara *et al.*, 1984; Garfinkel *et al.*, 2000a). Moreover, a non-monotonic restitution curve can indicate the occurrence of chaos at the tissue level (Qu *et al.*, 1997). Figure 2.12 shows an example where the steep region of a restitution curve (*i.e.* slope greater than 1) is associated with the occurrence of period-doubling (alternans)

in the model proposed by Fox *et al.* (2002).

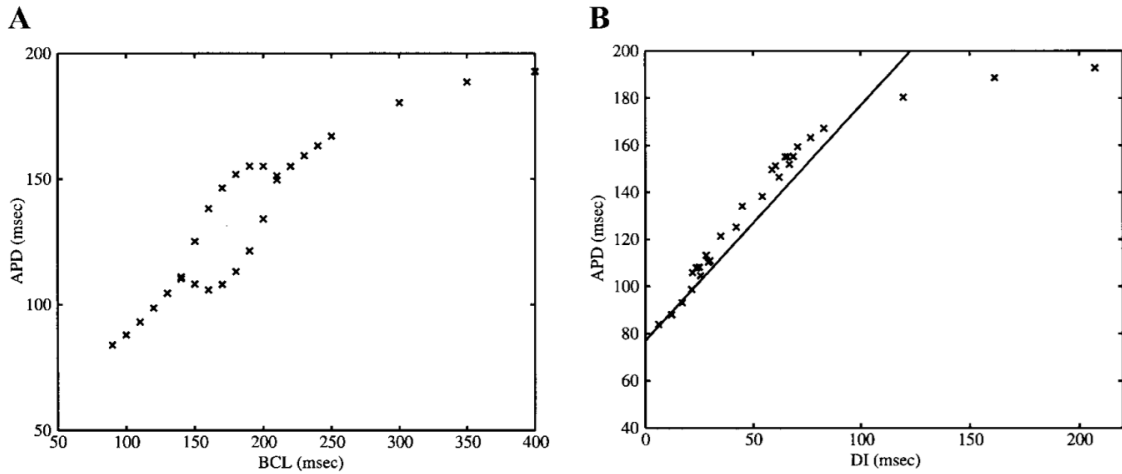


Figure 2.12: Relation between a steep restitution curve and period-doubling (adapted from Fox *et al.* (2002)): (A) bifurcation diagram, where APD is plotted as a function of the basic cycle length (BCL); (B) restitution plot of APD as a function of the diastolic interval (DI) alongside with a solid line with a slope of 1.

APD alternans can also arise from non voltage-driven mechanisms, such as calcium cycling instabilities (Díaz *et al.*, 2004). Therefore, restitution analysis is not always a reliable tool for assessing the manifestation of alternans, since it can occur even when the restitution slope is not greater than 1 (Goldhaber *et al.*, 2005).

2.4 Tissue Models

The bidomain model (Tung, 1972) is the main framework for simulating the electrical activity of cardiac tissue. The model describes electrical potential propagation in both intracellular and extracellular media. It is deduced from the volume conductor theory for quasi-static electric and magnetic fields, and divides the tissue into two continuum domains (intracellular and extracellular). For each point of the tissue an electrical potential is associated in each of the two domains, and it is defined as a quantity averaged over a small volume.

If u_e is the extracellular potential, u_i is the intracellular potential, \mathbf{M}_e and \mathbf{M}_i are the conductivities tensors in the two domains, and $V = u_i - u_e$ is the transmembrane

potential, then the bidomain model can be written as:

$$\nabla \cdot (\mathbf{M}_i \nabla V) + \nabla \cdot (\mathbf{M}_i \nabla u_e) = \chi C_m \frac{\partial V}{\partial t} + \chi I_{ion}(V(\mathbf{x}, t), \mathbf{y}, t), \quad (2.13)$$

$$\nabla \cdot (\mathbf{M}_i \nabla V) + \nabla \cdot ((\mathbf{M}_i + \mathbf{M}_e) \nabla u_e) = 0, \quad (2.14)$$

$$\frac{\partial \mathbf{y}}{\partial t} = \mathbf{f}(V(\mathbf{x}, t), \mathbf{y}, t), \quad (2.15)$$

where χ is the ratio of membrane area to volume, C_m is the transmembrane capacitance by unit of membrane area and I_{ion} is the ion current crossing the membrane, which is determined by the state variables \mathbf{y} from a myocyte model. Assuming the heart is surrounded by an insulating medium, the boundary conditions are

$$\mathbf{n} \cdot (\mathbf{M}_i \nabla V + \mathbf{M}_i \nabla u_e) = 0, \quad (2.16)$$

$$\mathbf{n} \cdot (\mathbf{M}_e \nabla u_e) = 0. \quad (2.17)$$

The bidomain model is a nonlinear system of partial differential equations. One can reduce the model to a single partial differential equation by assuming that both domains have equal anisotropy rates. So if $\mathbf{M}_e = \lambda \mathbf{M}_i$, it is possible to deduce the *monodomain model*, which is given by

$$\frac{\lambda}{1 + \lambda} \nabla \cdot \mathbf{M}_i \nabla V = \chi C_m \frac{\partial V}{\partial t} + \chi I_{ion}(V(\mathbf{x}, t), \mathbf{y}, t), \quad (2.18)$$

$$\frac{\partial \mathbf{y}}{\partial t} = \mathbf{f}(V(\mathbf{x}, t), \mathbf{y}, t), \quad (2.19)$$

$$\mathbf{n} \cdot (\mathbf{M}_i \nabla V) = 0, \quad (2.20)$$

$$V(\mathbf{x}, 0) = V_0(\mathbf{x}), \quad (2.21)$$

$$\mathbf{y}(\mathbf{x}, 0) = \mathbf{y}_0(\mathbf{x}). \quad (2.22)$$

For an isotropic medium, the model can be simplified into the following formulation:

$$\frac{\partial V}{\partial t} = D\Delta V - \frac{1}{C_m}I_{ion}(V(\mathbf{x}, t), \mathbf{y}, t), \quad (2.23)$$

$$\mathbf{n} \cdot \nabla V = 0, \quad (2.24)$$

$$\frac{\partial \mathbf{y}}{\partial t} = \mathbf{f}(V(\mathbf{x}, t), \mathbf{y}, t), \quad (2.25)$$

where D is the constant diffusion coefficient given by $D = \frac{\lambda}{1+\lambda} \frac{\sigma}{\chi C_m}$, where σ is the medium's conductivity.

The monodomain model is not as realistic or physiologically accurate as the bidomain model, especially in situations where the extracellular potential is essential, e.g., applications involving data collected from electrocardiograms. On the other hand, the monodomain model has reduced computational complexity and is still adequate for studying wave propagation dynamics and even complex types of arrhythmia (Potse *et al.*, 2006), such as fibrillation.

Cardiac fibrillation is a dangerous form of arrhythmia that is thought to be caused by breakups of initial reentrant waves in cardiac tissue (Weiss *et al.*, 2002). The underlying mechanism of spiral breakups is often associated with steep restitution of action potential duration and electrical alternans (Qu *et al.*, 2000; Garfinkel *et al.*, 2000b). Figure 2.13 shows snapshots from a monodomain simulation where alternans induce spiral wave breakup in the two-variable model proposed by Karma (1994). This two-dimensional experiment illustrates the transition from an arrhythmic state of tachycardia to cardiac fibrillation.

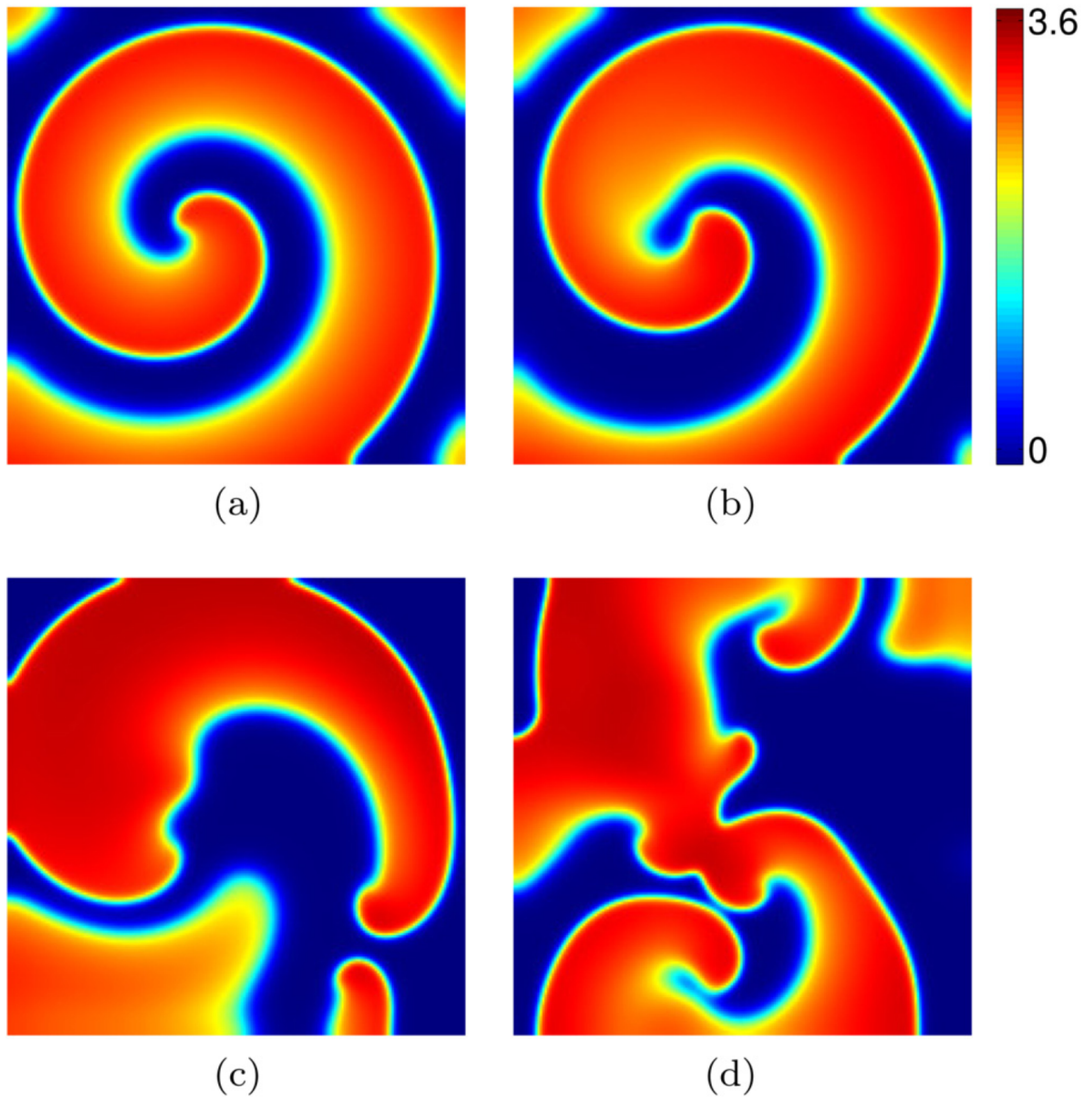


Figure 2.13: Voltage snapshots of a 2D simulation of the Karma (1994) model. A single spiral wave (a) is destabilized by electrical alternans (b) and breaks up into multiple spiral segments (c) that evolve into spiral turbulence (d). Image adapted from Byrne *et al.* (2015)

3 Methods

This chapter addresses the numerical schemes applied in this research with the objective of performing computationally efficient DDE-based tissue simulations. It also describes the techniques we applied to modify action potential models with DDE-based formulations.

3.1 Methods for ODE-based models

The following subsections describe methods that are classically utilized for the numerical solution of models based on the Hodgkin-Huxley formulation.

$$\frac{d\mathbf{y}}{dt} = \mathbf{f}(\mathbf{y}, t), \quad (3.1)$$

$$\mathbf{y}(t_0) = \mathbf{y}_0. \quad (3.2)$$

3.1.1 Forward Euler method (FE)

The traditional forward Euler method is the simplest among the classical explicit schemes. It has first-order accuracy and its stability is conditioned to the size of the time step Δt . Given an initial condition $\mathbf{y}_0 = \mathbf{y}(t_0)$, the approximated solution at each step $n + 1$ is computed by:

$$\mathbf{y}_{n+1} = \mathbf{y}_n + \Delta t \mathbf{f}(\mathbf{y}_n, t_n), \quad (3.3)$$

where \mathbf{y}_{n+1} is the discretization of the ODE at step $n + 1$, \mathbf{y}_n is its value at the previous step n , t_n is given by $t_0 + n\Delta t$, and $\mathbf{f}(\mathbf{y}_n, t_n)$ is the right-hand-side function.

The system of ODEs may be very stiff in realistic models of excitable systems (SUNDNES *et al.*, 2002). In this case, the Euler method may need a large number of very small time steps to finish a simulation without losing numerical stability.

3.1.2 Rush-Larsen method (RL)

The method proposed by Rush - Larsen (1978) aims to improve the stability of the traditional Euler scheme when applied to models based on the Hodgkin-Huxley formulation for ion channels. The model is partitioned between gating variables - which are also called *quasi-linear* variables - and fully nonlinear variables. The last group of variables is integrated with the traditional FE scheme, while the equations associated with the first group are considered locally linear at each time step and are solved by an exponential integrator. For a gating variable p^j associated with the ODE

$$\frac{dp^j}{dt} = \frac{p_\infty^j - p^j}{\tau_{p^j}}, \quad (3.4)$$

which can be written as

$$\frac{dp^j}{dt} = a^j p^j + b^j, \quad (3.5)$$

with a^j and b^j being nonlinear functions of the membrane potential or a certain intracellular concentration, the following formulation is applied at each step $n + 1$:

$$p_{n+1}^j = \begin{cases} e^{a_n^j \Delta t_n} \left(p_n^j + \frac{b_n^j}{a_n^j} \right) - \frac{b_n^j}{a_n^j}, & \text{if } |a_n^j| \geq \delta \\ p_n^j + \Delta t_n (a_n^j p_n^j + b_n^j), & \text{otherwise,} \end{cases} \quad (3.6)$$

where a_n^j and b_n^j are previously computed approximations for $a^j(t_n)$ and $b^j(t_n)$, respectively.

3.2 DDE-based formulations for ion channels

The traditional modeling techniques for describing an action potential are either based on the Hodgkin-Huxley formalism or Markov models for ion channels. Markov models are particularly useful to describe delayed activation or inactivation of ion channels through the use of intermediate discrete states of channel conformation. It has been recently shown that it is possible to approximate action potential models with a single delay

differential equation (Rameh *et al.*, 2019), which makes DDEs a candidate alternative tool for describing ion channel dynamics in modern models of electrophysiology.

In this research, we focus on introducing DDEs into preexisting action potential models in order to aggregate new dynamical features while preserving physiological properties. We propose a DDE-based technique to perturb Hodgkin-Huxley formulations with delays. The technique consists of imposing delays on the voltage (or calcium) sensing of ion channels. Given a gating variable n with time constant $\tau_n(V)$ and steady-state value $n_\infty(V)$, the following method applies a delay δ to the membrane potential V , converting the ODE

$$\frac{dn}{dt} = \frac{n_\infty(V(t)) - n}{\tau_n(V(t))}, \quad (3.7)$$

into the DDE:

$$\frac{dn}{dt} = \frac{n_\infty(V(t - \delta)) - n}{\tau_n(V(t - \delta))}. \quad (3.8)$$

Some gating variables are assumed to have a very small time constant, so they are mathematically described as algebraic functions of V . As an example, the inward rectifier potassium current (I_{K_1}) in the Luo - Rudy (1991) model is modeled by:

$$I_{K_1} = \bar{g}_{K_1} K_{1\infty}(V(t))(V - E_K), \quad (3.9)$$

where \bar{g}_{K_1} is the maximum conductivity of I_{K_1} channels and $K_{1\infty}$ is the associated activation gate, which is described as a nonlinear function of V . A delay δ can be applied to this gating variable if $V(t)$ is replaced by $V(t - \delta)$ when evaluating $K_{1\infty}(V(t))$:

$$I_{K_1} = \bar{g}_{K_1} K_{1\infty}(V(t - \delta))(V - E_K). \quad (3.10)$$

In this case, the ODE associated with V is directly converted into a DDE, since I_{K_1} contributes to the total ion current I_{ion} in

$$\frac{dV}{dt} = -\frac{1}{C_m} I_{ion}. \quad (3.11)$$

3.3 Methods for DDE-based single cell models

3.3.1 Forward Euler adaptation for a DDE

Let us consider the initial value problem (IVP) given by

$$\frac{dy}{dt} = f(t, y(t), y(t - \delta)), t > 0, \quad (3.12)$$

$$y(t) = g(t), t \leq 0, \quad (3.13)$$

where δ is a fixed positive value and g is a function that provides a initial history for y . Equation (3.12) is a delay differential equation with a single constant delay δ . The MATLAB package *dde23* (Shampine - Thompson, 2001) implements an adaptive time step method based on an m -stage Runge-Kutta (RK) formulation. A fixed time step version of the method, when applied to the IVP (3.12) with $\Delta t < \delta$, is given by

$$y_{n+1} = y_n + \Delta t \sum_{i=1}^m c_i f_{ni}, \quad (3.14)$$

where

$$f_{ni} = \begin{cases} f(t_{ni}, y_{ni}, g(t_{ni} - \delta)), & \text{if } t_{ni} \leq \delta \\ f(t_{ni}, y_{ni}, \tilde{y}(t_{ni} - \delta)), & \text{otherwise,} \end{cases} \quad (3.15)$$

$$y_{ni} = y_n + \Delta t \sum_{j=1}^{i-1} d_{ij} f_{nj}, \quad (3.16)$$

$$t_{ni} = t_n + e_i \Delta t, \quad (3.17)$$

where y_n is the previously computed approximation for $y(t_n)$, c_i and d_i are predefined weights of the chosen Runge-Kutta scheme, t_{ni} are the corresponding predefined intermediate times with $0 \leq e_i \leq 1$, and \tilde{y} is a history function obtained from previously computed values of y .

In order to compute $\tilde{y}(t_{ni} - \delta)$, we must consider generalizing the formulation given

by Eq.(3.14) to a point $t_{p+\sigma}$ in $[t_p, t_{p+1}]$, taking the coefficients c_i as polynomials in σ :

$$y_{p+\sigma} = y_p + \Delta t \sum_{i=1}^m c_i(\sigma) f_{pi}. \quad (3.18)$$

Then, with the previously computed values y_1, y_2, \dots, y_{n-1} and $f_{1i}, f_{2i}, \dots, f_{(n-1)i}$ available in memory, we can obtain an approximation to any $y(\tau)$ for $t_p \leq \tau \leq t_{p+1}$ and p in $\{0, 1, \dots, n-1\}$ with the use of Equation (3.18).

We could derive a first-order version of this scheme, which would be an adaptation of the forward Euler method to DDEs:

$$y_{n+1} = \begin{cases} y_n + \Delta t f(t_n, y_n, g(t_n - \delta)), & \text{if } t_n \leq \delta \\ y_n + \Delta t f(t_n, y_n, \tilde{y}(t_n - \delta)), & \text{otherwise,} \end{cases} \quad (3.19)$$

where $\tilde{y}(t_n - \delta)$ can be written as $y_{p+\sigma}$ if $t_n - \delta = t_p + \sigma \Delta t$. If f_p is the right-hand side evaluated at the p -th step, then

$$\tilde{y}(t_n - \delta) = y_{p+\sigma} = y_p + \Delta t \sigma f_p, \quad (3.20)$$

which is equivalent to

$$\tilde{y}(t_n - \delta) = y_{p+\sigma} = (1 - \sigma)y_p + \sigma y_{p+1}. \quad (3.21)$$

Therefore, it is not needed to store the right-hand side values in this case, since each past value of y can be obtained by direct linear interpolation of pre-evaluated values of y .

3.3.2 *Rush-Larsen method for DDE-based cardiac models*

The forward Euler adaptation for DDEs can be easily extended to systems composed of ODEs and DDEs, such as the cardiac models we modified in this research using the formulation described in Section 3.2. Also, the Rush-Larsen integrator can be naturally applied to the Hodgkin-Huxley equations.

Let us consider an action potential model with the DDE formulation (3.8) applied to

n_p voltage-dependent gating variables $\mathbf{p} = [p^1, p^2, \dots, p^i, \dots, p^{n_p}]^\top$ and to n_q intracellular calcium-dependent gating variables $\mathbf{q} = [q^1, q^2, \dots, q^j, \dots, q^{n_q}]^\top$ described by

$$\frac{dV}{dt} = -\frac{1}{C_m} I_{ion}, \quad (3.22)$$

$$\frac{dCa_i}{dt} = f^{Ca_i}(V, \mathbf{p}, \mathbf{q}, \mathbf{y}, t), \quad (3.23)$$

$$\frac{dp^i}{dt} = a_p^i(V(t - \delta_{p^i}))p^i + b_p^i(V(t - \delta_{p^i})), i \in \{1, 2, \dots, n_p\}, \quad (3.24)$$

$$\frac{dq^j}{dt} = a_q^j(Ca_i(t - \delta_{q^j}))q^j + b_q^j(Ca_i(t - \delta_{q^j})), j \in \{1, 2, \dots, n_q\}, \quad (3.25)$$

$$\frac{dy^k}{dt} = f^k(V, \mathbf{p}, \mathbf{q}, \mathbf{y}, t), k \in \{1, 2, \dots, n_{nl}\}, \quad (3.26)$$

where δ_{p^i} and δ_{q^j} are fixed delay sizes associated with the gates p^i and q^j , respectively; V is the membrane potential, C_m is the membrane capacitance, and I_{ion} is the total transmembranic current; Ca_i is the intracellular calcium concentration and f^{Ca_i} is its associated right-hand-side function; y^k represents any remaining nonlinear variable of the model with f^k being its associated right-hand-side function.

The non-gating variables of the model are all described by the ODEs (3.22), (3.23), and (3.26), and can be solved via direct application of the forward Euler method. The DDEs (3.24) and (3.25) can be solved by an adapted version of the Rush-Larsen integrator proposed in this work, which is given by

$$a_{p,n}^i = a_p^i(\tilde{V}(t_n - \delta_{p^i})), \quad (3.27)$$

$$b_{p,n}^i = b_p^i(\tilde{V}(t_n - \delta_{p^i})), \quad (3.28)$$

$$p_{n+1}^i = \begin{cases} e^{a_{p,n}^i \Delta t_n} \left(p_n^i + \frac{b_{p,n}^i}{a_{p,n}^i} \right) - \frac{b_{p,n}^i}{a_{p,n}^i}, & \text{if } |a_{p,n}^i| \geq \delta \\ p_n^i + \Delta t_n (a_{p,n}^i p_n^i + b_{p,n}^i), & \text{otherwise,} \end{cases} \quad (3.29)$$

$$a_{q,n}^j = a_q^j(\tilde{C}a_i(t_n - \delta_{q^j})), \quad (3.30)$$

$$b_{q,n}^j = b_q^j(\tilde{C}a_i(t_n - \delta_{q^j})), \quad (3.31)$$

$$q_{n+1}^j = \begin{cases} e^{a_{q,n}^j \Delta t_n} \left(q_n^j + \frac{b_{q,n}^j}{a_{q,n}^j} \right) - \frac{b_{q,n}^j}{a_{q,n}^j}, & \text{if } |a_{q,n}^j| \geq \delta \\ q_n^j + \Delta t_n (a_{q,n}^j q_n^j + b_{q,n}^j), & \text{otherwise,} \end{cases} \quad (3.32)$$

where $\tilde{V}(t_n - \delta_{p^i})$ and $\tilde{C}a_i(t_n - \delta_{q^j})$ are obtained from historical data, as described in the previous section.

3.4 Methods for wave propagation in tissue

In this work we present 1-dimensional (1D) and 2-dimensional (2D) wave propagation simulations in order to assess the proposed DDE formulations and the efficiency of the applied numerical techniques at the tissue level. In order to perform these experiments, we applied the finite differences method to discretize the monodomain model described by Eq. (2.25) and obtain explicit numerical schemes of simple parallel implementation.

The resulting scheme for 1D experiments in a ring geometry is given by

$$\begin{aligned} \frac{V_{n+1}^i - V_n^i}{\Delta t} &= D \frac{V_n^{i+1} - 2V_n^i + V_n^{i-1}}{\Delta x^2} - \frac{1}{C_m} I_{ion} \mathbf{f}(V_n^i, \mathbf{y}_n, t_n) \implies \\ \implies V_{n+1}^i &= V_n^i + D \frac{\Delta t}{\Delta x^2} (V_n^{i+1} - 2V_n^i + V_n^{i-1}) - \\ &\quad - \Delta t \frac{1}{C_m} [I_{ion}(V_n^i, \mathbf{y}_n, t_n) + I_{stim}(x, t)], \\ i &\in \{1, 2, \dots, N - 1\}, \end{aligned} \tag{3.33}$$

where Δx is the spatial discretization, Δt is the time discretization, V_n^i is the discretized membrane potential at $t = t_n$ and $x = i\Delta x$, N is the total number of discrete nodes, and I_{ion} is determined by the myocyte model. In this case the boundary condition is periodic, i.e.,

$$V_{n+1}^0 = V_{n+1}^N. \tag{3.34}$$

For the 2D case, a finite differences scheme with 9-point stencil was applied to the

approximate Laplacian operator, which results in the following formulation:

$$\begin{aligned}
V_{n+1}^i &= V_n^i + \frac{2}{3}D \frac{\Delta t}{\Delta x^2} (V_n^{i+1,j} - 2V_n^{i,j} + V_n^{i-1,j}) \\
&\quad + \frac{2}{3}D \frac{\Delta t}{\Delta y^2} (V_n^{i,j+1} - 2V_n^{i,j} + V_n^{i,j-1}) \\
&\quad + \frac{1}{6}D\Delta t \left(\frac{1}{\Delta x^2} + \frac{1}{\Delta y^2} \right) (V_n^{i-1,j-1} + V_n^{i-1,j+1} - 4V_n^{i,j} + V_n^{i+1,j-1} + V_n^{i+1,j+1}) \\
&\quad - \Delta t \frac{1}{C_m} [I_{ion}(V_n^i, \mathbf{y}_n, t_n) + I_{stim}(\mathbf{x}, t)], \\
&\quad (i, j) \in \{1, 2, \dots, N_x - 1\} \times \{1, 2, \dots, N_y - 1\}.
\end{aligned} \tag{3.35}$$

The no-flux boundary conditions was imposed through the use of the ghost points technique (Holmes, 2006).

3.4.1 *Initiation of spiral waves in 2D*

To initiate reentrant spiral waves in monodomain experiments, we applied an S1-S2 protocol. Consider a square two-dimensional domain of isotropic tissue. The protocol consists of (i) the application of a stimulus current to all cells located at the left border (S1), which initiates a planar wave that propagates towards the right edge, and (ii) the application of a second stimulus current (S2) after the refractory tail of the first wave reaches the middle of the media. This second stimulus is applied to all cells located in a rectangular region that is adjacent to the refractory tail of the first wave, as shown in Figure 3.1.

The bottom-left panel of Figure 3.1 shows that the refractory tail of the first wave blocks the right edge of the wave initiated by S2. Still, the second wave starts to propagate upwards. When the refractory tail of the first wave gets further to the right, the second wavefront is allowed to propagate rightwards, and a spiral wave is initiated, as shown in the bottom-right panel of Figure 3.1.

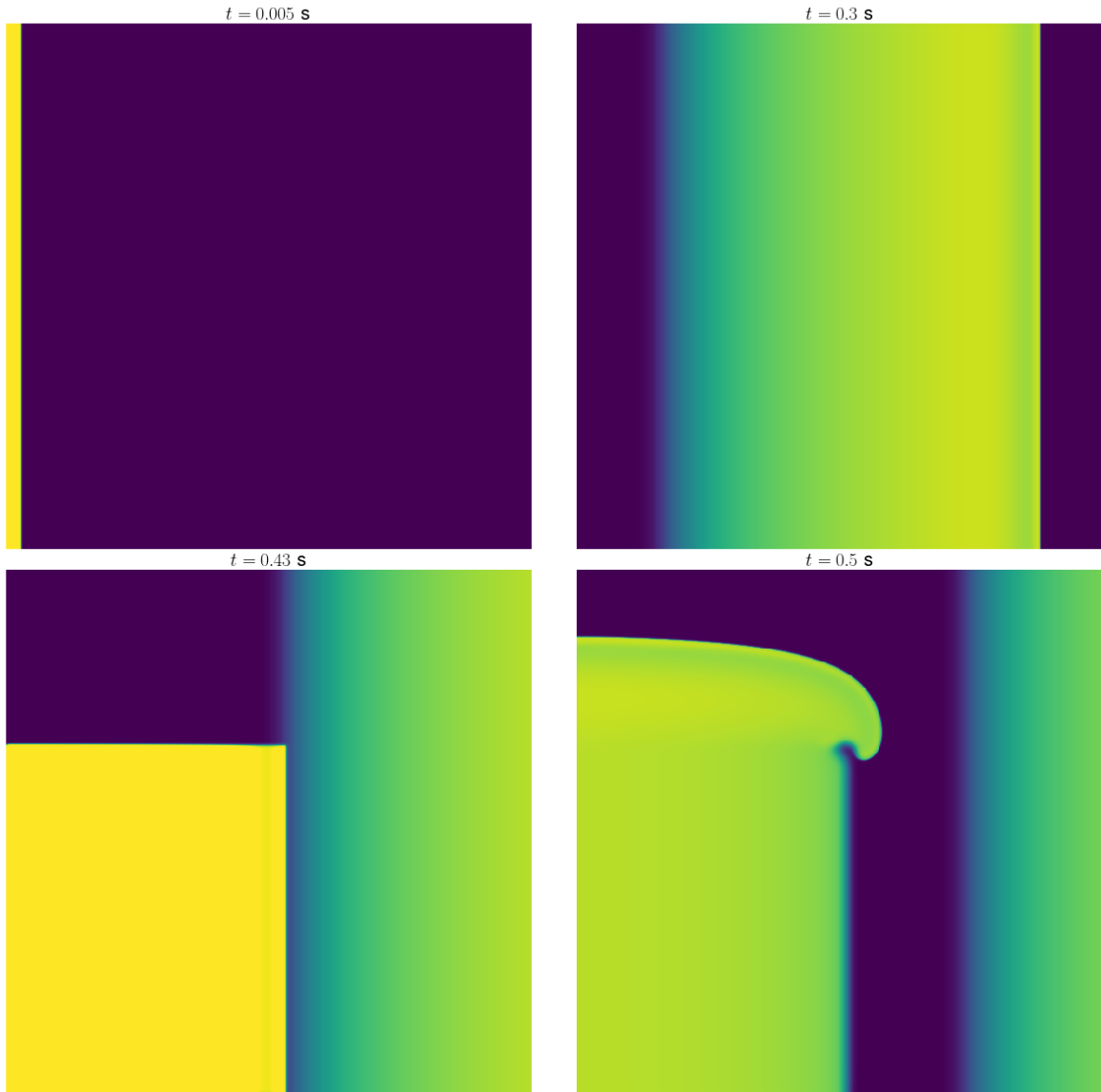


Figure 3.1: S1-S2 protocol for initiating a spiral wave in 2D.

3.5 Handling historical data in DDE-based simulations

As described in Section 3.3.1, the numerical solution of DDEs requires to maintain histories of variables that are referenced at previous times. In this research, these past-referenced variables are usually voltage or intracellular calcium. In tissue simulations, each node of the discretized spatial domain is required to keep its own version of history for each of the past-referenced variables, which significantly impacts the memory requirements of the computational experiment. In this section we propose history management algorithms

for reducing these memory requirements while keeping numerical errors under control.

3.5.1 Simple linear interpolation algorithm (SLIA)

This straightforward scheme consists of updating the history using a different time step Δt_{hist} that is a multiple of the integration time step Δt . With this approach, which we refer to as the *simple linear interpolation algorithm* (SLIA), the history is updated less often and interpolation must be used even if the delay is a multiple of the integration time step, thereby resulting in the addition of error through the approximation of past values.

3.5.2 Adaptive history management algorithm (AHMA)

This novel adaptive algorithm dynamically reduces the resolution of the delayed variable history while maintaining acceptable numerical accuracy. The method relies on two simultaneous strategies: the first one is to avoid adding new values to the history if the associated variable is changing slowly; the second one is to remove values from the history when they can be well approximated by linear interpolation.

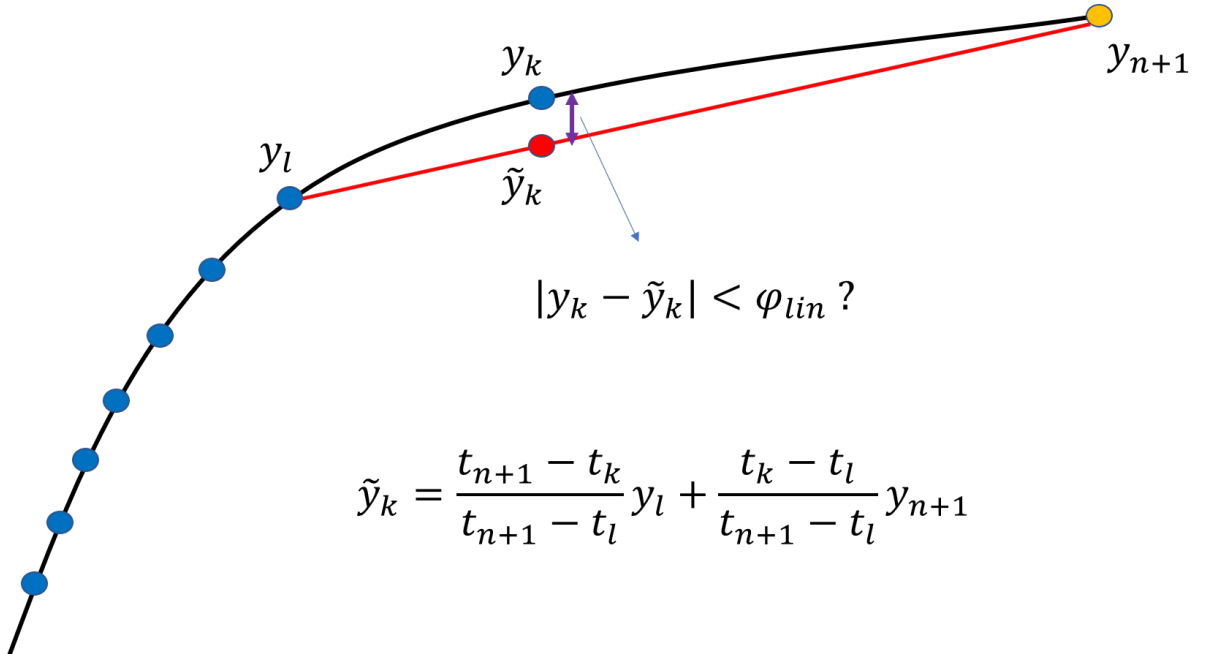


Figure 3.2: Values present in the history (blue dots) and newly computed value y_{n+1} with $|y_{n+1} - y_k| > \phi_{push}$. The adaptive algorithm decides if y_k can be approximated with sufficient accuracy by a linear interpolation of y_l and y_{n+1} .

At each step an approximation to $y(t_n - \delta)$ is computed from the history by linearly

interpolating between the two nearest stored values in time. After y_{n+1} is obtained from numerical integration, the first strategy is implemented by not storing y_{n+1} if $|y_{n+1} - y_k|$ is smaller than a predefined tolerance ϕ_{push} , where y_k is the most recently stored value in the history. Before storing y_{n+1} to the history, the second strategy is used to check whether y_k could be approximated within some tolerance ϕ_{lin} by linear interpolation between y_l and y_{n+1} , where y_l is the second most recently stored value (Fig. 3.2). If so, y_k is replaced by y_{n+1} in the history. Otherwise, y_k is maintained and the algorithm then determines whether the oldest value in the history, y_q , remains within the length of the delay at the new time. If not (that is, $t_q < (t_{n+1} - \delta)$), y_q is discarded and the history size remains constant. Otherwise, the history size is increased to accommodate the new value. This procedure is described by the algorithm in Fig. 3.3, which is executed after every step of numerical integration.

Algorithm 1 Adaptive History Management Algorithm

```

1: procedure UPDATEHISTORY( $hist_y$ ,  $hist_t$ ,  $y_{new}$ ,  $t_{new}$ ,
    $\phi_{push}$ ,  $\phi_{lin}$ )
2:    $y_k \leftarrow getNewestValue(hist_y)$ 
3:    $t_k \leftarrow getNewestValue(hist_t)$ 
4:   if  $abs(y_{new} - y_k) \geq \phi_{push}$  then
5:      $y_l \leftarrow getSecondNewestValue(hist_y)$ 
6:      $t_l \leftarrow getSecondNewestValue(hist_t)$ 
7:      $\tilde{y}_k \leftarrow \frac{t_{new} - t_k}{t_{new} - t_l} y_l + \frac{t_k - t_l}{t_{new} - t_l} y_{new}$ 
8:     if  $abs(y_k - \tilde{y}_k) < \phi_{lin}$  then
9:        $removeNewestValue(hist_y)$ 
10:       $removeNewestValue(hist_t)$ 
11:       $storeNewValue(hist_y, y_{new})$ 
12:       $storeNewValue(hist_t, t_{new})$ 

```

Figure 3.3: Algorithm illustrating how the AHMA handles local histories updates.

In order to take advantage of the fact that action potentials have a brief depolarization phase followed by a longer repolarization phase, our implementation of the AHMA utilizes three distinct tolerances (instead of two) when voltage V is the delayed variable. In that

case, ϕ_{lin} is split into an upstroke tolerance $\phi_{lin,u}$ and a downstroke tolerance $\phi_{lin,d}$.

Since the update rate of the history is not constant, the AHMA requires that each value y_p is stored alongside with its associated time t_p , which will increase the memory needed. Thus, it is important to ensure that the added memory requirement of storing the time is overcome by the savings provided by the scheme.

3.5.2.1 Memory management implementations

Since the AHMA requires a variable number of stored values at runtime, a possible data structure to use is a linked list. However, its use could increase the computational cost of tissue simulations due to the high number of memory jumps occurring as multiple computational nodes retrieve values from their local histories. In addition, more memory would be required to store the linking pointers of the data structure.

An alternative to linked lists would be the use of fixed-size contiguous arrays. The predefined length of the local histories should be greater than the maximum number of entries the algorithm would require with the use of linked lists, which could be determined by previous experimentation.

In the case of action potential models it can be observed that voltage-dependent variables undergo rapid changes during the depolarization phase when the voltage changes on the order of 100 mV. For this reason it would be both useful and efficient to use two types of history: (i) a short local history for each node of the discretized spatial domain with sufficient memory for the repolarization phase (which represents most of the action potential; for large mammals it is about two orders of magnitude longer than depolarization) and (ii) a set of long arrays that are shared amongst the nodes only during the depolarization phase. Given that the cardiac wavelength is long relative to the width of the wave front, only a fraction of the total tissue will contain wave fronts, so that the number of required long shared arrays is much lower than the total number of nodes. The algorithm does not require determining the locations of wave fronts; instead, when a new value is being added to the short local history array and it is already fully utilized, the algorithm makes the transition to a long shared array. Note that in these cases, because

their lengths are fixed, the arrays may include entries farther back in time than the delay value.

In summary, we designed four implementations to manage memory used to store historical values:

1. **Linked List Implementation (LLI):** This version implements a circular linked list for the history associated with the delayed variable. Each entry of the list contains a mesh value y_k and its corresponding time t_k . The list is always ordered from oldest to newest, with the newest entry pointing back to the oldest. Each node of the spatial domain has a pointer to the newest entry in its history, which gives fast access to the newest values for adding entries and to the oldest values for accessing and removing entries. Every time a value is stored in the list, the algorithm removes any old entry that is not longer needed because its time is earlier than the delayed time value currently needed.
2. **Simple Contiguous Array Implementation (SCAI):** The algorithm utilizes a contiguous array with a predefined length based on the maximum number of entries that would be required by the AHMA. The array is ordered from oldest to newest, but the starting position pointer changes as new entries are added: a new entry replaces the oldest entry and the next location in the array is set to be new starting position of the history. When the new entry is added to the last array location, the new starting position in the history will be the first location in the array.
3. **Shared Memory Pool Implementation (SMPI):** This implementation applies the same idea as SCAI, but two types of array are utilized: (i) a short local array for each computational node of the discretized domain, with enough entries for storing values during the repolarization phase; and (ii) a long shared array that is used during the depolarization phase. The number of arrays in the shared pool is typically much smaller than the number of computational nodes because only a small fraction of the tissue requires depolarization history at the same time. The algorithm must manage the transitions between local arrays and shared arrays and

vice versa.

4. Dynamic Array Implementation (DAI): In this approach, contiguous arrays are utilized as in SCAI, but the algorithm switches between two predefined lengths (short and long) as needed. When the algorithm demands more frequent history updates (depolarization), a long array is dynamically created, the values from the short array are copied to it and the short array is dynamically destroyed. When the long array is no longer needed, a short array is created, the needed values are copied to it and the long array is destroyed. Figure 3.4 illustrates this process of dynamic allocation in a scenario where a single wave is propagating through a cable.

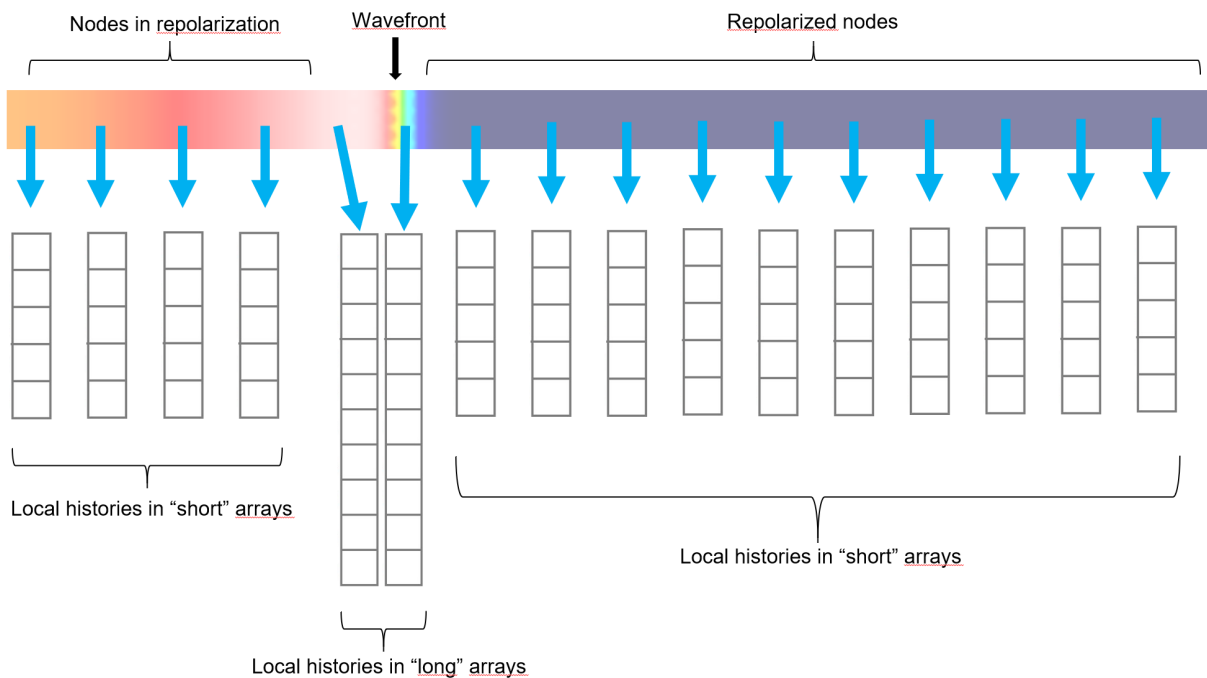


Figure 3.4: Schematic of a DDE-based wave propagation simulation on a cable using the Dynamic Array Implementation (DAI) for the Adaptive History Management Algorithm (AHMA).

3.6 Parallel implementations

Computing the electrical activity of the cardiac tissue involves the numerical solution of nonlinear partial differential equations in complex spatial domains and represents a big challenge in terms of computational performance. With the use of parallel computing,

it is possible to distribute such complex workload across multiple processing units in order to obtain significant gains in performance (Petersen - Arbenz, 2004). In this work we developed parallel implementations of the proposed techniques for DDE-based tissue simulations, aiming for efficiency both in terms of memory and computation time.

3.6.1 OpenMP implementations

OpenMP is an open application programming interface (API) that provides support for shared memory multiprocessing computing in C, C++ and Fortran. The use of OpenMP allows for simple portable parallel implementations for a wide variety of multi-CPU environments.

We developed OpenMP implementations for all the presented 2D experiments of the monodomain model that were performed on a CPU, so that a sufficiently large domain could be computed in an acceptable amount of time. Since the applied numerical scheme given by Equation 3.35 is explicit, distributing the workload among multiple threads was as simple as partitioning the domain into equally sized tissue slices across either the x-axis or y-axis.

All OpenMP experiments were performed on a computer with a 16-core AMD Threadripper processor clocked at 4GHz and 32GB of memory, running Linux Debian.

3.6.2 GPU implementations

The use of graphical processing units (GPUs) in computational cardiac modeling has become increasingly popular in the past few years as significant gains in performance have been reported in recent studies involving the monodomain model (Sato *et al.*, 2009; Rocha *et al.*, 2010; Oliveira *et al.*, 2016) and the bidomain model (Neic *et al.*, 2012; Amorim - dos Santos, 2013).

CUDA from NVIDIA is one of the most popular platforms and programming models for GPU computing, since it includes several toolkits and libraries for developing efficient massively parallel applications for both professional and consumer graphics cards. A typical GPU includes from several hundreds to a few thousands of floating-point units



Figure 3.5: Microarchitecture of the NVIDIA Pascal (NVIDIA, 2016) streaming multiprocessor, including 64 single-precision units (cores), 16 special function units (SFUs), and 32 double-precision units (adapted from NVIDIA (2016)).

(FPUs) that are grouped into a number of streaming multiprocessors (SMs). This large number of FPUs is well suited for arithmetic-intensive and highly parallel workloads. Figure 3.5 shows how these FPUs are organized in a stream multiprocessor of the Pascal GPU microarchitecture from NVIDIA.

The CUDA programming model requires the developer to divide their workload into multiple threads and to group them into structures called blocks. Each block must contain a number of threads that is multiple of 32, since the SMs schedulers always issue instructions in groups of 32 threads called warps. As shown in Figure 3.6, each thread block is executed in a single SM, which means its threads share some memory resources of that block, including L1 cache and shared memory. Communication between different blocks is established through the GPU global memory and L2 cache.

In this work we developed NVIDIA CUDA implementations of the history management algorithms presented in Section 3.5 in order to assess the performance of DDE-based tissue

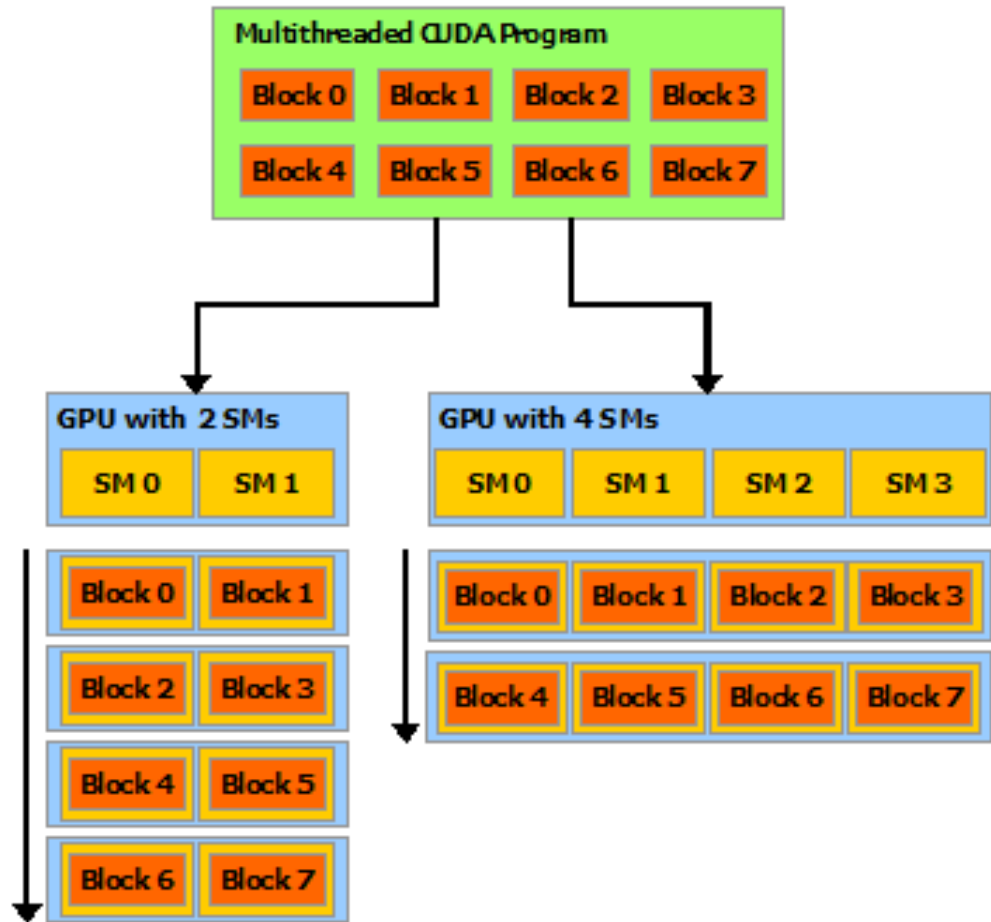


Figure 3.6: NVIDIA CUDA programming model and blocks scheduling (adapted from NVIDIA (2016)).

simulations on standard GPU devices. All 2D simulations of electrophysiological activity were performed on a Pascal GPU (GTX 1080 Ti). The kernels were organized into blocks of 64 threads each, since using 128 or more threads per block resulted in lower performance. The shared memory of the streaming multiprocessors, which has lower latency than the global memory, was used to accommodate the nodes' histories in DDE-based experiments.

3.7 Metrics

3.7.1 APD restitution analysis

In order to assess how the many models studied in this research behave in terms of APD as a function of CL, we applied a down-sweep pacing protocol (Tolkacheva *et al.*, 2003) starting from a sufficiently large CL that allowed full repolarization between action

potentials and then reducing the CL in steps of ΔCL after reaching steady-state. The step size ΔCL varies from 2 to 5 ms depending on how the model is sensitive to CL changes. The process stops when the pacing rate is so fast that action potential blocks start to occur. The action potential duration was measured using the APD_{80} metric, which is the time it takes for the membrane to repolarize in 80% since the upstroke.

3.7.2 *Period distributions*

In this work, we have computed period distributions (or period spectra) from two-dimensional spiral wave simulations in order to quantify the effects of delays in terms of dominant frequency and period range. The period samples for a distribution plot were obtained by computing the time between depolarizations of each domain node during the entire simulation (Bueno-Orovio *et al.*, 2008).

Figure 3.7 shows the period distribution obtained from 5 seconds of spiral wave activity using the ten Tusscher *et al.* (2004) model on a 24 cm \times 24 cm isotropic tissue. The plot indicates a dominant period of about 274 ms and a period range of approximately 12.5 ms.

3.7.3 *Spiral wave tip tracking*

The tip of a spiral wave can be defined as the point of zero normal velocity along an isopotential boundary that separates the tissue between depolarized and repolarized regions (Fenton - Karma, 1998). In this work, we used the zero-normal-velocity method proposed by Fenton - Karma (1998) to determine spiral wave tip locations for plotting and comparing the trajectories of spiral waves from different scenarios of tissue simulation. As an example, Figure 3.8 shows spiral wave tip trajectories from different configurations of the FitzHugh-Nagumo model (FitzHugh, 1961).

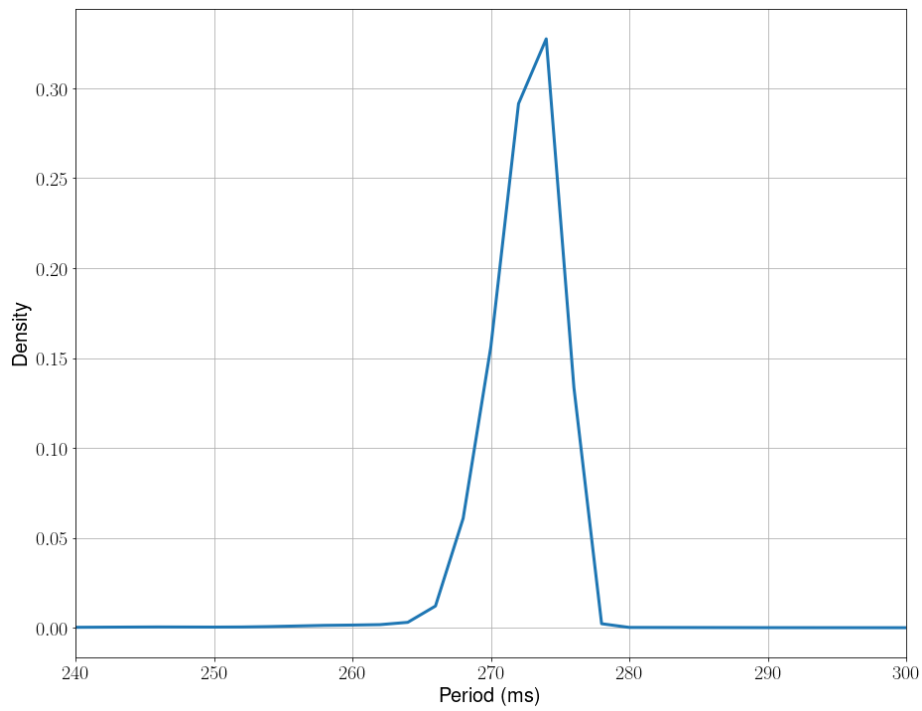
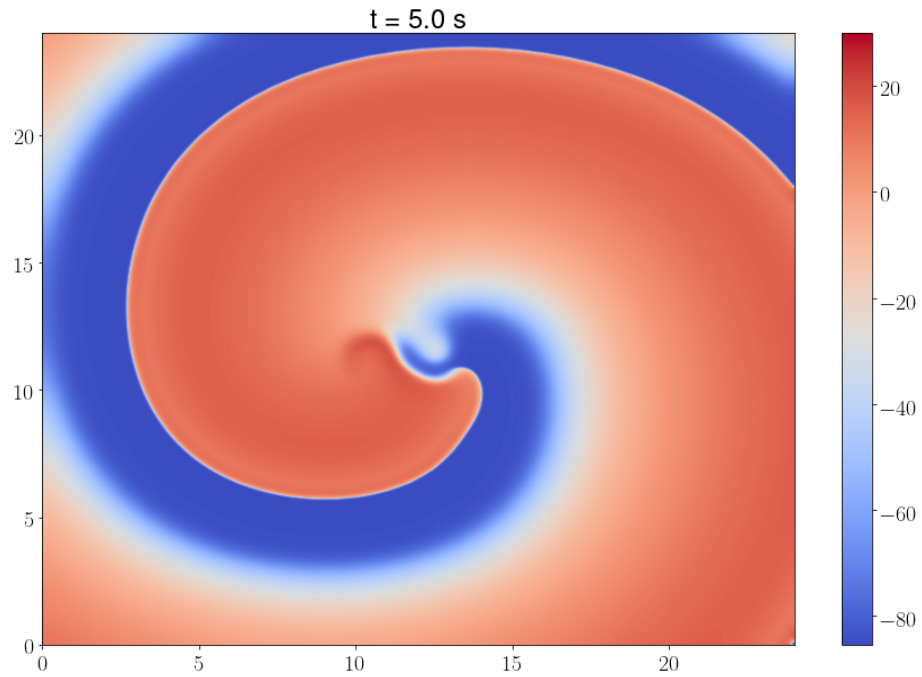


Figure 3.7: Two-dimensional simulation of 5 seconds of spiral wave activity from the model by ten Tusscher *et al.* (2004): (a) snapshot of membrane potentials at $t = 5 \text{ s}$ and (b) the obtained period distribution across the entire domain.

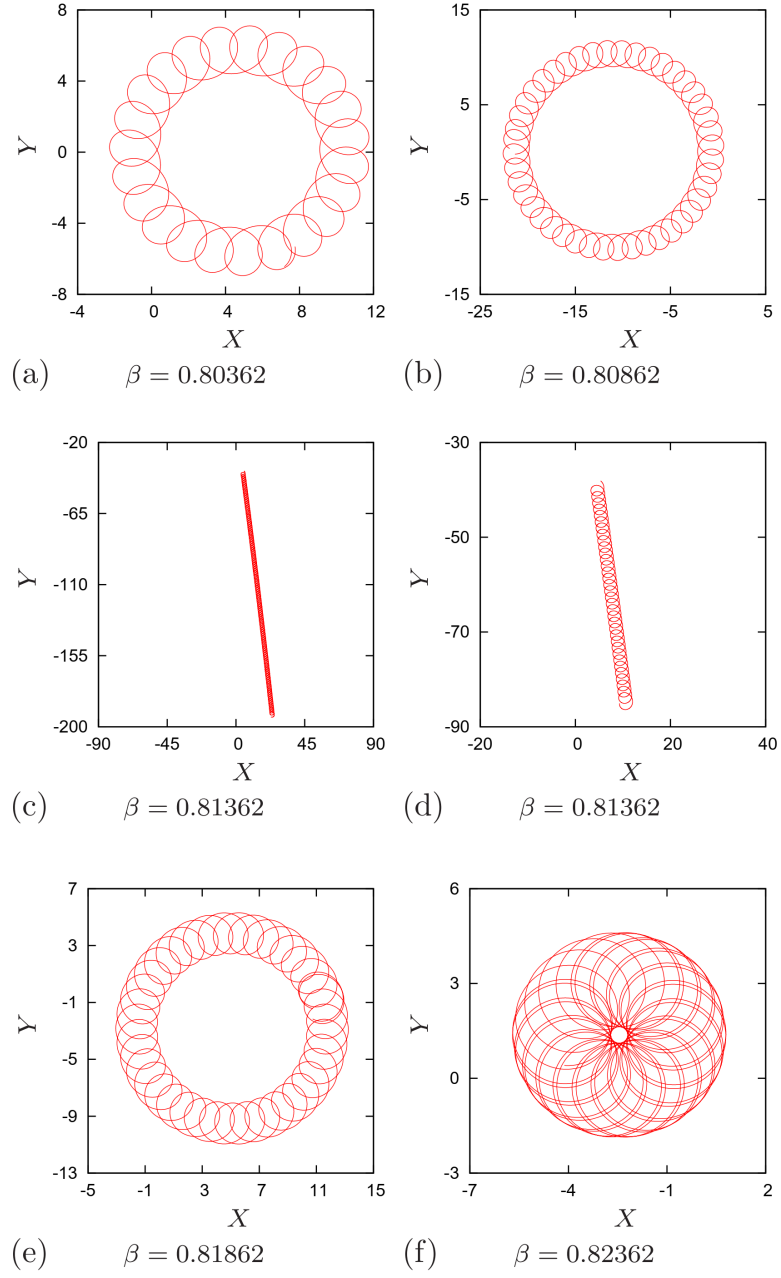


Figure 3.8: Spiral tip trajectories from simulations of the FitzHugh-Nagumo system (FitzHugh, 1961) with varying parameter β (adapted from Foulkes - Biktashev (2010)).

3.7.4 Error calculation

In the present work, every numerical error of a variable y from a given test solution with respect to a reference solution was calculated using the relative l^2 -norm:

$$error_y = \frac{\sqrt{\sum_{k=1}^N (y_k^{Ref} - y_k)^2}}{\sqrt{\sum_{k=1}^N (y_k^{Ref})^2}}, \quad (3.36)$$

where y_k and y_k^{Ref} are samples of the test solution and the reference solution, respectively, and N is the total number of samples for each solution. The chosen sampling step was $\Delta t_{save} = 1$ ms.

3.7.5 Measuring performance

All computation times presented in this manuscript were obtained from the average of three identically configured runs. Information regarding the memory use of historical data in DDE-based simulations was obtained by monitoring the number of data structures that were allocated at runtime.

4 Results

4.1 DDE-induced alternans in single cell models

In this section we cover an important application of the DDE-based formulations presented in Section 3.2, which is alternans induction in single cell models through delays. The section is divided into two parts: (i) experiments with models that are naturally able to exhibit alternans and this behavior is either restored or enhanced by the use of DDEs, and (ii) alternans promotion in models that are not originally able to produce this phenomena.

4.1.1 Alternans restoration in Hodgkin-Huxley-based models

4.1.1.1 DDE implementations for the Fox et al. model

The canine ventricular model proposed by Fox *et al.* (2002) exhibits stable alternans in its originally published parameter configuration, but the alternans can be suppressed by modifying ion channel maximum conductances. Figure 4.1 compares the original model with an alternans-suppressed version in which the maximum conductivity \bar{g}_{Kr} of the rapid delayed rectifier potassium current I_{Kr} is doubled. Fig. 4.1A compares steady-state action potentials from both versions at a pacing period of 180 ms, where the alternans-suppressed version exhibits a constant action potential shape and duration, while strong alternans can be noticed for the original version. Figure 4.1B shows a range of cycle lengths that produces alternans in the original model, while the APDs of the alternans-suppressed version are monotonically decreased as the pacing rate is increased.

We analyzed the effects of applying the DDE-based formulation presented in Section 3.2 to the previously described alternans-suppressed version of the Fox et al. model. Delays were introduced into each of the ten gating variables of the model: the L-type calcium current I_{Ca} activation gate d and inactivation gates f and f_{Ca} ; the fast sodium current I_{Na} activation gate m and inactivation gates h and j ; X_{Kr} and X_{Ks} , the activation gates for the rapid and slow components I_{Kr} and I_{Ks} of the delayed rectifier

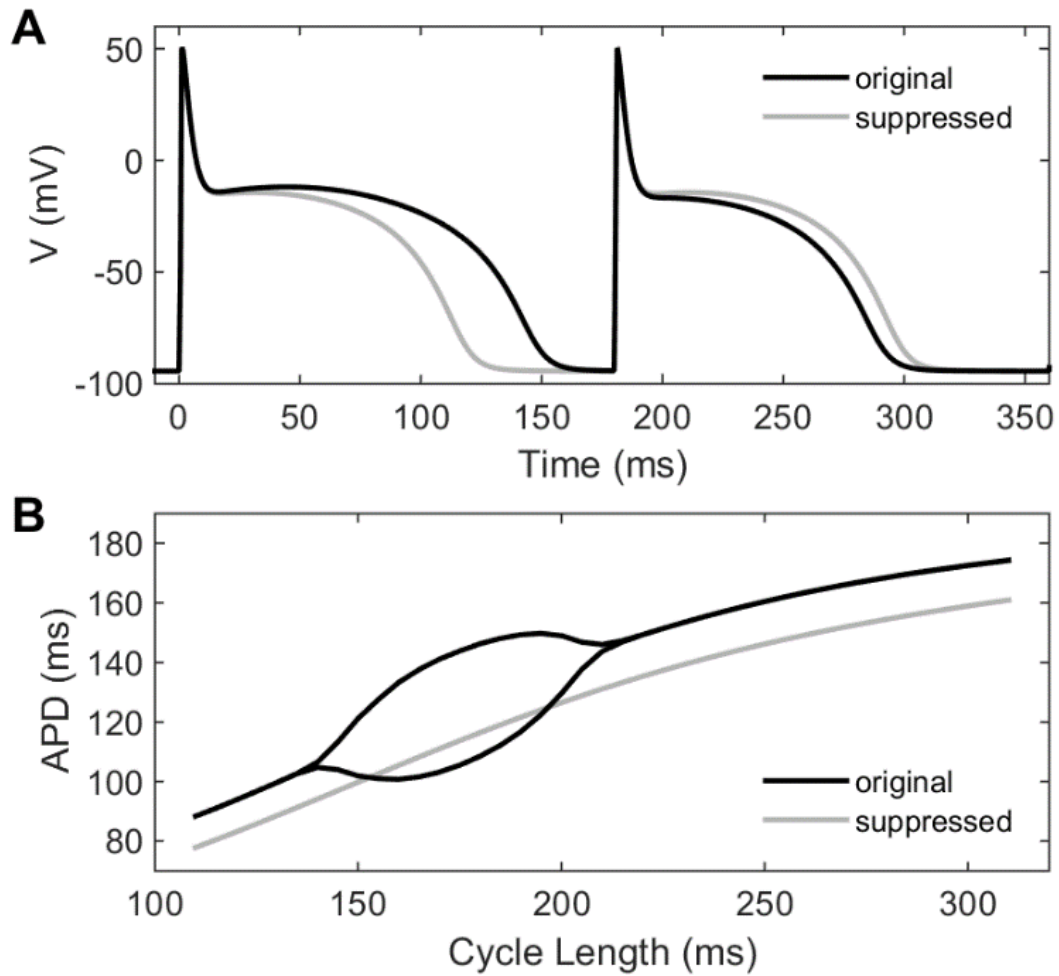


Figure 4.1: (A) Action potentials from the model by Fox *et al.* (2002) for 10s at a constant cycle length of 180 ms: original model versus version with doubled \bar{g}_{Kr} . (B) Bifurcation diagrams of the original Fox *et al.* (2002) model and of the version with alternans suppressed by doubling \bar{g}_{Kr} .

potassium current, respectively; the activation and inactivation gates of the transient outward potassium current X_{to} and Y_{to} , respectively; and K_1^∞ , the steady-state activation function of the inward rectifier potassium current I_{K1} .

By implementing DDEs for the I_{Ca} voltage-dependent gates f and d , it was possible to restore alternans in the version with doubled \bar{g}_{Kr} , as shown in Figure 4.2. For the case with delayed f gate, it was possible to induce alternans using a delay as short as 9 ms, as shown in Figure 4.3. Also, the alternans most closely resembled the original version for a delay of about 15 ms, but the APDs remained shorter in general because of the increased repolarizing current I_{Kr} (Fig. 4.1A). For the version with delayed d gate, alternans could be induced by using smaller delays (about 4 ms, as shown in Fig. 4.3), but the action

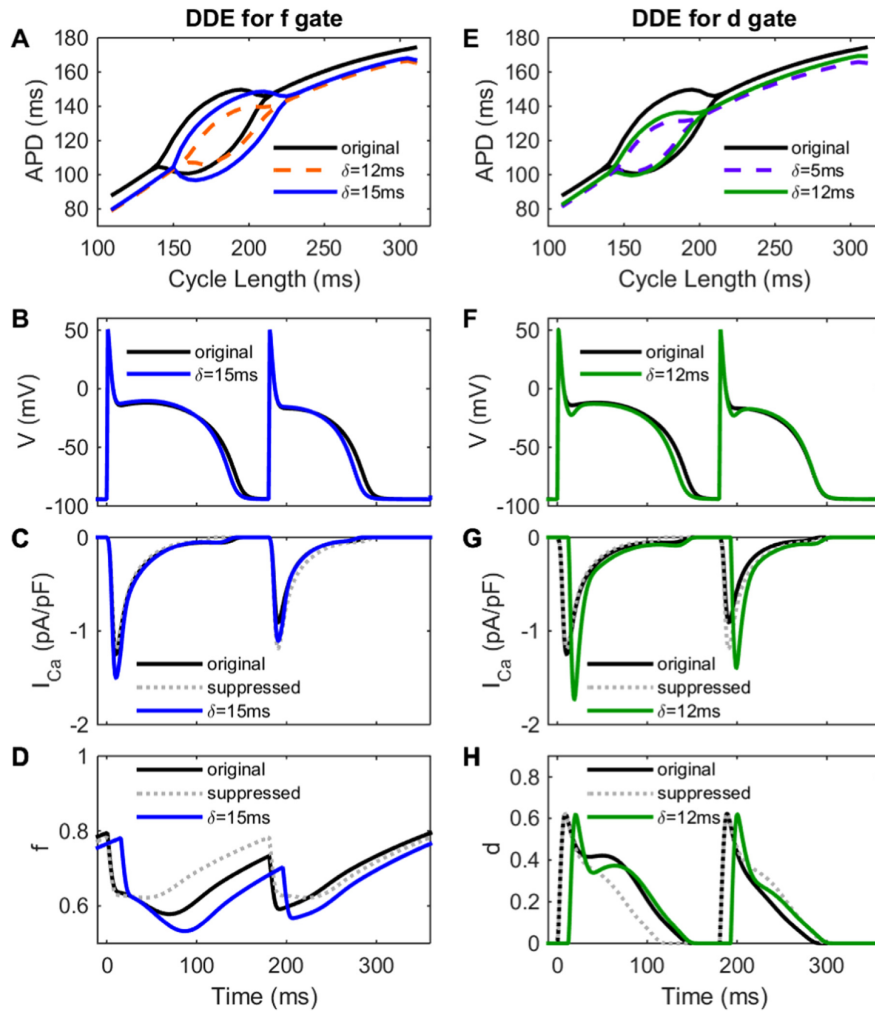


Figure 4.2: Alternans promotion by introducing delays into the f and d gates of the Fox et al. model: (A,E) bifurcation diagrams from the original Fox et al. models against alternans-suppressed version with DDE implementation for the f gate (A) and the d gate (E); (B,F) steady-state successive action potentials at a cycle length of 180 ms; (C,G) I_{Ca} corresponding to the successive action potentials in panels (B) and (F); (D,H) gating variables from the original and alternans-suppressed versions compared to the versions using delays of 15 ms and 12 ms, respectively.

potential shape was more severely altered since the delayed activation of I_{Ca} allowed a greater initial repolarization following the action potential upstroke (Fig. 4.1F,G). It was also possible to initiate alternans by delaying the calcium-dependent inactivation gate of the I_{Ca} current. The model was more sensitive to delays in this variable, with alternans beginning at a delay of 3 ms, as shown in Fig. 4.3.

We have also tested delaying the three I_{Ca} gating variables as a group rather than separately. Delays were added to all possible pairings of two of these variables as well as to all three, using the same delay value in each DDE. Alternans could be initiated in

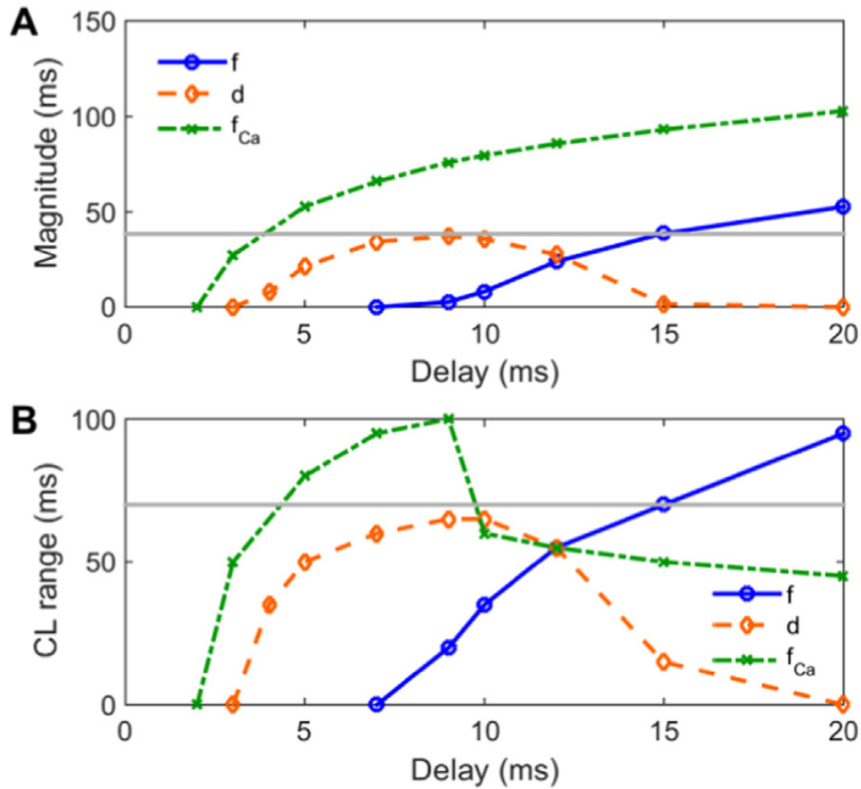


Figure 4.3: Alternans magnitude (A) and CL range exhibiting alternans (B) for delaying f , d , and f_{Ca} gates in Fox et al. model with doubled \bar{g}_{Kr} . The gray lines indicate the values for the original model.

each of the four resulting combinations, as shown in Fig. 4.4. The minimum delay value for giving rise to alternans in each of the cases was 3 ms for all groups that included f_{Ca} , except for the case where only the d and f gates were delayed, where a minimum delay of 4 ms was necessary to initiate alternans.

Delaying the steady-state activation gate I_{K_1} also promoted alternans, but for a very small range of delays (from 1.3 ms to 2.5 ms). In the original model, the gate responds instantaneously to changes in voltage, so even small delays can produce significant physiological effects. Delaying the other gating variables associated with potassium currents (X_{Kr} , X_{Ks} , X_{to} , and Y_{to}) by up to 20 ms did not produce alternans since these modifications all resulted in significant action potential shortening, which led to stronger diastolic intervals and complete recovery of the gating variables.

Delaying the sodium inactivation gates h and j also shortened the action potential, and adding delays to the I_{Na} activation gate m impaired the development of the action

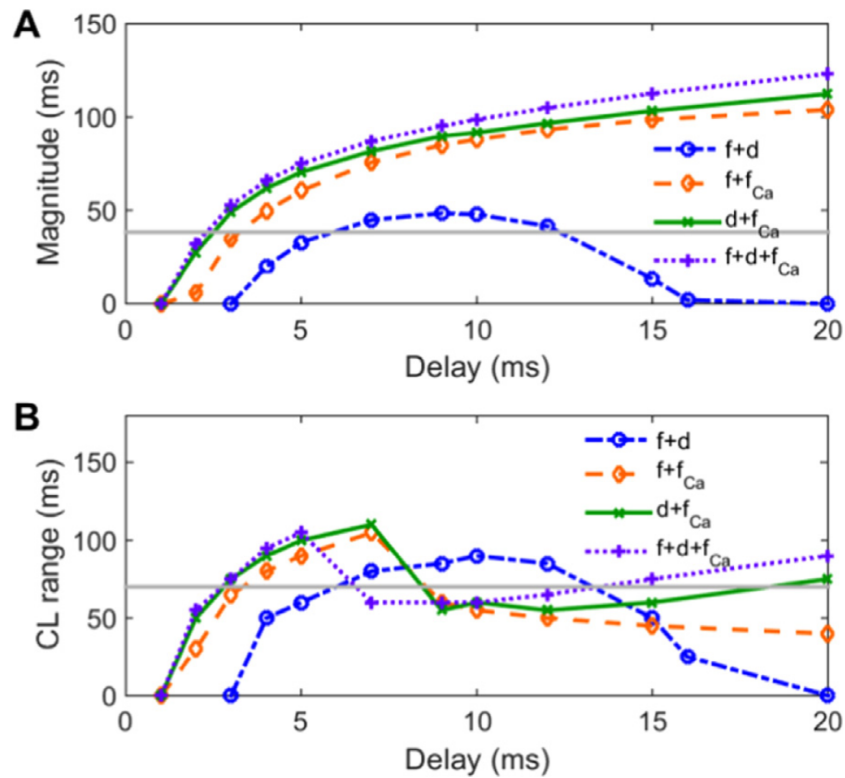


Figure 4.4: Alternans magnitude (A) and CL range exhibiting alternans (B) for delaying groups of I_{Ca} gates in Fox *et al.* model with doubled \bar{g}_{Kr} . The gray lines indicate the values for the original model.

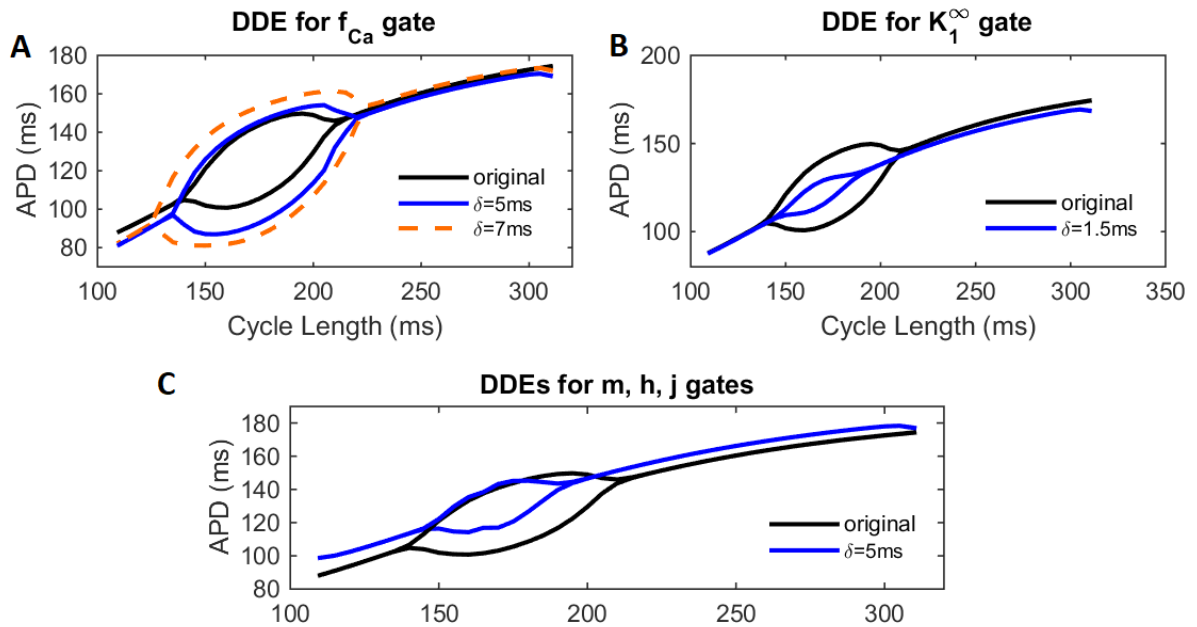


Figure 4.5: Bifurcation diagrams for the Fox *et al.* (2002) model comparing the original version with the an alternans-suppressed suppressed version using the DDE formulation for (A) I_{Ca} inactivation gate f ; (B) I_{Ca} activation gate d ; (C) I_{Ca} calcium-dependent inactivation gate f_{Ca} ; (D) I_{K1} gate K_1^∞ ; (E) I_{Na} gates m , h and j .

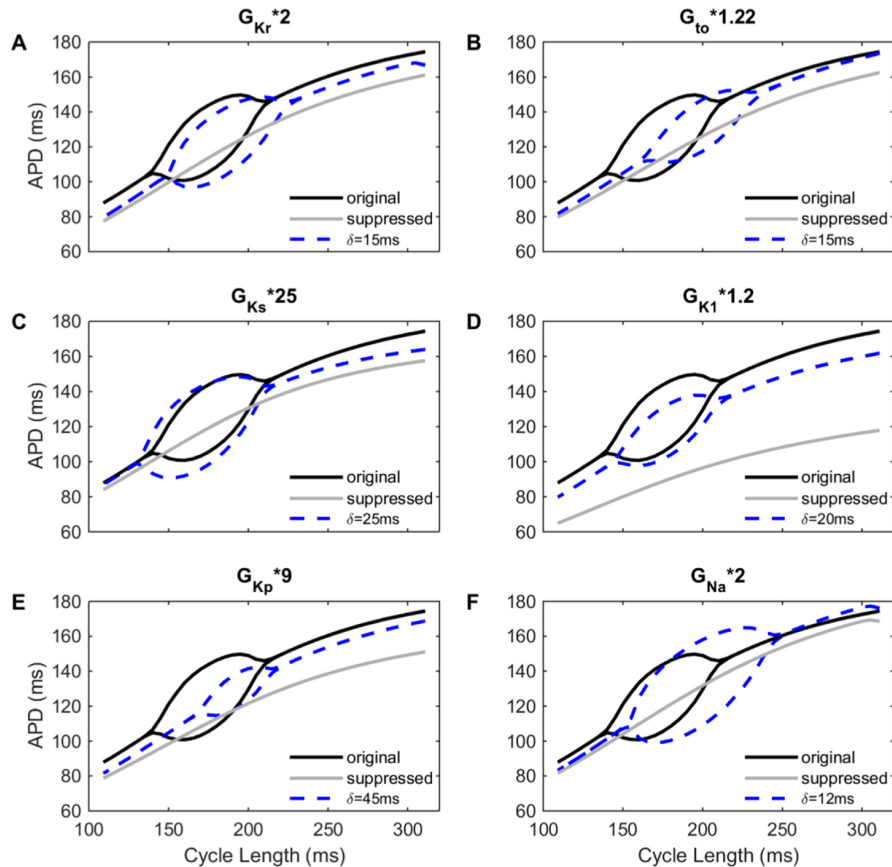


Figure 4.6: Robustness of the DDE-based formulation to promote alternans for different alternans suppression methods. Delays were added to the f gate in the following alternans-suppressed versions: (A) doubled \bar{g}_{Kr} ; (B) \bar{g}_{to} increased by a factor of 1.22; (C) \bar{g}_{Ks} increased by a factor of 25; (D) \bar{g}_{K1} increased by a factor of 1.2; (E) \bar{g}_{Kp} increased by a factor of 9; and (F) doubled \bar{g}_{Na} .

potential by reducing overall current. The same result was observed when delaying all sodium gating variables as a group. However, increasing the fast sodium current conductance \bar{g}_{Na} in the original model consists of an alternative method for suppressing alternans, as described in the original manuscript (Fox *et al.*, 2002). Therefore, we considered an alternans-suppressed version of the model with doubled \bar{g}_{Na} and applied delays to all sodium gates simultaneously, which successfully restored alternans for delays in the range of 2-6 ms. Figure 4.5 presents bifurcation diagrams from cases where alternans could be restored by delaying the calcium-dependent I_{Ca} inactivation gate, the I_{K1} steady-state activation gate K_1^∞ , and all the sodium gating variables as a group.

In order to assess the robustness of the DDE-based technique for promoting alternans, we produced a total of six alternans-suppressed versions of the Fox *et al.* model by

modifying different maximum conductances and applied delays to the calcium voltage-dependent inactivation gate f . The results are shown in Figure 4.6, where the different alternans-suppressed versions are compared to versions with DDE implementation of the f gate and the original model. We published these and other results for the Fox et al. model in Eastman *et al.* (2016) where more details can be found.

4.1.1.2 Adding delays to other five HH-based models

In order to verify if the results presented in the previous section are model-specific, we applied the proposed DDE-based formulation to other five different Hodgkin-Huxley-based models: the action-potential and pacemaker model for cardiac Purkinje fibers proposed by Noble (1962), the mammalian ventricular action-potential models by Beeler - Reuter (1977) and Luo - Rudy (1991), the electrophysiology model of the canine Purkinje cell proposed by Li - Rudy (2011), and the reduced human ventricular cell model by Tusscher - Panfilov (2006).

The Noble (1962) model can generate pacemaker potentials in response to an initial stimulus with a frequency of about 1.2 Hz. It is possible to force the system to oscillate with higher frequencies by applying a periodic stimulus current. The model exhibits alternans if a fast pacing rate is applied and it can be suppressed by increasing the maximum conductance of the time-dependent potassium current \bar{g}_{K_2} by a factor of 1.2, as shown in Fig. 4.7a-b. It is possible to restore alternans in the alternans-suppressed model by applying a DDE formulation to the variable $K_{1\infty}$, which is the quasi-gate of the time-independent potassium current I_{K_1} (see Fig. 4.7c-d). Alternans can be initiated for delays greater than 10 ms, although the action potential is blocked if delays greater than 15 ms are applied. Figures 4.8a and 4.8b show the maximum alternans magnitude and the CL range of alternans as a function of delay size with a DDE formulation for $K_{1\infty}$. It can be seen that for $\delta > 10$ ms, both quantities increase monotonically for the range of delays shown.

Using a DDE for the n gate (I_{K_2} current) did not give rise to alternans. Delays were also added to the sodium gates m and h . Delaying m did not produce alternans and for

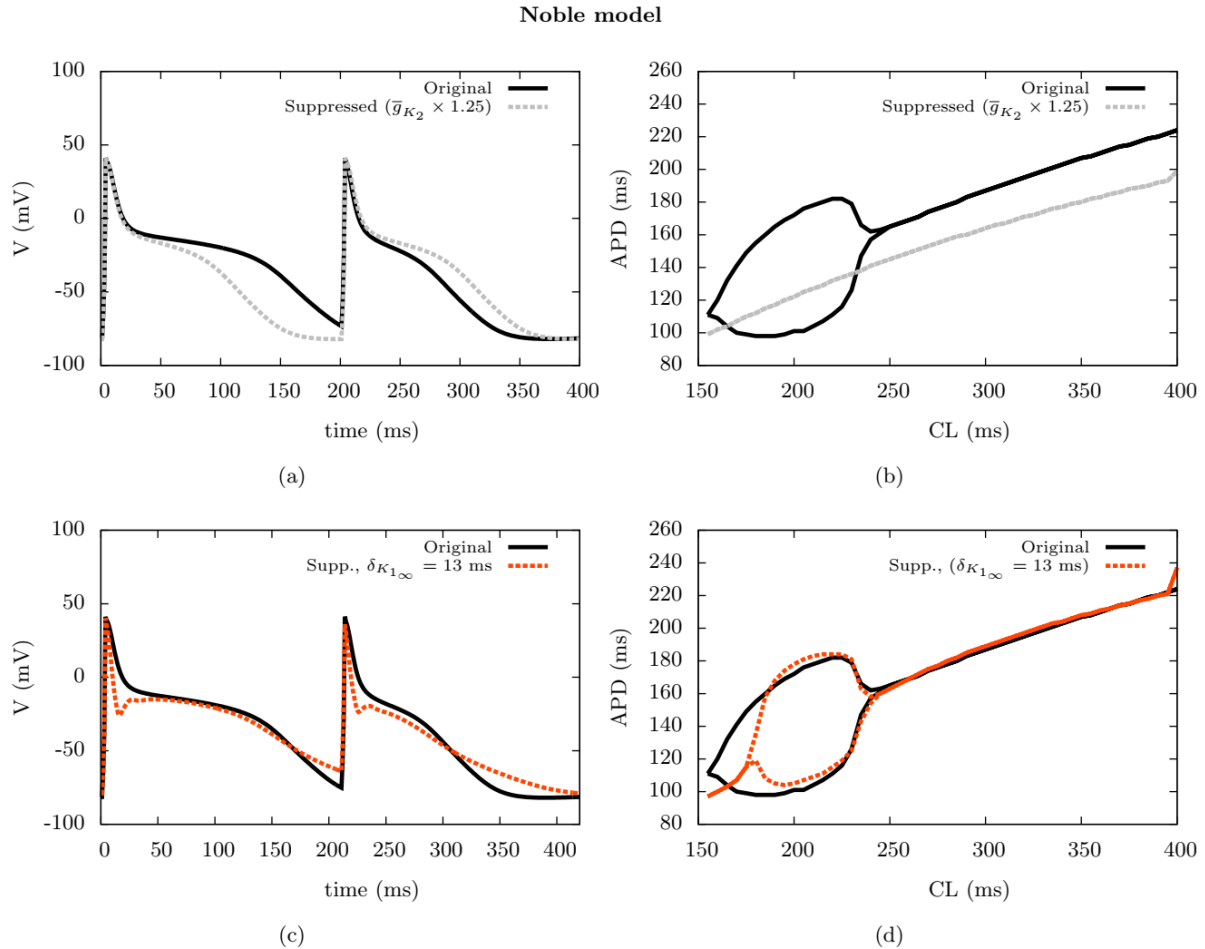
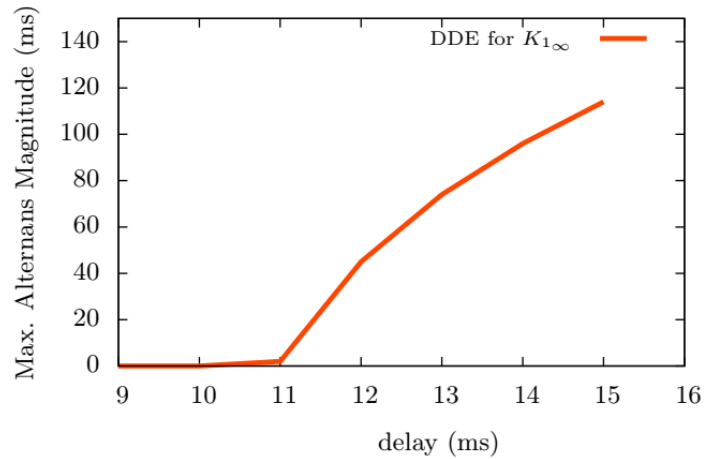


Figure 4.7: (a) Action potentials from the Noble model with a cycle length of 200 ms: original version (solid) and alternans suppressed version ($\bar{g}_{K_2} \times 1.25$, dashed). (b) Bifurcation plots for the original and alternans-suppressed versions. (c) Action potentials for the original and suppressed version with a DDE for $K_{1\infty}$, with CL = 210 ms. (d) Bifurcation plots for the original Noble model and suppressed version with a DDE for $K_{1\infty}$.

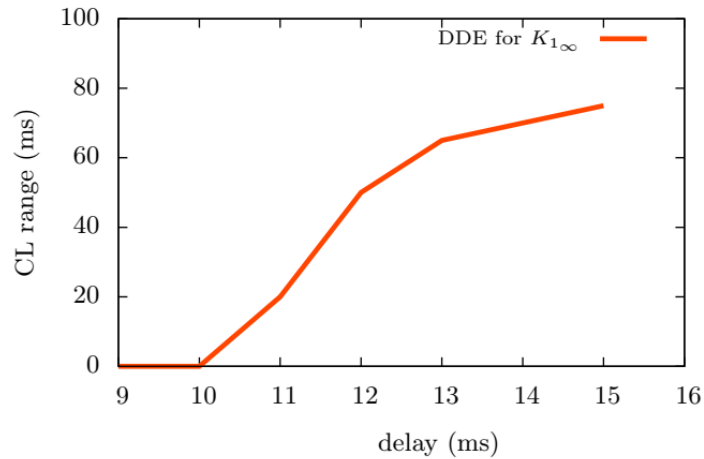
$\delta \geq 10$ ms, the development of action potentials was impaired. Delaying h with by up to 20 ms did not result in alternans. We also applied delays to both m and h together, and the results are similar to those obtained with m delayed separately.

The Beeler - Reuter (1977) model exhibits alternans when stimulated with a pacing period lower than 265 ms, and alternans can be suppressed in the model by increasing potassium conductivities, and ergo shortening the APDs. As in previous cases, the alternans-suppressed version can give rise to alternans by the introduction of delays in the ion channel formulations. Figure 4.9 shows the two cases where alternans could be produced by using delays: delaying the I_s inactivation gate (f) and delaying the I_{x_1}

Noble model: alternans *vs* delay size



(a)



(b)

Figure 4.8: Alternans properties of the suppressed Noble model with a DDE for the $K_{1\infty}$ variable. (a) Maximum alternans magnitude as a function of delay. (b) Alternans CL range as a function of delay.

activation gate (x_1). In both cases, the APDs were only slightly changed with respect to the suppressed version in the pre-alternans phase. Alternans could not be induced by delaying the I_s activation gate d with delay values up to 20 ms, but delaying the f gate promoted strong alternans. Figure 4.9b shows the maximum alternans magnitude as a function of delay from the DDE versions of the model that were successful at inducing alternans. The magnitude and the CL range increase with delay size for both cases in the given range of delays (Fig. 4.9b-c).

By delaying the sodium current activation gate m with delays greater than 1 ms, the action potential amplitude and duration were severely reduced, so that no alternans was

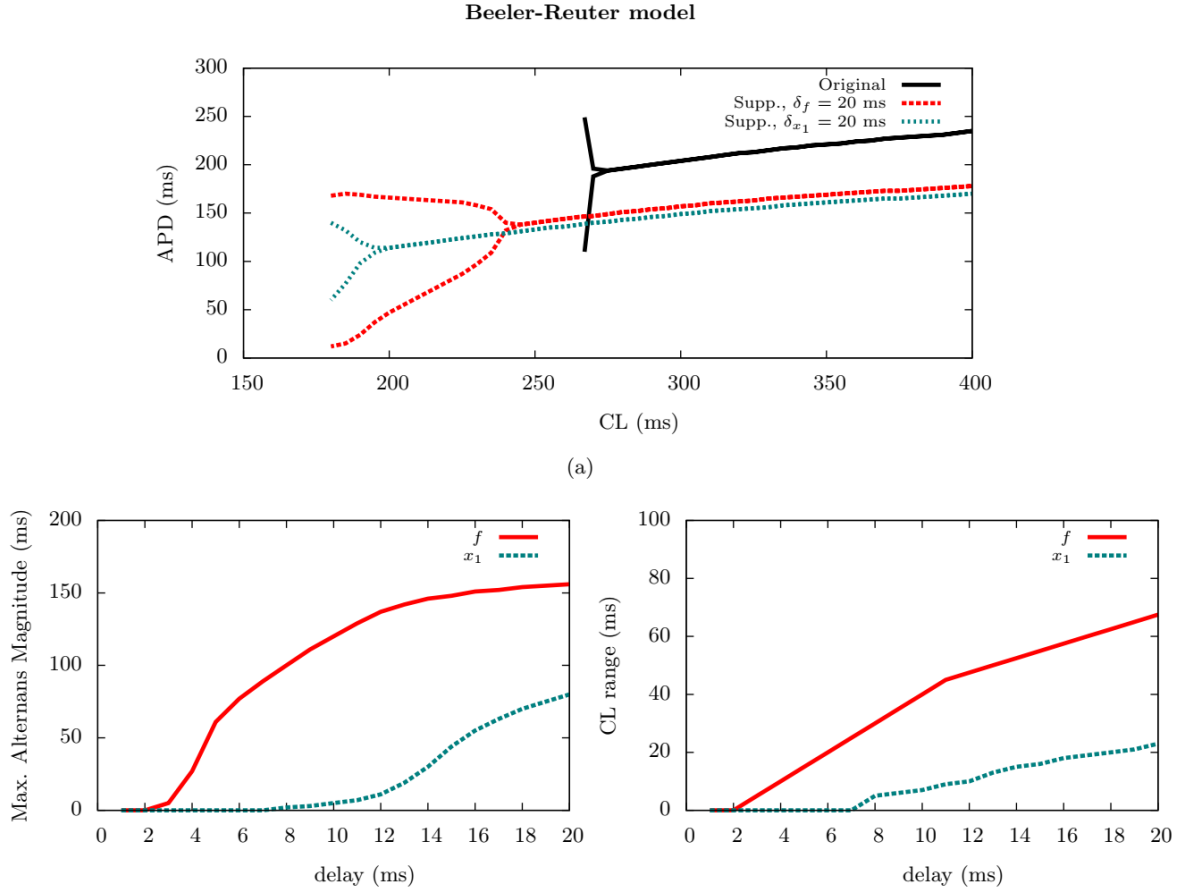


Figure 4.9: (a) Bifurcation plots for the Beeler-Reuter model using DDEs for the gating variables f and x_1 . (b) Maximum alternans magnitude as a function of delay. (c) Alternans CL range as a function of delay.

produced. If the sodium gates m , h , and j are simultaneously delayed as a group, then the AP amplitude is preserved and no alternans is observed, but for $\delta \geq 5$ ms the AP shape presented superposed oscillations. Alternans could not be induced when the sodium inactivation gates were delayed separately either.

The Luo - Rudy (1991) model in its original description exhibits relatively large APDs, so it is not possible to pace the model fast enough in order to observe alternans. Therefore, we increased the maximum conductivity (\bar{g}_K) of the time-dependent potassium current (I_K) from $0.282\text{mS}/\text{cm}^2$ to $0.705\text{mS}/\text{cm}^2$ to reduce the APD and enable faster pacing to be applied. In this modified version of the model (mLR1), alternans occurs for CLs smaller than 240 ms. Alternans can be suppressed if the maximum conductivity (\bar{g}_s) of the slow inward current (I_S) is decreased. Alternans in the mLR1 model was suppressed for any tested pacing period by reducing \bar{g}_s by a factor of 0.8.

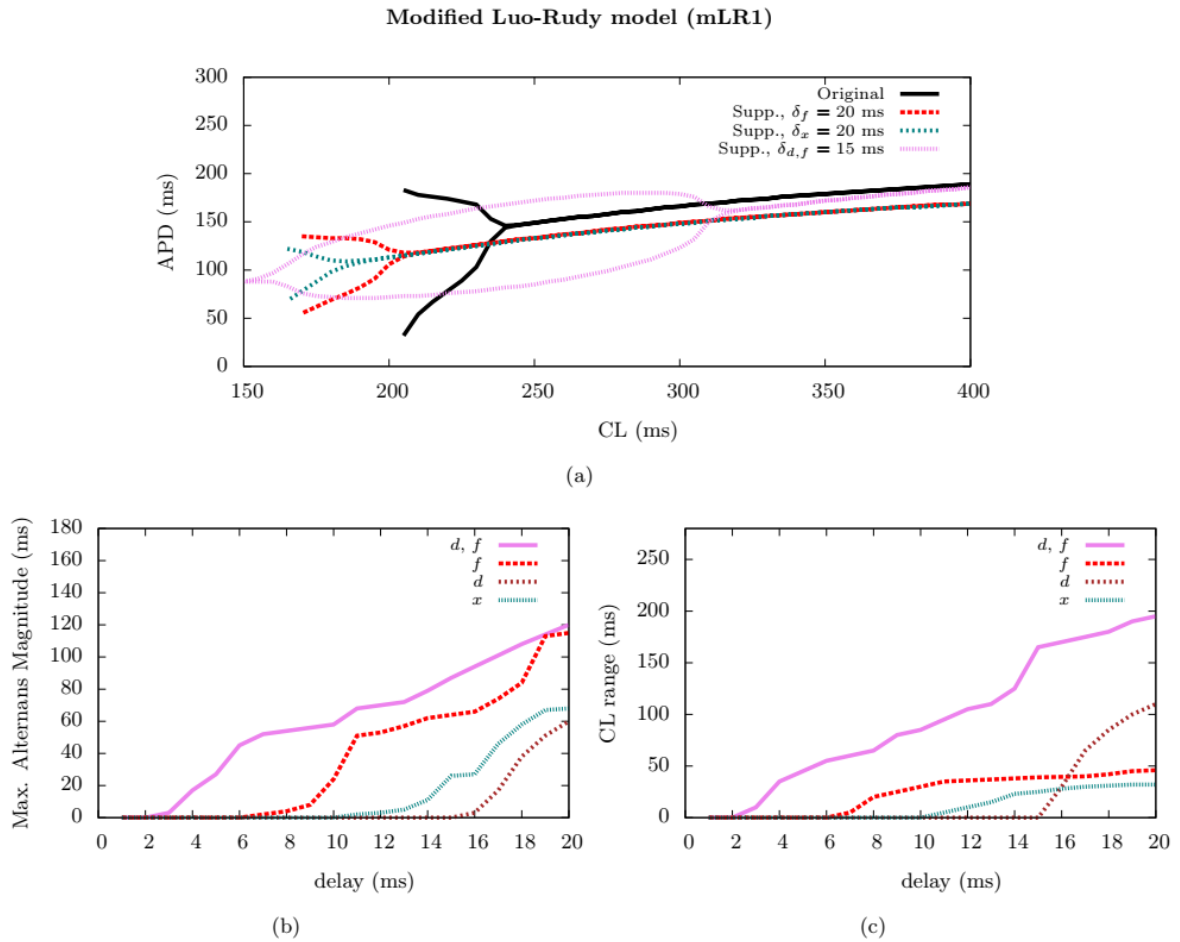


Figure 4.10: (a) Bifurcation plots of the alternans-suppressed mLR1 model with DDE formulations for the gating variable f , gating variable x , and gating variables f and d together. (b) Maximum alternans magnitude as a function of delay. (c) Alternans CL range as a function of delay.

By delaying different gating variables, it was possible to restore alternans in the alternans-suppressed version in few scenarios. Figure 4.10a shows bifurcation plots from versions with DDE implementation for the I_s inactivation gate f , the I_s activation gate d and f gate simultaneously, and the time-dependent potassium current activation gate x . The most pronounced alternans was achieved by delaying both the d and f gates, as shown in Fig. 4.10. The alternans magnitude and CL range are shown as functions of delay size in Figures 4.10b and 4.10c. As with the Noble and Beeler-Reuter models, the alternans magnitude and CL range are monotonically increased with delay size for all cases, showing that delays consistently enhanced alternans in this model for the considered range of delays. Cases where alternans could not be induced are detailed in our published

article (Gomes *et al.*, 2017).

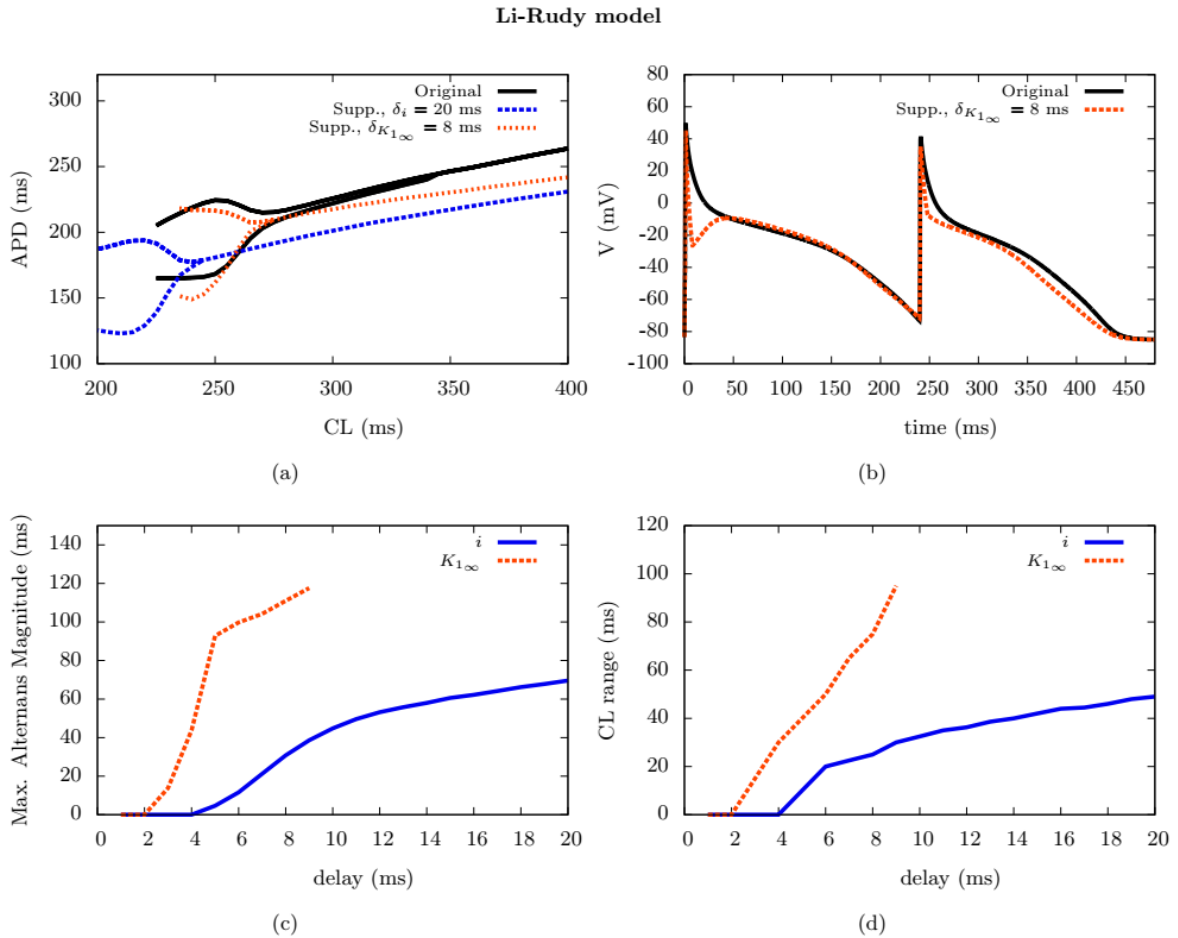


Figure 4.11: (a) Bifurcation plots of the alternans-suppressed Li-Rudy model with delayed gates i and $K_{1\infty}$. (b) APs from the original model and the alternans-suppressed version with delayed $K_{1\infty}$ ($CL = 245$ ms) using a delay of 8 ms, which produced AP shapes very close to those of the original model. (c) Maximum alternans magnitude as a function of delay. (d) Alternans CL range as a function of delay. Action potential blocks occur when delaying $K_{1\infty}$ by values greater than 9 ms.

The Li - Rudy (2011) model exhibits alternans for pacing periods lower than 340 ms, as shown in Fig. 4.11a. We suppressed alternans by increasing the maximum conductivity of the delayed rectifier potassium current (I_{K_r}) by a factor of 2, which produced only minor alterations on the AP shape and duration. When applying DDE formulations, the only time-dependent gating variable that produced alternans was the inactivation gate i of the transient outward potassium current I_{to} . Delaying the remaining gates either did not induce alternans or, in the case of delaying the sodium current gates, produced unphysiological action potential shapes for delay values greater than 2 ms. Alternans

could also be produced by delaying V in the algebraic formulation of the quasi-gate $K_{1\infty}$ of the inward-rectifier potassium current I_{K_1} . Figure 4.11a shows the bifurcation plots for these two successful cases, and Figures 4.11c and 4.11d present the corresponding alternans magnitude and CL range as a function of delay, respectively. In both scenarios, both the maximum alternans magnitude and the CL range of alternans increased with the use of longer delays.

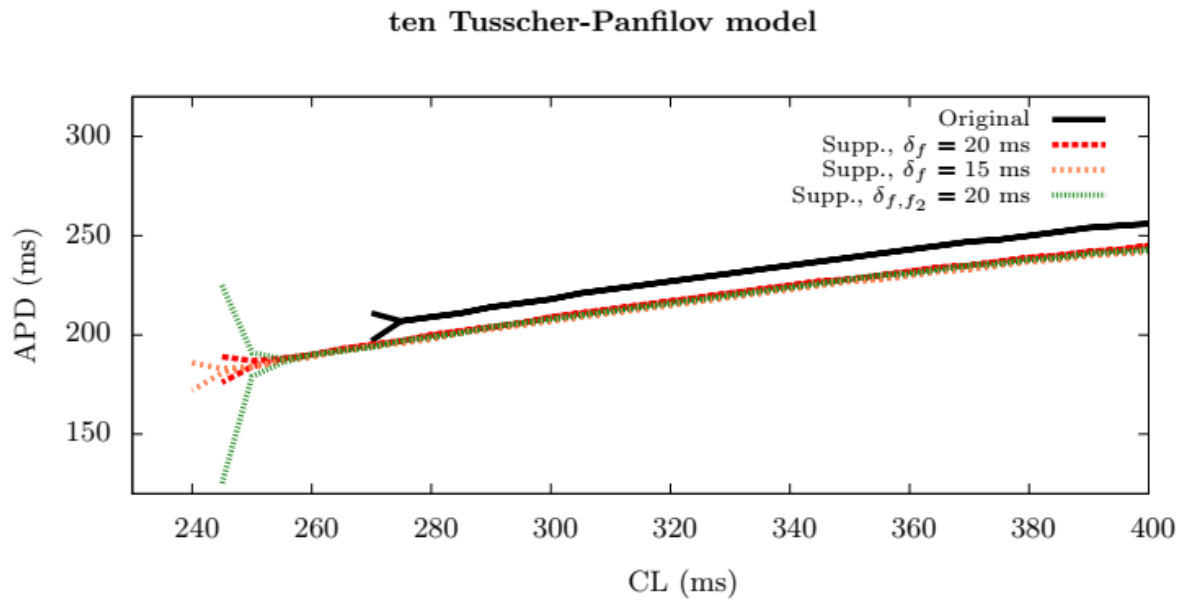


Figure 4.12: Bifurcation plots of the alternans-suppressed Tusscher - Panfilov (2006) model by using DDE formulations for f and for both f and f_2 .

The Tusscher - Panfilov (2006) model produces alternans when paced with cycle lengths lower than 275 ms. In this work, we increased the delayed rectifier potassium current I_{K_r} conductance by a factor of 1.9 in order to inhibit alternans, producing an alternans-suppressed version of the model with a minor impact on the AP shape. Figure 4.12 shows bifurcation plots from scenarios where alternans could be restored with the use of delays. Alternans were successfully produced when DDEs were applied to the I_{Ca_L} inactivation gate f or to both I_{Ca_L} gates f and f_2 . The point of bifurcation becomes closer to the original model as the delay value is increased (see Fig. 4.12).

As with the other models, delaying sodium gates produced unphysiological upstrokes in the AP. They appear when delaying the activation gate m with $\delta \geq 3$ ms. Delaying

the inactivation gates h and j did not result in alternans, as observed for the other four models. When all three gates are delayed as a group, extra upstrokes occur before the repolarization phase for $\delta \geq 5$ ms and no alternans is produced. Using a DDE formulation for the activation gate x_s (slow delayed rectifier potassium current I_{K_s}), activation gate x_{r_1} (rapid delayed rectifier potassium current I_{K_r}), or inactivation gate s (transient outward potassium current I_{to}) did not result in alternans. In addition, alternans can be produced when DDEs are used for both the calcium inactivation gates f and f_2 , but not when only f_2 is delayed.

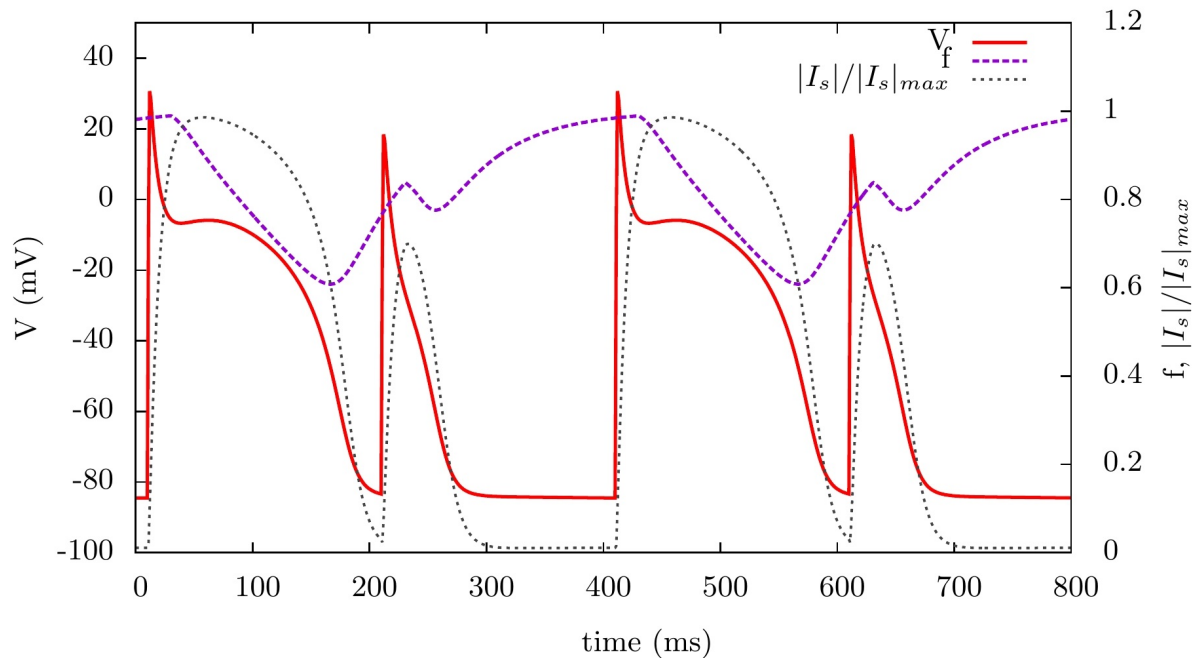


Figure 4.13: Membrane potential, calcium inactivation gating variable f and calcium current during alternans in the suppressed Beeler-Reuter model with DDE for f , using $\delta = 20$ ms and $CL = 200$ ms.

In every case where alternans could be restored, the gating variable modified with the DDE formulation had a significant influence on the action potential duration and its recovery was significantly impaired by the delay. As an example, Fig.4.13 shows how the calcium current inactivation gate f has its recovery affected by the imposition of a 20 ms delay, which leads to the long-short alternation in the resulting action potentials of the Beeler - Reuter (1977) model, since its associated current (I_S), like most inward calcium currents, plays a significant role in modulating the length of the plateau phase

and, consequently, the APD.

We concluded from the results that there are two possible requirements for a gating variable to induce alternans when modified with the DDE formulation: (i) the associated ion current must have significant influence on the APD and (ii) the delay must significantly impair the recovery of the gate between two consecutive APs. The establishment of these two requirements suggests a general approach when promoting alternans through DDEs in a Hodgkin-Huxley-based model of cardiac AP. All results presented in this section were published and described with more details in Gomes *et al.* (2017).

4.1.2 DDE-induced alternans in cardiac myocyte models

A number of models for cardiac myocytes are not originally capable of reproducing alternans in single cell simulations, even when fast paced stimuli are applied. In this section, we present and discuss results obtained from DDE-based modifications in two of these models.

4.1.2.1 ten Tusscher *et al.* model (2004)

The model of the action potential of human ventricular cells proposed by ten Tusscher *et al.* (2004) has been widely used to simulate reentrant arrhythmias in human ventricular tissue. It includes parameter configurations for endocardial, epicardial, and midmyocardial cells and it has a basic description of intracellular calcium dynamics.

The original model settings do not exhibit steady state APD alternans in single cell simulations, as shown in the CL versus APD curve of Figure 4.14A. For all three parameter settings, it can be observed that if the imposed CL is decreased below certain value, the APD starts increasing up to a point where action potential blocks occur, as shown in Figure 4.14B.

We analyzed the sensitivity of the APD with respect to the model's ion current maximum conductances to determine which gating variables would be more prone to induce alternans if delayed. In Figure 4.15 we show how the APD responds to changes in maximum conductances of ion currents of the model. It can be observed that increasing

ten Tusscher et al. (2004) model: original settings

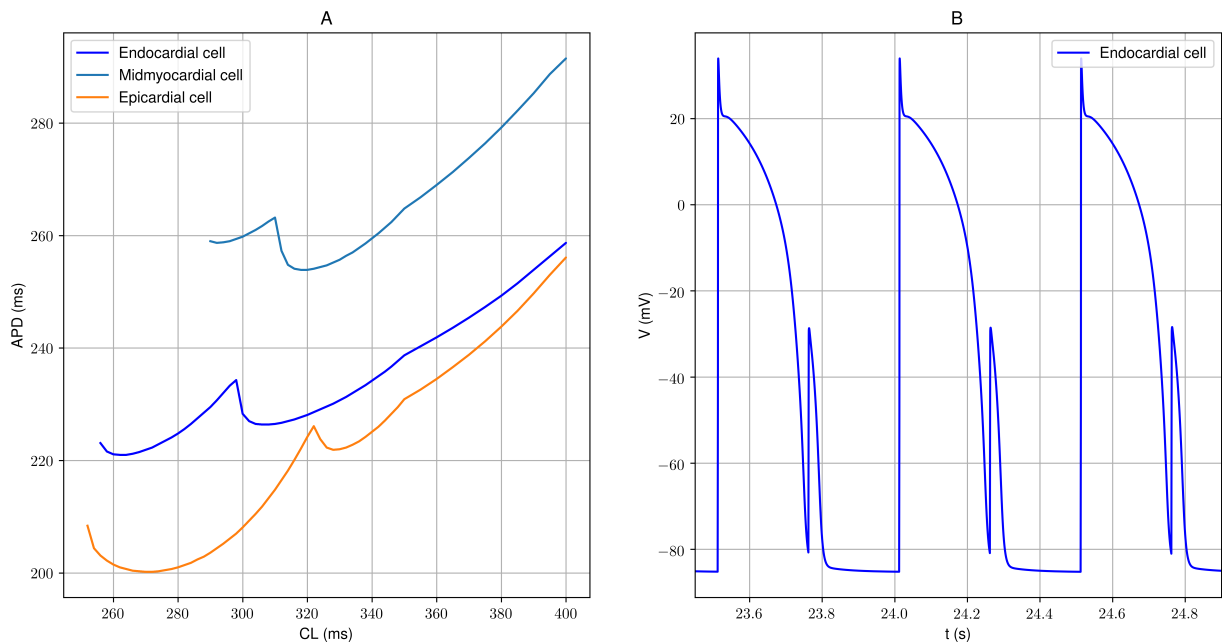


Figure 4.14: (A) CL versus APD curves for the three original parameter settings of the ten Tusscher *et al.* (2004) model. (B) Action potential blocks that occur in the endocardial setting of the ten Tusscher *et al.* (2004) model for CL = 250 ms.

ten Tusscher et al. (2004) model: conductivities modifications

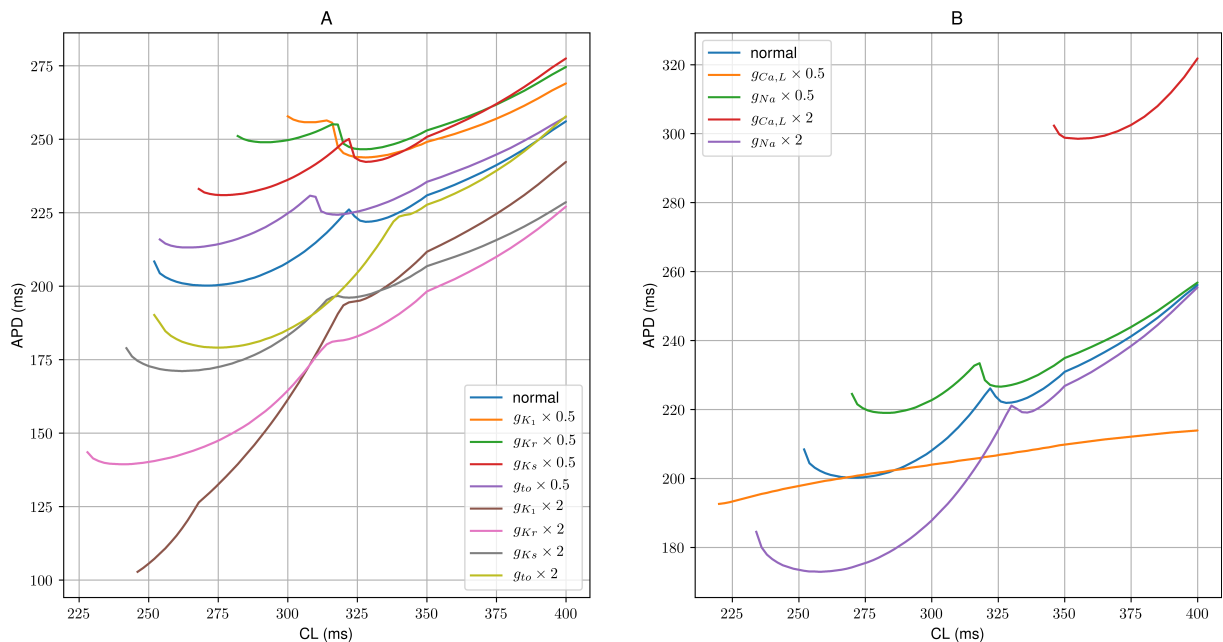


Figure 4.15: CL versus APD curves for assessing the APD sensitivity to ion current maximum conductivities. Each curve results from a single modification in the epicardial cell model by ten Tusscher *et al.* (2004): (A) Modifications to potassium maximum conductivities; (B) modifications to sodium and calcium maximum conductivities.

potassium conductances leads to lower values of APD, and the opposite effect can be obtained by decreasing the potassium conductances. This behavior is expected since potassium currents are generally responsible for promoting the repolarization phase. On the other hand, calcium currents tend to postpone the repolarization phase, which contributes to increasing the APD as can be evidenced when modifying $g_{Ca,L}$. Increasing the sodium conductance leads to stronger upstroke, which could potentially delay repolarization, but the opposite behavior can be observed in 4.15B because repolarizing currents are increased in response to the higher depolarization peak. The potassium currents I_{K_1} , I_{K_r} , I_{to} , and I_{K_s} all have a noticeable influence on the APD, and that is also true for the L-type calcium current $I_{Ca,L}$, as doubling the original value of $g_{Ca,L}$ promotes a strong increase in the APD. Modifications in the sodium current conductance do not produce great APD changes in terms of magnitude.

We tested applying the DDE formulation described in Section 3.2 to the following gating variables: the sodium current (I_{Na}) activation gate m and inactivation gates j and h ; the L-type calcium current (I_{Ca}) activation gate d , voltage-dependent inactivation gate f , and intracellular calcium-dependent inactivation gate f_{Ca} ; the inward rectifier potassium current (I_{K_1}) time-dependent activation gate $K_{1\infty}$; the rapid delayed rectifier current (I_{K_r}) activation gate x_{r1} and inactivation gate x_{r2} ; the slow delayed rectifier current (I_{K_s}) activation gate x_s ; and the transient outward current I_{to} activation gate r and inactivation gate s .

Delays from 2 ms to 20 ms were applied to each calcium and potassium gate separately. None of these DDE-based modifications could promote steady-state APD alternans before action potential blocks started to occur. We applied small delay values from 0.5 ms to 2 ms to each sodium gating variable, since applying greater delay values produced degenerated or unphysiological action potentials. This also resulted in action potential blocks at fast pacing rates and no alternans. The next step was to apply the DDE formulation simultaneously to groups of gating variables, where each group consisted of all gating variables of given ion current. Figure 4.16A shows APD x CL diagrams resulting from some of these experiments, showing it is possible to induce moderate alternans in

ten Tusscher et al. (2004) model: delaying groups of gates

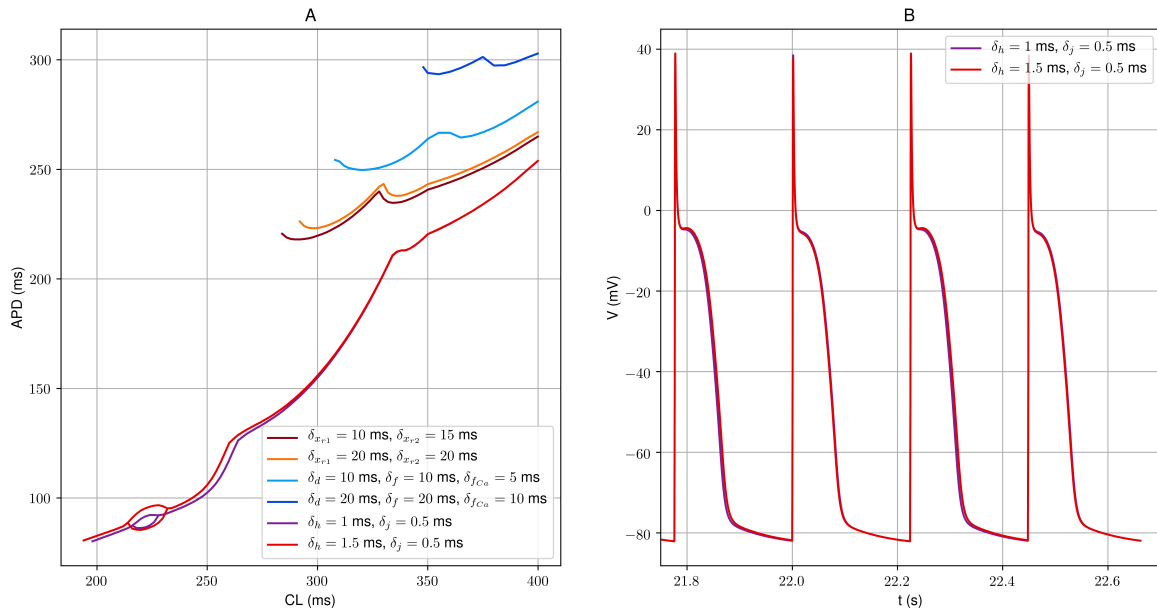


Figure 4.16: Delaying groups of gating variables in the ten Tusscher *et al.* (2004) model: (A) APD x CL diagrams of scenarios with DDEs applied to gates of the I_{K_r} current (x_{r1} and x_{r2}), the $I_{Ca,L}$ current (d , f , and f_{Ca}), and the I_{Na} current (m , h , and j); (B) action potentials exhibiting moderate steady-state alternans when sodium inactivation gates are delayed (CL = 224 ms).

this model by applying certain combinations of delay values to the sodium inactivation gates h and j (Fig. 4.16B). Alternans could not be induced by delaying groups of calcium or potassium gates separately by values from 2 ms to 20 ms.

In order to enhance the observed DDE-induced alternans of Fig.4.16B, we tested combining the use of DDEs to sodium inactivation gates with delaying other groups of gating variables. Simulations were performed in three different scenarios, each of them varying δ_h and δ_j from 0 to 2 ms in steps of 0.5 ms: (i) delaying $\delta_{x_{r1}}$ and $\delta_{x_{r2}}$ by up to 20 ms; (ii) delaying d , f , and f_{Ca} by up to 20 ms; and (iii) delaying r and s by up to 20 ms. Figure 4.17 shows that some of these modifications produced strong steady-state alternans at the expense of affecting the morphology of restitution curves.

Understanding the underlying mechanism of alternans in these experiments can be a complex challenge, since it involves the use of DDEs in multiple ion channel formulations using delay sizes of different orders of magnitude. As shown in Figure 4.16, delaying sodium inactivation gates destabilizes the APD to a certain degree, and adding delays to gating variables associated with repolarization currents seems to amplify these instabilities

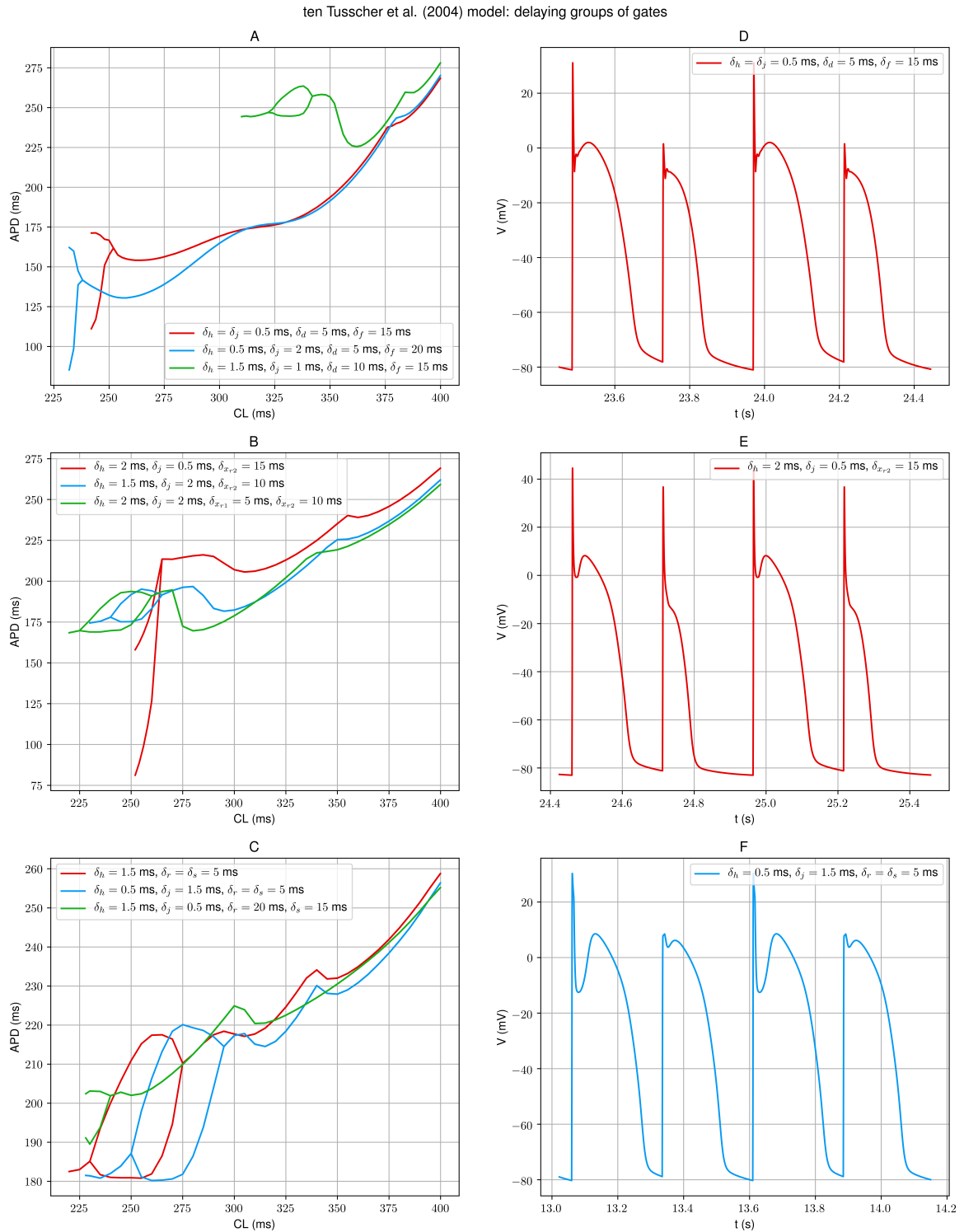


Figure 4.17: Bifurcation diagrams from experiments associating delayed sodium inactivation gates with the use of delays for $I_{Ca,L}$ gates (A), I_{Kr} gates (B), and I_{to} gates (C) in the ten Tusscher *et al.* (2004) model. Action potentials from selected cases exhibiting steady-state alternans using stimulus periods of 242 ms (D), 252 ms (E), and 275 ms (F).

and produce strong steady-state alternans (Fig. 4.17). In addition, it is possible to observe how delaying sodium inactivation gates can produce a favorable condition for other

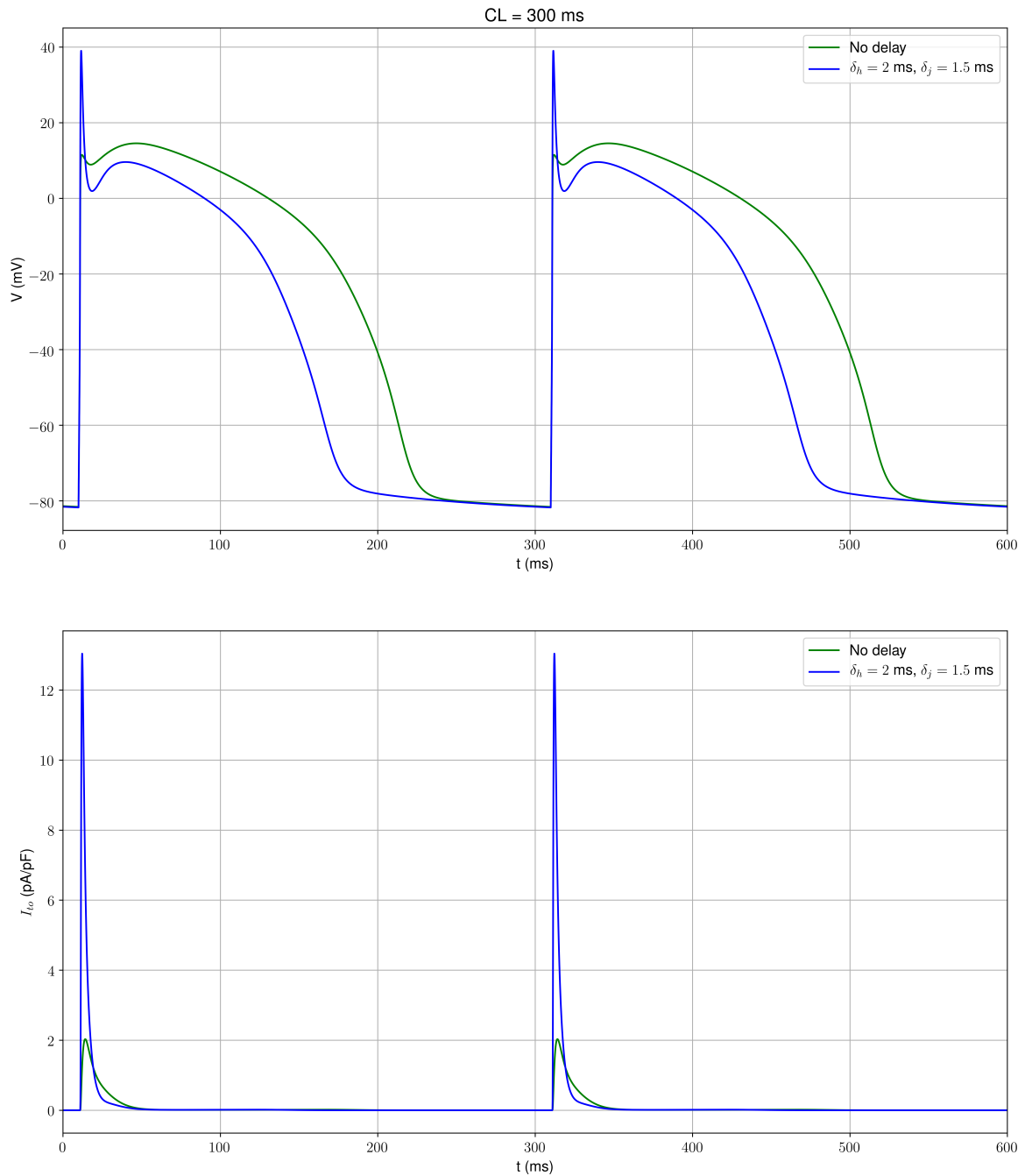


Figure 4.18: Original ten Tusscher *et al.* (2004) model for epicardial cells versus version with delayed sodium inactivation gates.

gating variables to induce alternans when delayed, as this kind of DDE-based modification strengthens the upstroke and reduces the action potential duration (Fig. 4.18A), which allows the use of lower CLs before action potential blocks start to occur. The APD is reduced because some outward currents are increased in response to the stronger upstroke, as shown in Figure 4.18B where the I_{to} current is more than six times greater than that of the version with no DDEs.

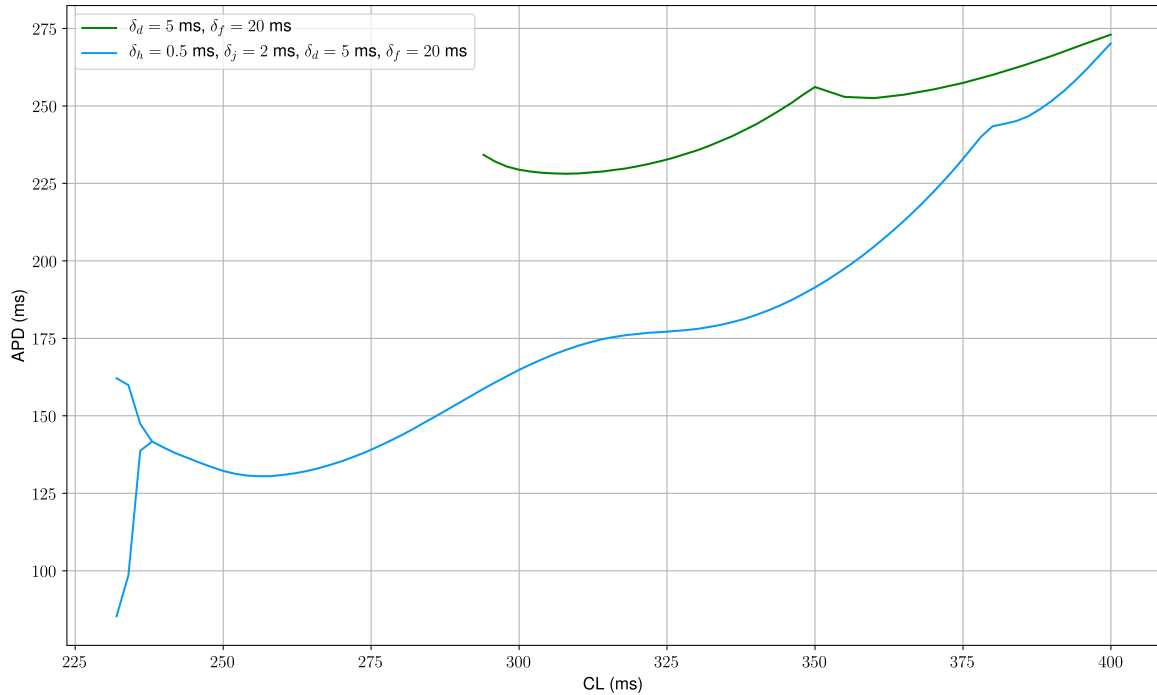


Figure 4.19: Bifurcation diagrams from DDE-based experiments with the ten Tusscher *et al.* (2004) model: version with delayed calcium gates d and f versus version with DDE implementation for sodium gates h and j and calcium gates d and f .

To illustrate how these features facilitate the initiation of alternans, let us consider one of the cases of Fig. 4.17 where both sodium gates and calcium gates are delayed with $\delta_h = 0.5 \text{ ms}$, $\delta_j = 2 \text{ ms}$, $\delta_d = 5 \text{ ms}$ and $\delta_f = 20 \text{ ms}$. Figure 4.19 shows that if only calcium gates are delayed, it is not possible to apply stimulus periods lower than 294 ms, but if the sodium inactivation gates are also delayed, it is possible to use CLs as low as 232 ms, and steady-state alternans starts to occur at $CL = 236 \text{ ms}$. From that point, alternans is sustained by a mechanism similar to that of the Beeler - Reuter (1977) model with delayed calcium inactivation gate (Fig. 4.13), i.e. an incomplete recover of the calcium gates that shortens the AP followed by a complete recover of the calcium gates that increases the AP and causes the cycle to repeat.

4.1.2.2 Grandi *et al.* model (2010)

The mathematical model for the human ventricular action potential proposed by Grandi *et al.* (2010) describes the intracellular calcium handling and how it relates to the excitation-contraction coupling mechanism. The model also aims to describe adaptation

Grandi et al. (2010) model: original settings

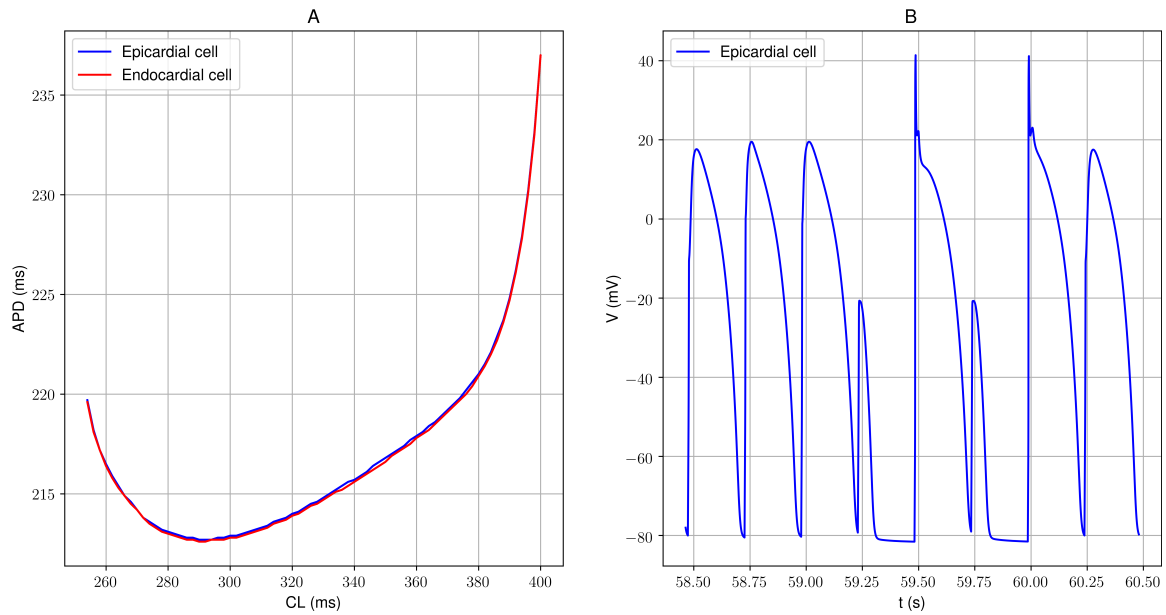


Figure 4.20: (A) CL versus APD curves for both original settings of the Grandi *et al.* (2010) model. (B) Action potential blocks and chaos that occur in the original setting of the Grandi *et al.* (2010) model, despite constant pacing at $CL = 252$ ms and a small integration step of 10^{-4} ms.

mechanisms for APD shortening at fast pacing rates for both epicardial and endocardial cells. Experiments in the literature (Elshrif - Cherry, 2014) involving this model were not able to reproduce alternans. As shown in Figure 4.20A, the model in its original parameter configuration exhibits APD shortening as the CL decreases from 400 ms to 290 ms, but if the CL is decreased further the APD starts increasing up to a point where action potential blocks start to occur (Fig. 4.20B) and the model becomes highly sensitive to perturbations in the stimulus current, leading to a chaotic behavior despite constant pacing at $CL = 252$ ms.

As with the ten Tusscher *et al.* (2004) model, we investigated the APD sensitivity of the Grandi *et al.* (2010) model to ion currents to determine candidate gating variables for being delayed in order to promote alternans. For each maximum conductance of the model's membrane currents, we tested both reducing up to 50% and increasing up to double its value and measured the resulting changes in APD. Figure 4.21 shows the APD x CL diagrams from tests that resulted in more than 5 % change in the APD with respect to the original model. The APD is strongly sensitive to both the inward-rectifier

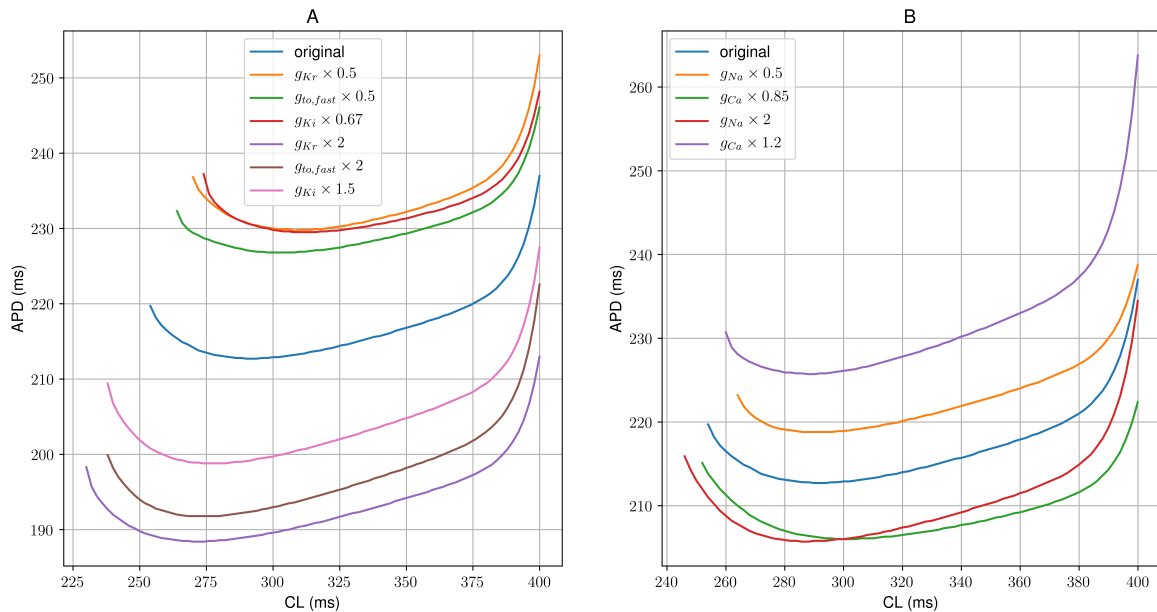
Grandi *et al.* (2010) model: conductivities modifications

Figure 4.21: CL versus APD curves for assessing the APD sensitivity to maximum ion current conductivities of the Grandi *et al.* (2010) model (epicardial cell version): (A) Modifications to potassium maximum conductivities; (B) modifications to sodium and calcium maximum conductivities.

potassium current (I_{K_1}) and the L-type calcium current ($I_{Ca,L}$), so that moderate changes in their maximum conductivities can lead to early action potential blocks.

The DDE implementation was applied to: the fast sodium current ($I_{Na,f}$) activation gate m and inactivation gates j and h ; the L-type calcium current ($I_{Ca,L}$) activation gate d and voltage-dependent inactivation gate f ; the inward rectifier potassium current (I_{K_1}) time-dependent activation gate $K_{1\infty}$; the rapid delayed rectifier current (I_{Kr}) activation gate x_{kr} ; and the fast transient outward current $I_{to,fast}$ activation gate $x_{to,f}$ and inactivation gate $y_{to,f}$.

The sodium-related gates were delayed by up to 2 ms as in previous experiments, whereas the other gating variables were delayed by values up to 20 ms. The preliminary experiments consisted of delaying each gating variable separately, and no alternans was observed in any of them. The next step was to delay all gating variables associated with each ion current simultaneously, which did not produce alternans either, despite changes in APD dynamics were observed, as shown in Figure 4.22.

Finally, we tested applying the DDE formulation simultaneously to the fast sodium

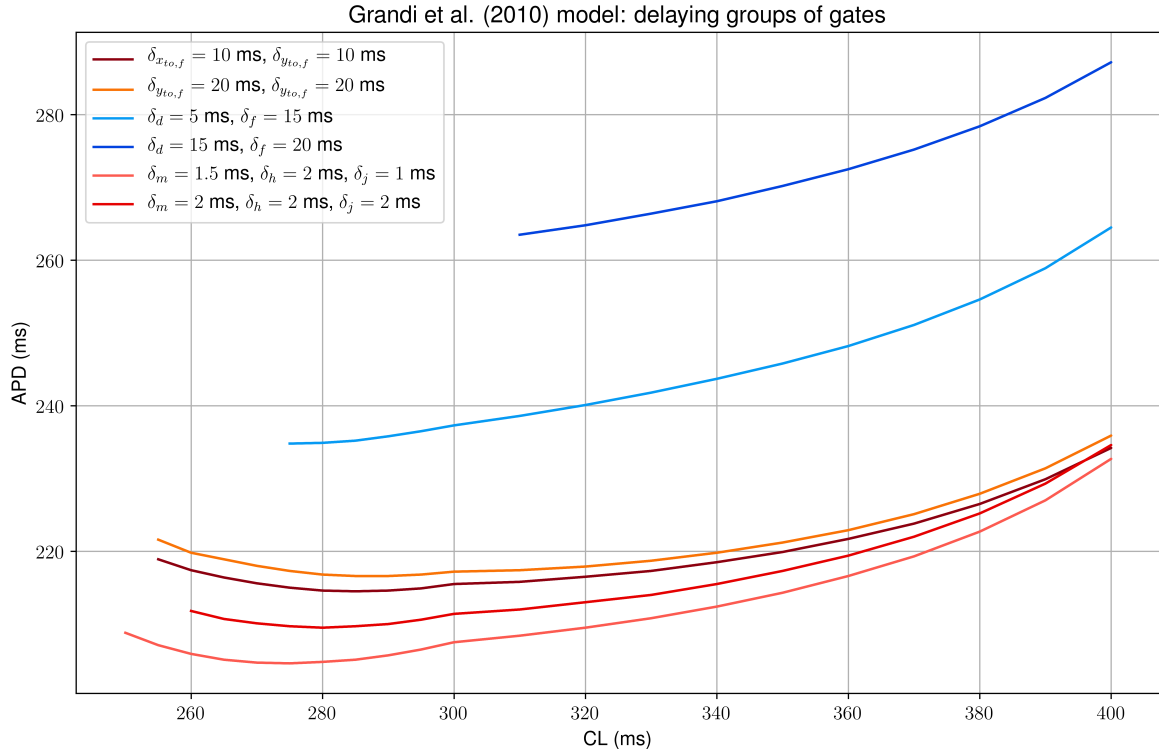


Figure 4.22: APD versus CL curves from experiments delaying groups of gating variables in the Grandi *et al.* (2010) model.

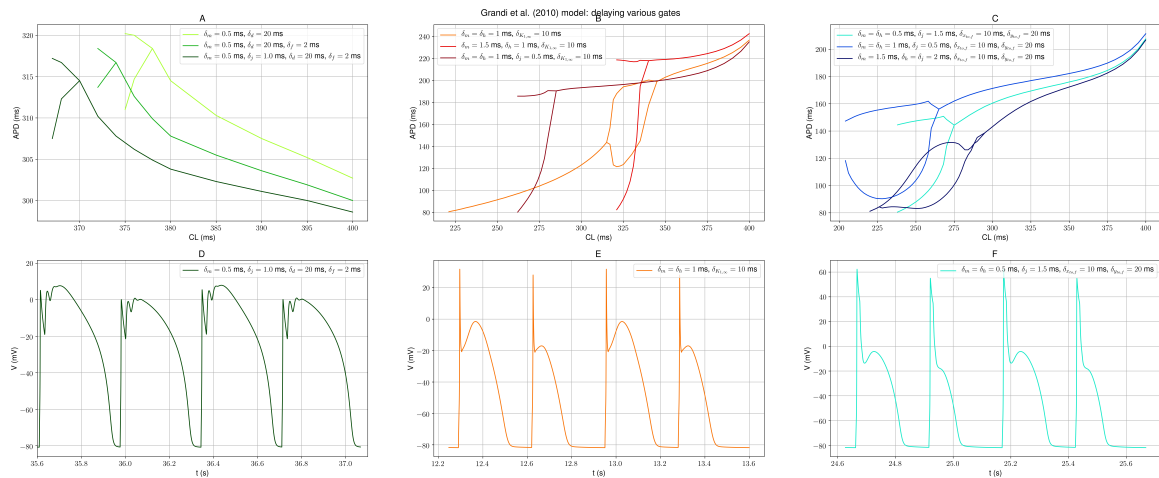


Figure 4.23: DDE-induced alternans from experiments delaying various combinations of gates in the Grandi *et al.* (2010) model. Bifurcation diagrams from experiments applying the DDE formulation to: (A) $I_{Na,f}$ and $I_{Ca,L}$ gates; (B) $I_{Na,f}$ gates and the I_{K_1} activation gate; and (C) $I_{Na,f}$ and $I_{to,f}$ gates. Action potentials from selected cases exhibiting steady-state alternans using stimulus periods of 367 ms (D), 330 ms (E), and 254 ms (F).

current gates and to groups of gating variables associated to other ion currents. The experiments were performed in four different scenarios, each of them varying δ_m , δ_h , and δ_j from 0 to 2 ms in steps of 0.5 ms: (i) delaying d and f by up to 20 ms; (ii) delaying $K_{1\infty}$ by up to 20 ms; (iii) delaying x_{kr} by up to 20 ms; and (iv) delaying $x_{to,f}$ and $y_{to,f}$ by

up to 20 ms. Alternans was successfully induced in some instances of scenarios (i), (ii), and (iv), as shown in Figure 4.23.

4.2 DDE-based simulations of cardiac tissue

4.2.1 History management algorithms in ring simulations

In order to assess the efficiency and accuracy of the adaptive algorithms described in Section 3.5, we performed 1D simulations of the Fox *et al.* model with doubled g_{Kr} in a ring geometry so that both conduction velocity and gating variable accuracy could be measured with respect to a reference solution, using the DDE formulation described in Sec. 3.2. The performance of the algorithm only depends on how fast the delayed variables change, so the results should provide useful insight into more general applications of DDEs to cardiac models.

The length of the ring was 12 cm and the spatial discretization was $\Delta x = 0.02$ cm. A single stimulus pulse was applied at the beginning of the simulation and the wave propagated periodically with a period of approximately 200 ms for all tested DDE implementations. The reference solutions were obtained by updating local history information at all spatial locations every time step.

Table 4.1 shows the results in terms of memory use for different scenarios of DDE-based implementations. Each case consists of applying Equation (3.8) to one or more voltage-dependent gating variables, so that only voltage is stored in history, even if more than one gate is delayed. The memory use is presented through the number of values per history node (VPHN). For the SLIA, the VPHN is fixed and given by the ratio of the delay size to the history time step Δt_{hist} . Since the history size changes dynamically when the AHMA is applied, both the average and maximum VPHN are shown for each case in the table. The average memory usage of the AHMA is always significantly lower than that of the SLIA, while the maximum memory usage - which occurs only during specific short periods - is higher in a few scenarios.

The parameters were chosen to provide minimum history length and numerical errors

Table 4.1: Number of values per node history (NVPNH) in simulations of a 12 cm ring using the Fox *et al.* model with delays used for different gating variables. Gating variable choices included the L-type calcium current activation gate d , the L-type calcium current voltage-dependent inactivation gate f , the combination of d and f , and the three gates of the sodium current with the same delay. The parameters Δt_{hist} , ϕ_{push} and ϕ_{lin} were chosen based on achieving a 2% tolerance for the gating variable and conduction velocity errors with respect to the reference solution. The highlighted numbers indicate the most memory-efficient results of each scenario in terms of maximum NVPNH, although the AHMA always exhibits the lowest average memory use.

DDE formulation	Reference	SLIA		AHMA				
	NVPNH	Δt_{hist}	NVPNH	ϕ_{push}	$\phi_{lin,u}$	$\phi_{lin,d}$	avg. NVPNH	max. NVPNH
$\delta_d = 5$ ms	250	0.1 ms	50	0.5 mV	0.125 mV	0.25 mV	6.01	66
$\delta_d = 10$ ms	500	0.1 ms	100	0.5 mV	0.125 mV	0.125 mV	9.19	74
$\delta_d = 20$ ms	1000	0.1 ms	200	0.5 mV	0.125 mV	0.125 mV	14.9	76
$\delta_d = 30$ ms	1500	0.1 ms	300	1.5 mV	0.15 mV	0.15 mV	21.2	68
$\delta_f = 5$ ms	250	0.5 ms	10	1.5 mV	0.375 mV	0.75 mV	5.41	26
$\delta_f = 10$ ms	500	0.5 ms	20	1 mV	0.25 mV	0.5 mV	7.28	30
$\delta_f = 20$ ms	1000	0.5 ms	40	2 mV	0.5 mV	0.5 mV	11.4	38
$\delta_f = 30$ ms	1500	0.5 ms	60	1 mV	0.25 mV	0.25 mV	15.9	54
$\delta_d = \delta_f = 5$ ms	250	0.2 ms	25	1 mV	0.25 mV	0.25 mV	5.95	50
$\delta_d = \delta_f = 10$ ms	500	0.2 ms	50	1 mV	0.25 mV	0.25 mV	7.78	54
$\delta_d = 12$ ms, $\delta_f = 20$ ms	1000	0.2 ms	100	1 mV	0.25 mV	0.25 mV	11.9	52
$\delta_d = \delta_f = 20$ ms	1000	0.2 ms	100	1 mV	0.25 mV	0.25 mV	12.2	52
$\delta_d = \delta_f = 30$ ms	1500	0.2 ms	150	1 mV	0.25 mV	0.25 mV	15.3	52
$\delta_m = \delta_h = \delta_j = 0.5$ ms	25	0.04 ms	13	1.5 mV	0.375 mV	0.75 mV	4.03	10
$\delta_m = \delta_h = \delta_j = 1$ ms	50	0.04 ms	25	0.5 mV	0.125 mV	0.125 mV	4.14	20

below 2% for the gating variables and the conduction velocity with respect to the reference solution. For determining each parameters configuration, we tried to set the highest possible value to ϕ_{push} first while maintaining the other two parameters set to zero, since ϕ_{push} directly limits the maximum history size to $ceil[(V_{max} - V_{min})/\phi_{push}]$, where V_{max} and V_{min} are the maximum and the minimum computed voltage values, respectively. Once we determined ϕ_{push} , we set $\phi_{lin,u}$ and $\phi_{lin,d}$ to a quarter of the ϕ_{push} value and then progressively increased both values until the error tolerance was reached. Finally, since numerical errors are usually more sensitive to $\phi_{lin,u}$ than to $\phi_{lin,d}$, we tested whether doubling only $\phi_{lin,d}$ would reduce the average history size while maintaining the numerical error below the 2% tolerance.

The results indicate that tolerances must be chosen based on how the gating variable is sensitive to the upstroke and to the repolarization phase. Activation gates, like the d gate, are usually sensitive to the depolarization phase, so the corresponding ϕ_{push} and $\phi_{lin,u}$ needed to obtain good accuracy tend to be small. On the other hand, repolarization-sensitive gates allow for greater ϕ_{push} and $\phi_{lin,u}$, while tending to require a lower $\phi_{lin,d}$

value to meet accuracy requirements.

The average NVPNH for the AHMA is always significantly lower than the history size required by the SLIA, because the repolarization phase is much longer than the upstroke, which is the phase where the history is updated more often. In most cases, the AHMA outperforms the SLIA in terms of maximum history length, especially for large delays or cases where sodium gates are delayed, since it performs better in terms of conduction velocity accuracy. The exception are the cases where $\delta_f = 5$ ms or $\delta_d \leq 10$ ms.

4.2.2 *Spiral wave dynamics in 2D*

The proposed techniques now allow memory-efficient DDE-based tissue simulations and this is the first application of the DDE formulation presented in Section 3.2 to wave propagation experiments in 2D.

As presented in the previous section, these DDEs are capable of promoting instabilities and alternans in single-cell simulations of cardiac models based on the Hodgkin-Huxley formalism for ion channels. Therefore, it is natural to consider the effects of these DDE-based modifications on spiral wave dynamics in 2D, including stability, dominant frequency, and period distribution. In addition, these studies provide an opportunity to analyze the performance of the AHMA in a large domain for a range of conditions.

We performed 2D simulations of the Fox *et al.* in a 30 cm \times 30 cm tissue uniformly discretized into an 1500 \times 1500 grid. The experiments consist of the simulation of 10 seconds of electrical activity, using a single stable spiral wave obtained from 30 seconds of simulation of the alternans-suppressed version of the model ($g_{Kr} \times 2$) as initial condition.

Four cases were considered: (A) the original Fox *et al.* model; (B) the alternans-suppressed version of the model, obtained by doubling g_{Kr} ; (C) the alternans-suppressed version with a DDE implementation for the f gate using $\delta_f = 20$ ms; and (D) the alternans-suppressed version with a DDE implementation for both the f and d gates, using $\delta_f = 20$ ms and $\delta_d = 12$ ms. Figure 4.24 shows voltage snapshots of all four cases at different instants of time. In single cell experiments, it is possible to restore alternans by either delaying the f gate, or the d gate, or both (Eastman *et al.*, 2016). At the tissue

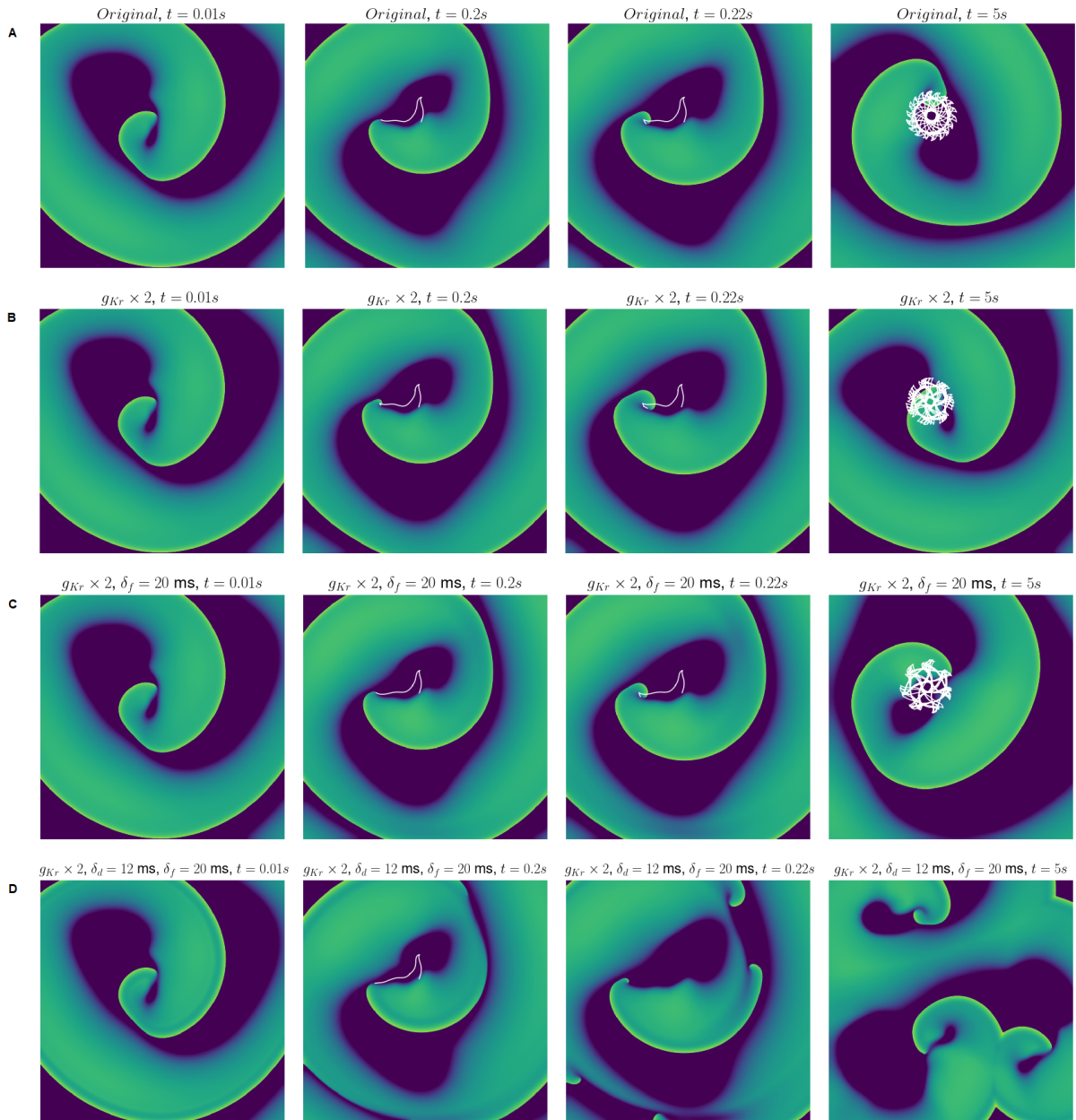
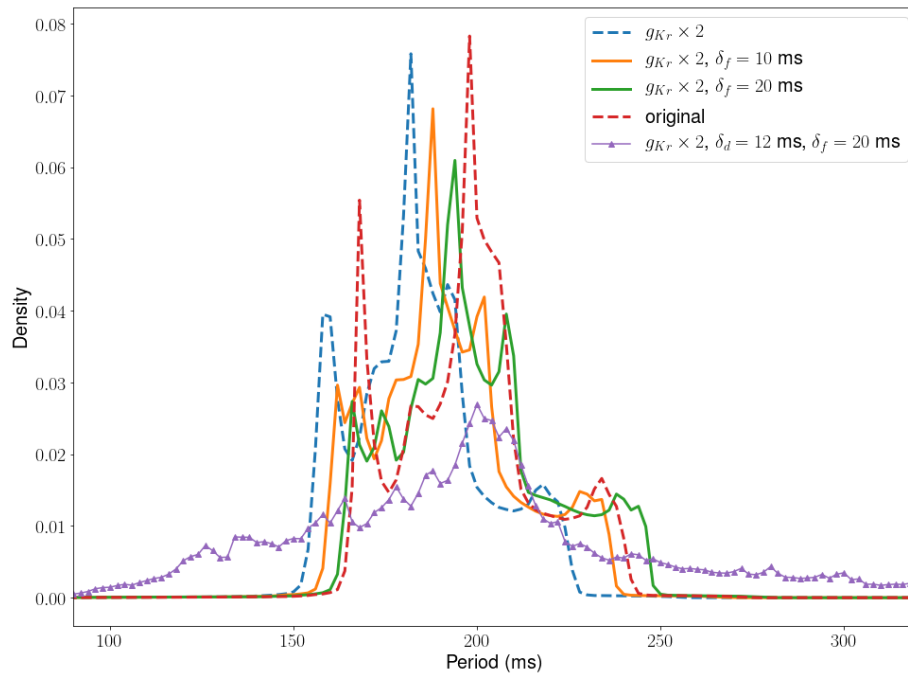


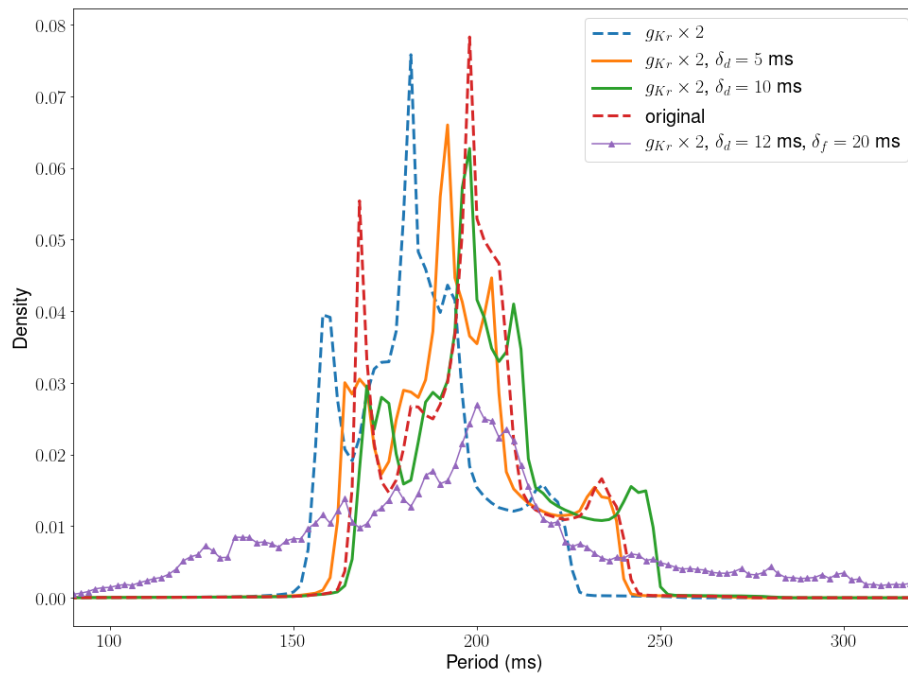
Figure 4.24: Snapshots of membrane potentials from simulations of a $30 \text{ cm} \times 30 \text{ cm}$ tissue using of the Fox *et al.* model and a stable spiral wave as initial condition, in four different scenarios: (A) the original model; (B) the model with doubled g_{Kr} ; (C) the model with doubled g_{Kr} and the f gate delayed by 20 ms; and (D) the model with doubled g_{Kr} , the f gate delayed by 20 ms, and the d gate delayed by 12 ms. The spiral wave tip trajectory is shown in white whenever there is a single spiral wave.

level, spiral breakups occurred only by delaying both voltage-dependent calcium gates in case D, where the single spiral wave started to break at $t = 0.2 \text{ s}$, and multiple spiral waves were generated, leading to a sustained chaotic behavior.

We also performed experiments to analyze how the dynamics changed as the delay sizes were increased. For that purpose, we simulated 20 seconds of electrical activity, starting



(a)



(b)

Figure 4.25: Period distributions across a 2D tissue for different configurations of the Fox *et al.* model: (a) DDE implementation for the f gate versus non-DDE versions and case D; (b) DDE implementation for the d gate versus non-DDE versions and case D.

from the same initial condition as before but applying different delay values to each voltage-dependent calcium gate. We measured the period distribution across the tissue during the last 10 seconds of each simulation. Figure 4.25 shows the period distributions

obtained for different values of the delay δ compared to the original model, the alternans-suppressed version of the model, and the version that produces spiral breakups (case D). As expected, the version with doubled \bar{g}_{Kr} and no DDE had its period profile displaced to the left with respect to that of the original model, since increasing \bar{g}_{Kr} reduced the action potential duration (APD) and thus the wavelength. As delays were added to the calcium gates of the alternans-suppressed model, the period distribution shifted to the right (longer periods), and the dominant frequency moved closer to that of the original model. We also observed that as the delay sizes were increased, the period spectrum became broader even in scenarios with no spiral wave breakups, which suggests that delays may have intensified the hypermeandering of the spiral wave.

4.2.3 Computational performance in 2D

Table 4.2: Computation times and history memory usage of different memory management implementations for simulating 1 second of electrical activity of the Fox *et al.* model in a 2D tissue. The alternans-suppressed version with DDE implementation for the f and d gates was used in order to assess the algorithms in a situation of sustained chaos.

Implementation	Computation time (CPU)	Max. hist. memory	Computation time (GPU)
Reference	293 minutes	17.3 GB	
SLIA	273 minutes	1.73 GB	4.28 minutes
AHMA w/ LLI	334 minutes	667.0 MB	
AHMA w/ SCAI	277 minutes	880.1 MB	4.46 minutes
AHMA w/ SMPI	287 minutes	648.4 MB	
AHMA w/ DAI	291 minutes	648.4 MB	

To assess the computational performance of the adaptive algorithm in a situation of complex dynamics, we simulated 1 second of electrical activity with configuration D, which resulted in spiral wave breakup, using OpenMP and the memory management implementations described in Section 3.5. Table 4.2 shows the computation time and history memory usage measured for all implementations of the adaptive algorithm. It also shows the results of a reference implementation that uses the standard first-order DDE solver. Double precision was used for real values and the code was compiled in x64 mode, which makes the size of each linked list pointer 4 bytes. The performance of all implementations is quite similar, with the linked list implementation (LLI) being the slowest one due to its more irregular memory operations. The memory usage is also

similar across all implementations and represents a 90% to 97% reduction with respect to the reference implementation and 50% to 63% compared to the SLIA.

The differences in terms of both memory and performance were not large across the various implementations of the AHMA: the fastest implementation (SCAI) was about 20% faster than the slowest (LLI), and the most memory-efficient implementations (SMPI and DAI) used 26% less memory than the least memory-efficient (SCAI). Therefore, ease of implementation could play a significant role in determining which memory-management scheme should be applied.

We also studied the performance of two of our history optimization algorithms on a graphics processing unit (GPU). The simple linear interpolation algorithm (SLIA) and the adaptive history management algorithm with contiguous arrays (AMHA+SCAI) were implemented in CUDA with the alternans-suppressed model and DDE implementations for the f and d gates ($\delta_f = 20$ ms, $\delta_d = 12$ ms). We limited our GPU implementations to these methods because the others involve irregular memory operations that dramatically impact the performance on the GPU and, for this reason, were not implemented.

Since $\delta_f = 20$ ms and $\delta_d = 12$ ms, $\Delta t_{hist} = 0.2$ ms was used for the SLIA implementation (Table 4.1). The tolerances for the AMHA+SCAI version were also chosen according to Table 4.1. The AMHA+SCAI implementation used about 50% less history memory than the SLIA implementation, but its performance (4.46 minutes) was 4% slower (4.28 minutes), as shown in Table 4.2. Both GPU implementations exhibited performance gains of about 63 times over the 16-thread CPU implementations and about 756 times over the single-thread version. Despite the AMHA+SCAI version being the most memory-efficient, it is important to notice that its implementation is considerably more complex when compared to the SLIA version.

We also simulated the non-DDE alternans-suppressed version of the model (case B) on the GPU in order to assess the performance impact of a DDE implementation on such environment. The simulation took 3.98 minutes to complete 1 second of electrical activity, representing a performance gain of 7.5% over the SLIA implementation for case D. In terms of memory use, the non-DDE version required about 223 MB of global memory,

while the DDE version with the AMHA+SCAI implementation required an additional 440 MB, for a total of 663 MB of global memory.

4.2.4 *DDE-induced alternans and spiral breakup*

In order to assess the potential of DDEs to produce spiral wave instabilities, we performed wave propagation experiments in 2D using the ten Tusscher *et al.* (2004) model with some of the DDE-based configurations described in Section 4.1.2.1 that were able to induce steady-state alternans in single cell simulations, as the model in its original configurations does not produce breakups when a spiral wave is generated by the stimulus protocol applied in the original manuscript.

The simulations were performed in a 24 cm \times 24 cm uniformly discretized piece of isotropic tissue using the model configuration for epicardial cells. A single stable spiral wave was generated by the S1-S2 stimulation protocol described in ten Tusscher *et al.* (2004), which consisted of: the application of a 1 second stimulus at all nodes located at $x = 0$, which produced a single planar wave propagating in the x-axis direction; and the application of a 2 seconds stimulus at all nodes located in the rectangle defined by $0 \leq x \leq 12$ cm and $0 \leq y \leq 18$ cm after the refractory tail of the first wave reached the middle of the domain. The state of the 17 variables after 10 seconds of simulation was used as initial condition for the subsequent experiments.

We considered four different scenarios for this model: (A) original version with parameter settings for epicardial cells; (B) original version for epicardial cells with DDE implementation for the sodium inactivation gating variables h and j , using $\delta_h = 2$ ms and $\delta_j = 0.5$ ms; (C) original epicardial cell version with DDE implementation for the inactivation gate of the rapid delayed rectifier current (x_{r2}), using $\delta_{x_{r2}} = 15$ ms; and (D) a version that combines the DDE implementations of cases (B) and (C), which corresponds to one of the scenarios where alternans could be induced in single cell experiments (see Fig. 4.17B).

Snapshots of membrane potentials from simulations of all four cases are presented in Fig. 4.26 alongside with the corresponding spiral wave trajectories whenever a single

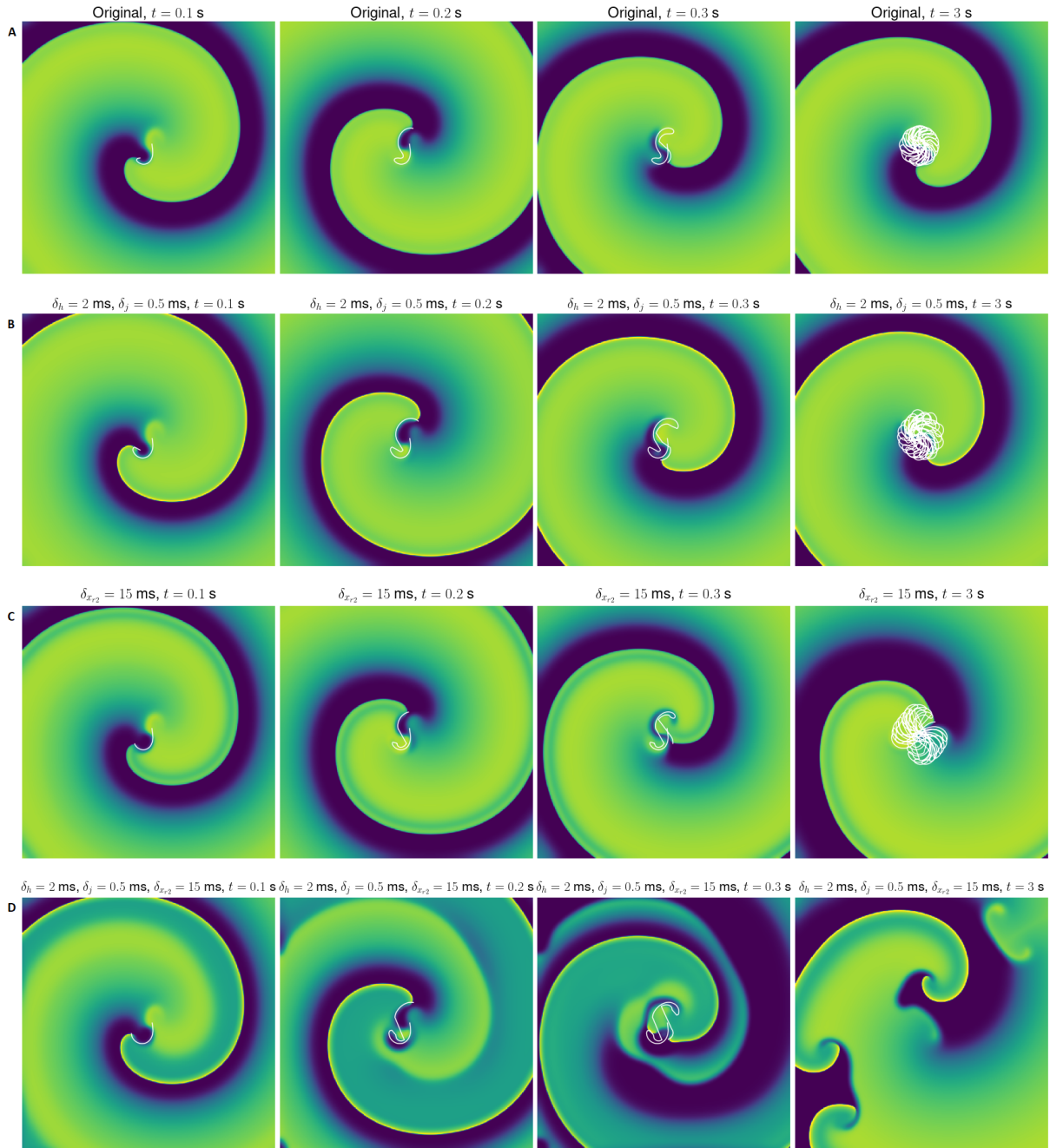


Figure 4.26: Snapshots of membrane potentials from simulations of a $24 \text{ cm} \times 24 \text{ cm}$ tissue using the ten Tusscher *et al.* (2004) model and a stable spiral wave as initial condition, in four different scenarios: (A) the original model for epicardial cells; (B) the model with the h gate delayed by 2 ms and the j gate delayed by 0.5 ms; (C) the model with the x_{r2} gate delayed by 15 ms; and (D) the model with the h gate delayed by 2 ms, the j gate delayed by 0.5 ms, and the x_{r2} gate delayed by 15 ms. The spiral wave tip trajectory is shown in white whenever there is a single spiral wave.

stable spiral wave is present. The spiral wave remains stable in cases A, B, and C, despite modifications to the trajectory and wavelength in cases B and C. In case D, the spiral wave started to breakup at $t = 0.5 \text{ s}$ and subsequent breakups continued to occur even

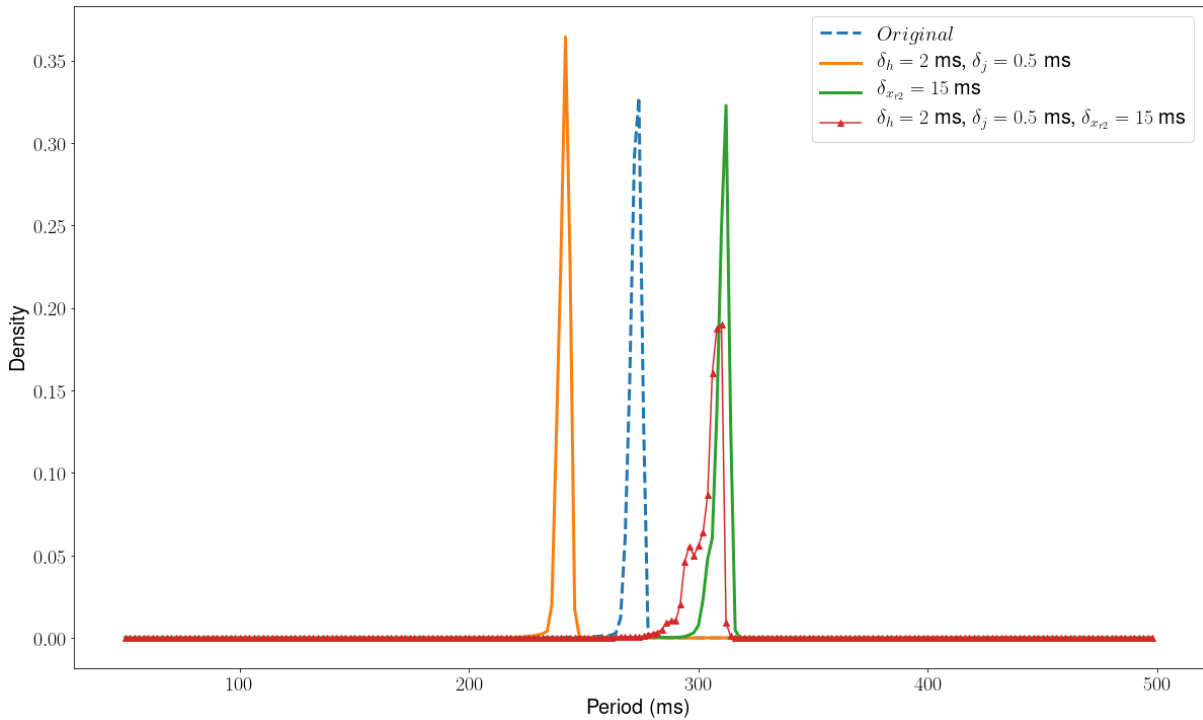


Figure 4.27: Period distributions obtained from simulations of the four scenarios presented in Figure 4.26. The period information was collected from $t = 5$ s to $t = 10$ s of each simulation.

after 10 s of simulation.

In Figure 4.27, we show the period distribution obtained from the entire domain for 5 seconds after the first 5 seconds of simulation of each four scenarios. As previously stated, adding delays to the sodium inactivation gates in the ten Tusscher *et al.* (2004) model shortens the APD, which results in the dominant period being displaced to the left with respect to the original model. On the other hand, delaying the inactivation gate of the rapid delayed rectifier current increases the APD and the wavelength, so the dominant period is displaced to the right with respect to the version with no DDEs. If the sodium inactivation gates are also delayed, the dominant period remains virtually the same, but the period distribution becomes broader, and the spiral waves are destabilized.

5 Discussion

5.1 DDE-induced alternans and spiral wave breakup

The presented results showed that it is possible to induce/enhance arrhythmia-related instabilities in cardiac models by adding discrete delays to Hodgkin-Huxley formulations for ion channels.

Our first experiments with the proposed DDE-based formulation were performed using the Fox *et al.* (2002) model, which naturally exhibits cardiac alternans in its original description. The proposed technique of perturbing Hodgkin-Huxley models with delays proved to be robust by successfully restoring alternans in 6 different alternans-suppressed versions of the Fox *et al.* (2002) model.

The results presented in Section 4.1.1.2 and published in Gomes *et al.* (2017) demonstrated that our findings using the Fox *et al.* (2002) model were not model-specific, since delays could promote alternans in other five HH-based models of cardiac cells. In general, it was possible to initiate alternans by delaying calcium or potassium gates of currents that have a significant influence on the APD. In addition, we observed that alternans only occurred in cases where the delayed gate had its recover impaired by increasing the delay size.

We could also observe that one must be careful when delaying fast sodium current gates since even small delays in the range of 2-5 ms can either produce unphysiological action potential shapes or even impair the initiation of action potentials. For all models tested, 1-2 ms seemed to be a safe upper-bound for delaying sodium gating variables in terms of physiological behavior.

In Section 4.1.2, we investigated two models that are not originally able to reproduce electrical alternans. Giving rise to alternans in those models using DDEs was not as simple as in the previous cases: it was necessary to apply small delays to fast sodium gating variables, which seemed to destabilize the dynamics but not enough to produce

solid steady-state alternans. We had to amplify these instabilities by also adding delays to calcium or potassium gating variables in order to successfully observe alternans. It was also observed that delaying sodium inactivation gates promotes stronger depolarization and shorter APDs, which facilitates the application of faster pacing periods.

Since we were able to induce alternans in single-cell experiments using the ten Tusscher *et al.* (2004) model, we applied one of the successful DDE-based configurations to wave propagation experiments in 2D in order to assess its effects on spiral wave dynamics. By using a stable spiral wave as the initial condition, we were able to destabilize the wave and produce breakups by adding delays to I_{Na} inactivation gates and the I_{Kr} inactivation gate. As shown in Figure 4.27, delaying the sodium inactivation gates allowed the existence of shorter activation periods because of the reduced refractory periods. This behavior is aligned with the conclusions we gathered from single-cell experiments involving delayed sodium inactivation gates.

5.2 Methods for DDE-based tissue simulations

In order to assess the performance of the proposed methods for memory-efficient simulation of DDE-based models, we performed tissue experiments using the Fox *et al.* (2002) model with DDE implementations for the voltage-dependent gating variables of the calcium current I_{Ca} . The preliminary ring experiments presented in Table 4.1 helped to tune the AHMA tolerances in terms of numerical error. The values depend on the sensitivity of the gating variable with respect to the upstroke and the downstroke phases, but using tolerances in the range from 0.5 mV to 1 mV generally provided acceptable results in terms of numerical accuracy.

By performing 2D simulations using a large mesh of about 2.4 million nodes, we could assess the performance of the different memory management implementations for the AHMA. Since differences in terms of memory use and computation time are rather small, the Linked List Implementation should be preferred on CPU-based solvers due to the simplicity of implementation. On the GPU side, linked-lists-based codes can be extremely complex and not likely to provide efficient results, so the SCAI is recommended

when applying the AHMA in this case. The DDE-based tissue simulations using the AHMA were up to 11% slower than the version with no DDEs on the GPU. On the CPU, the penalty in performance for using a DDE-based approach was lower than 5%. In both scenarios, using a 20 ms delay required about 200% of additional memory when the AHMA was applied. This amount of memory dedicated to historical values would be approximately 20-fold greater if a standard DDE solver was applied instead.

5.3 Limitations and future work

In this thesis, we have proposed a new mathematical formulation based on DDEs that can simulate the phenomenon of alternans and of spiral breakup, which are essential in studies of cardiac arrhythmia. The simulations used different cell models and were performed in 0D (cell model), 1D (cable model) and 2D (tissue model) geometries. A natural next step is to test the new formulations and new numerical methods in 3D, especially for whole heart simulations. In addition, in the near future, we intend to improve the numerical methods used here and to perform other studies using DDEs for cardiac modeling, such as to describe calcium handling mechanisms that can lead calcium-driven alternans, and to reproduce other cardiac diseases at the cellular level.

5.3.1 Numerical Methods

During this research, we developed an article describing adaptive-step methods based on the uniformization method (Melamed - Yadin, 1984) for models that impose substantial restrictions on time step size due to stability requirements. These are known as *stiff* models and they usually include Markov formulations for ion channels (Marsh *et al.*, 2012). However, they have not been applied to the DDE-based simulations of this thesis, since the presented experiments were limited to models that only include Hodgkin-Huxley formulations for describing the ion channel dynamics. Our recently submitted article (Gomes *et al.*, 2019b) contains a complete description of these methods that can potentially provide numerical efficiency to future experiments involving DDEs in Markov-

based models. The proposed adaptive technique called ADP GRL1+UNI was up to 350 times faster than the tradition Rush-Larsen method for single-cell simulations.

The here proposed adaptive history management algorithm was mainly based on heuristics developed from previous knowledge about the dynamical properties of an action potential. Another promising approach would be to improve upon the ADP GRL1+UNI method to include numerical step adaptivity for past variables. That would allow memory-efficient DDE-based experiments with stiff models that could include Markov descriptions for ion channels.

5.3.2 DDEs for cardiac models

The present thesis has shown how models that include DDEs can produce complex dynamics by promoting electrical alternans and spiral-wave breakup. The scope of this project was limited to perturbing preexisting Hodgkin-Huxley equations with time delays. Rameh *et al.* (2019) have demonstrated it is possible to replace HH-based equations with a purely DDE-based formulation. Therefore, this is yet another suggestion that DDEs have a potential for replacing the delayed processes that are traditionally described by Markov models for ion channels. Therefore, these possible applications and extensions deserve further investigation.

6 Conclusion

Over 17 million people die of cardiac arrhythmias worldwide. In the emerging era of precision medicine, where treatments and medicaments are to be developed in a personalized fashion, computational models play an essential role. Electrical alternans is an important phenomenon that is closely associated with cardiac arrhythmia. Unfortunately, many modern models of cardiac electrophysiology can not reproduce this phenomenon.

In this thesis, we modified existing modern models of cardiac electrophysiology that could not generate alternans by introducing a new mathematical formulation based on delay differential equations. After extensive studies, we were able to find combinations of parameters of the new modified models that enabled the reproduction of alternans in single-cell simulations. In addition, these studies revealed different mechanisms by which alternans could be generated, such as the interplay of small delays in sodium variables with larger delays in calcium or potassium variables.

However, the new proposed formulation comes at a price. The management of past values of the variables, or history, due to the delay differential equations, poses new challenges to numerical methods. Therefore, in this thesis, we have also proposed and tested different numerical methods to solve the new DDE-based formulations efficiently. The new methods are based on adaptive schemes and were able to decrease memory usage by up to 97%. These enabled us to perform, for the first time, a series of cardiac tissue simulations with DDE-based models using a sizeable two-dimensional mesh with 2.4 million nodes.

Using our new DDE-based formulations and new methods, we were able to reproduce the phenomenon of spiral breakup, a mechanism strongly associated with ventricular fibrillation and sudden cardiac death. These simulations were also performed using a model that could not, before our modifications, reproduce these complex phenomena. We have also studied how the parameters of the new modified models affected the dynamics

of spiral wave, spiral breakup, and chaos.

In the future, further studies will be conducted to understand how the new DDE-based models differ from the traditional ODE-based models. In this way, we will continue to contribute to the development of models that can unravel complex mechanisms that underly fatal cardiac arrhythmias.

Bibliography

- Amanfu, R. K., Saucerman, J. J., 2011. Cardiac models in drug discovery and development: a review. *Critical reviews in biomedical engineering* 39 (5), 379–95.
- Amorim, R. M., dos Santos, R. W., Sep. 2013. Solving the cardiac bidomain equations using graphics processing units. *Journal of Computational Science* 4 (5), 370–376. Available at: <https://doi.org/10.1016/j.jocs.2012.06.007>
- Armstrong, C. M., Bezanilla, F., Nov 1977a. Inactivation of the sodium channel. I. Gating current experiments. *The Journal of general physiology* 70 (5), 549–66.
- Armstrong, C. M., Bezanilla, F., Nov 1977b. Inactivation of the sodium channel. II. Gating current experiments. *The Journal of general physiology* 70 (5), 567–90.
- Bayer, J., Lalani, G., Vigmond, E., Narayan, S., Trayanova, N., Sep. 2016. Mechanisms linking electrical alternans and clinical ventricular arrhythmia in human heart failure. *Heart Rhythm* 13 (9), 1922–1931. Available at: <https://doi.org/10.1016/j.hrthm.2016.05.017>
- Beeler, G. W., Reuter, H., Jun 1977. Reconstruction of the action potential of ventricular myocardial fibres. *The Journal of Physiology* 268 (1), 177–210.
- Bondarenko, V. E., 2014. A Compartmentalized Mathematical Model of the β_1 -Adrenergic Signaling System in Mouse Ventricular Myocytes. *PLOS ONE* 9 (e89113), 01–35.
- Bondarenko, V. E., Szigeti, G. P., Bett, G. C., Kim, S. J., Rasmusson, R. L., 2004. Computer Model of Action Potential of Mouse Ventricular Myocytes. *American Journal of Physiology - Heart and Circulatory Physiology* 287, H1378–H1403.

- Brennan, T., Fink, M., Rodriguez, B., 2009. Multiscale modelling of drug-induced effects on cardiac electrophysiological activity. *European Journal of Pharmaceutical Sciences* 36 (1), 62 – 77.
- Bueno-Orovio, A., Cherry, E. M., Fenton, F. H., Aug. 2008. Minimal model for human ventricular action potentials in tissue. *Journal of Theoretical Biology* 253 (3), 544–560. Available at: <https://doi.org/10.1016/j.jtbi.2008.03.029>
- Byrne, G., Marcotte, C. D., Grigoriev, R. O., Mar. 2015. Exact coherent structures and chaotic dynamics in a model of cardiac tissue. *Chaos: An Interdisciplinary Journal of Nonlinear Science* 25 (3), 033108. Available at: <https://doi.org/10.1063/1.4915143>
- Campos, F. O., 2008. Modelagem computacional da eletrofisiologia cardíaca: O desenvolvimento de um novo modelo para células de camundongos e avaliação de novos esquemas numéricos. Master Thesis, Universidade Federal de Juiz de Fora - Mestrado em modelagem computacional.
- Christini, D. J., Riccio, M. L., Culianu, C. A., Fox, J. J., Karma, A., Gilmour, R. F., Mar 2006. Control of electrical alternans in canine cardiac Purkinje fibers. *Physical review letters* 96 (10), 104101.
- Clancy, C. E., Rudy, Y., 1999. Linking a genetic defect to its cellular phenotype in a cardiac arrhythmia. *Nature* 400, 566–569.
- Clancy, C. E., Zhu, Z. I., Rudy, Y., January 2007. Pharmacogenetics and anti-arrhythmic drug therapy: a theoretical investigation. *American Journal of Physiology - Heart and Circulatory Physiology* 292 (1), H66–H75.
- Commons, W., 2007. Schematic of an action potential. Available at: https://commons.wikimedia.org/wiki/File:Action_potential.svg
- Courtemanche, M., Keener, J. P., Glass, L., feb 1996. A Delay Equation Representation of Pulse Circulation on a Ring in Excitable Media. *SIAM Journal on Applied Mathematics* 56 (1), 119–142. Available at: <http://dx.doi.org/10.1137/S0036139993259337>

- Díaz, M. E., O'Neill, S. C., Eisner, D. A., 2004. Sarcoplasmic Reticulum Calcium Content Fluctuation Is the Key to Cardiac Alternans. *Circulation Research* 94 (5), 650–656.
- Dutta, S., Mincholé, A., Quinn, T. A., Rodriguez, B., Oct. 2017. Electrophysiological properties of computational human ventricular cell action potential models under acute ischemic conditions. *Progress in Biophysics and Molecular Biology* 129, 40–52. Available at: <https://doi.org/10.1016/j.pbiomolbio.2017.02.007>
- Eastman, J., Sass, J., Gomes, J. M., dos Santos, R. W., Cherry, E. M., sep 2016. Using delay differential equations to induce alternans in a model of cardiac electrophysiology. *Journal of Theoretical Biology* 404, 262–272. Available at: <http://dx.doi.org/10.1016/j.jtbi.2016.06.009>
- Echebarria, B., Karma, A., 2002. Spatiotemporal control of cardiac alternans. *Chaos* 12, 923–930.
- Elshrif, M. M., Cherry, E. M., Jan. 2014. A Quantitative Comparison of the Behavior of Human Ventricular Cardiac Electrophysiology Models in Tissue. *PLoS ONE* 9 (1), e84401. Available at: <https://doi.org/10.1371/journal.pone.0084401>
- Fenton, F., Karma, A., Mar. 1998. Vortex dynamics in three-dimensional continuous myocardium with fiber rotation: Filament instability and fibrillation. *Chaos: An Interdisciplinary Journal of Nonlinear Science* 8 (1), 20–47. Available at: <https://doi.org/10.1063/1.166311>
- Fenton, F. H., Cherry, E. M., Hastings, H. M., Evans, S. J., Aug. 2002. Multiple mechanisms of spiral wave breakup in a model of cardiac electrical activity. *Chaos: An Interdisciplinary Journal of Nonlinear Science* 12 (3), 852–892. Available at: <https://doi.org/10.1063/1.1504242>
- FitzHugh, R., 1961. Impulses and Physiological States in Theoretical Models of Nerve Membrane. *Biophysical Journal* 1 (6), 445–466.
- Foulkes, A. J., Biktashev, V. N., Apr 2010. Riding a spiral wave: numerical simulation of

- spiral waves in a comoving frame of reference. *Physical review. E, Statistical, nonlinear, and soft matter physics* 81 (4 Pt 2), 046702.
- Fox, J. J., McHarg, J. L., Gilmour, R. F., oct 2002. Ionic mechanism of electrical alternans. *AJP: Heart and Circulatory Physiology* 282 (2), H516–H530. Available at: <http://dx.doi.org/10.1152/ajpheart.00612.2001>
- Gani, M. O., Ogawa, T., 2014. Alternans and Spiral Breakup in an Excitable Reaction-Diffusion System: A Simulation Study. *International Scholarly Research Notices* 2014, 1–14. Available at: <https://doi.org/10.1155/2014/459675>
- Garfinkel, A., Kim, Y. H., Voroshilovsky, O., Qu, Z., Kil, J. R., Lee, M. H., Karagueuzian, H. S., Weiss, J. N., Chen, P. S., May 2000a. Preventing ventricular fibrillation by flattening cardiac restitution. *Proceedings of the National Academy of Sciences of the United States of America* 97 (11), 6061–6.
- Garfinkel, A., Kim, Y.-H., Voroshilovsky, O., Qu, Z., Kil, J. R., Lee, M.-H., Karagueuzian, H. S., Weiss, J. N., Chen, P.-S., may 2000b. Preventing ventricular fibrillation by flattening cardiac restitution. *Proceedings of the National Academy of Sciences* 97 (11), 6061–6066. Available at: <http://dx.doi.org/10.1073/pnas.090492697>
- Garzón, A., Grigoriev, R. O., Fenton, F. H., oct 2011. Model-based control of cardiac alternans in Purkinje fibers. *Physical Review E* 84 (4). Available at: <http://dx.doi.org/10.1103/PhysRevE.84.041927>
- Göktepe, S., Wong, J., Kuhl, E., Oct. 2009. Atrial and ventricular fibrillation: computational simulation of spiral waves in cardiac tissue. *Archive of Applied Mechanics* 80 (5), 569–580. Available at: <https://doi.org/10.1007/s00419-009-0384-0>
- Goldhaber, J. I., Xie, L.-H., Duong, T., Motter, C., Khuu, K., Weiss, J. N., 2005. Action potential duration restitution and alternans in rabbit ventricular myocytes: the key role of intracellular calcium cycling. *Circulation Research* 96 (4), 459–466.
- Gomes, J. M., dos Santos, R. W., Cherry, E. M., sep 2017. Alternans promotion in cardiac electrophysiology models by delay differential equations. *Chaos: An Interdisciplinary*

- Journal of Nonlinear Science 27 (9), 093915. Available at: <https://doi.org/10.1063/1.4999471>
- Gomes, J. M., Lobosco, M., dos Santos, R. W., Cherry, E. M., Dec. 2019a. Delay differential equation-based models of cardiac tissue: Efficient implementation and effects on spiral-wave dynamics. *Chaos: An Interdisciplinary Journal of Nonlinear Science* 29 (12), 123128. Available at: <https://doi.org/10.1063/1.5128240>
- Gomes, J. M., Oliveira, R. S., Lobosco, M., dos Santos, R. W., sep 2019b. Adaptive-step methods for Markov-based membrane models. *Communications in Nonlinear Science and Numerical Simulation* (paper under review).
- Grandi, E., Pasqualini, F. S., Bers, D. M., Jan. 2010. A novel computational model of the human ventricular action potential and Ca transient. *Journal of Molecular and Cellular Cardiology* 48 (1), 112–121. Available at: <https://doi.org/10.1016/j.yjmcc.2009.09.019>
- Guevara, M. R., Ward, G., Shrier, A., Glass, L., 1984. Electrical alternans and period-doubling bifurcations. *Computational Cardiology* 11, 167–170.
- Hall, J. E., Guyton, A. C., 2006. *Guyton and Hall Textbook of Medical Physiology*, eleventh edition Edition. Saunders/Elsevier.
- Hodgkin, A., Huxley, A., 1952. A quantitative description of membrane current and its application to conduction and excitation in nerve. *The Journal of Physiology* 117 (4), 500.
- Holmes, M. H., 2006. *Introduction to numerical methods in differential equations*. Vol. 52. Springer.
- Karma, A., 1994. Electrical alternans and spiral wave breakup in cardiac tissue. *Chaos* 4 (3), 461. Available at: <http://dx.doi.org/10.1063/1.166024>
- Kazbanov, I. V., ten Tusscher, K. H. W. J., Panfilov, A. V., Feb. 2016. Effects of

- Heterogeneous Diffuse Fibrosis on Arrhythmia Dynamics and Mechanism. *Scientific Reports* 6 (1). Available at: <https://doi.org/10.1038/srep20835>
- Kléber, A. G., Janse, M. J., van Capelle, F. J., Durrer, D., May 1978. Mechanism and time course of S-T and T-Q segment changes during acute regional myocardial ischemia in the pig heart determined by extracellular and intracellular recordings. *Circulation Research* 42 (5), 603–613. Available at: <https://doi.org/10.1161/01.res.42.5.603>
- Krogh-Madsen, T., Karma, A., Riccio, M. L., Jordan, P. N., Christini, D. J., Gilmour, R. F., Jan 2010. Off-site control of repolarization alternans in cardiac fibers. *Physical review. E, Statistical, nonlinear, and soft matter physics* 81, 011915.
- Kwofie, M. A., Chaudhary, A. K., Martins, J. B., Nov. 2011. Association among intracardiac T-wave alternans, ischemia, and spontaneous ventricular arrhythmias after coronary artery occlusion in a canine model. *Translational Research* 158 (5), 265–272. Available at: <https://doi.org/10.1016/j.trsl.2011.07.001>
- Li, P., Rudy, Y., may 2011. A Model of Canine Purkinje Cell Electrophysiology and Ca^{2+} Cycling: Rate Dependence, Triggered Activity, and Comparison to Ventricular Myocytes. *Circulation Research* 109 (1), 71–79. Available at: <http://dx.doi.org/10.1161/CIRCRESAHA.111.246512>
- Luo, C., Rudy, Y., 1991. A model of the ventricular cardiac action potential. Depolarization, repolarization, and their interaction. *Circulation Research* 68 (6), 1501–1526.
- Marsh, M. E., Ziaratgahi, S. T., Spiteri, R. J., 2012. The secrets to the success of the Rush-Larsen method and its generalizations. *IEEE Transactions on Biomedical Engineering Journal* 59 (9), 2506–2515.
- Martin, F. F., 1968. *Computer modeling and simulation*, first Edition. John Wiley and Sons.
- Melamed, B., Yadin, M., 1984. The randomization procedure in the computation of

- cumulative time distributions over discrete state Markov processes. *Operations Research* 32, 929–943.
- Muñoz, L. M., Stockton, J. F., Otani, N. F., Sep 2010. Applications of control theory to the dynamics and propagation of cardiac action potentials. *Annals of biomedical engineering* 38 (9), 2865–76.
- Neic, A., Liebmann, M., Hoetzel, E., Mitchell, L., Vigmond, E. J., Haase, G., Plank, G., Aug 2012. Accelerating cardiac bidomain simulations using graphics processing units. *IEEE transactions on bio-medical engineering* 59 (8), 2281–90.
- Noble, D., Feb 1962. A modification of the Hodgkin–Huxley equations applicable to Purkinje fibre action and pace-maker potentials. *The Journal of physiology* 160, 317–52.
- Nolasco, J. B., Dahlen, R. W., Aug 1968. A graphic method for the study of alternation in cardiac action potentials. *Journal of applied physiology* 25 (2), 191–6.
- NVIDIA, 2016. NVIDIA Tesla P100. Available at: <https://images.nvidia.com/content/pdf/tesla/whitepaper/pascal-architecture-whitepaper.pdf>
- Oliveira, R. S., de Barros, B. G., Gomes, J. M., Lobosco, M., Alonso, S., Bär, M., dos Santos, R. W., 2016. Reactive Interstitial and Reparative Fibrosis as Substrates for Cardiac Ectopic Pacemakers and Reentries. In: *Bioinformatics and Biomedical Engineering*. Springer International Publishing, pp. 346–357. Available at: https://doi.org/10.1007/978-3-319-31744-1_31
- Petersen, W. P., Arbenz, P., 2004. *Introduction to parallel computing*. No. 9. Oxford University Press.
- Potse, M., Dube, B., Richer, J., Vinet, A., Gulrajani, R., Dec. 2006. A Comparison of Monodomain and Bidomain Reaction-Diffusion Models for Action Potential Propagation in the Human Heart. *IEEE Transactions on Biomedical Engineering* 53 (12), 2425–2435. Available at: <https://doi.org/10.1109/tbme.2006.880875>

- Qu, Z., Garfinkel, A., Chen, P. S., Weiss, J. N., Oct 2000. Mechanisms of discordant alternans and induction of reentry in simulated cardiac tissue. *Circulation* 102 (14), 1664–70.
- Qu, Z., Weiss, J. N., Garfinkel, A., 1997. Spatiotemporal Chaos in a Simulated Ring of Cardiac Cells. *Physical Review Letters* 78 (7), 1387–1390.
- Rameh, R. B., Cherry, E. M., dos Santos, R. W., Oct. 2019. Single-variable delay-differential equation approximations of the FitzHugh-Nagumo and Hodgkin-Huxley models. *Communications in Nonlinear Science and Numerical Simulation*, 105066. Available at: <https://doi.org/10.1016/j.cnsns.2019.105066>
- Rappel, W. J., Fenton, F., Karma, A., 2009. Spatiotemporal control of wave instabilities in cardiac tissue. *Phys. Rev. Lett.* 83, 456–459.
- Restrepo, J. G., Karma, A., 2009. Spatiotemporal intracellular calcium dynamics during cardiac alternans. *Chaos* 19 (3), 037115. Available at: <http://dx.doi.org/10.1063/1.3207835>
- Rocha, B. M., Campos, F. O., Amorim, R. M., Plank, G., dos Santos, R. W., Liebmann, M., Haase, G., Dec. 2010. Accelerating cardiac excitation spread simulations using graphics processing units. *Concurrency and Computation: Practice and Experience* 23 (7), 708–720. Available at: <https://doi.org/10.1002/cpe.1683>
- Rudy, Y., Silva, J. R., feb 2006. Computational biology in the study of cardiac ion channels and cell electrophysiology. *Quarterly Reviews of Biophysics* 39 (01), 57. Available at: <https://doi.org/10.1017%2Fs0033583506004227>
- Ruiz-Herrera, A., Oct. 2012. Chaos in delay differential equations with applications in population dynamics. *Discrete and Continuous Dynamical Systems* 33 (4), 1633–1644. Available at: <https://doi.org/10.3934/dcds.2013.33.1633>
- Rush, S., Larsen, H., jul 1978. A Practical Algorithm for Solving Dynamic Membrane Equations. *IEEE Transactions on Biomedical Engineering* BME-25 (4), 389–392. Available at: <http://dx.doi.org/10.1109/TBME.1978.326270>

- Saad, M., Mahmoud, A., Elgendy, I. Y., Conti, C. R., oct 2015. Ranolazine in Cardiac Arrhythmia. *Clinical Cardiology* 39 (3), 170–178. Available at: <https://doi.org/10.1002/clc.22476>
- Sato, D., Bers, D. M., Shiferaw, Y., dec 2013. Formation of Spatially Discordant Alternans Due to Fluctuations and Diffusion of Calcium. *PLoS ONE* 8 (12), e85365. Available at: <http://dx.doi.org/10.1371/journal.pone.0085365>
- Sato, D., Xie, Y., Weiss, J. N., Qu, Z., Garfinkel, A., Sanderson, A. R., Sep 2009. Acceleration of cardiac tissue simulation with graphic processing units. *Medical & biological engineering & computing* 47 (9), 1011–5.
- Seo, D., Ginsburg, G. S., Goldschmidt-Clermont, P. J., 2006. Gene Expression Analysis of Cardiovascular Diseases: Novel Insights Into Biology and Clinical Applications. *Journal of the American College of Cardiology* 48 (2), 227 – 235. Available at: <http://www.sciencedirect.com/science/article/pii/S073510970601134X>
- Shampine, L., Gahinet, P., Mar. 2006. Delay-differential-algebraic equations in control theory. *Applied Numerical Mathematics* 56 (3-4), 574–588. Available at: <https://doi.org/10.1016/j.apnum.2005.04.025>
- Shampine, L., Thompson, S., 2001. Solving ddes in matlab. *Applied Numerical Mathematics* 37 (4), 441–458.
- SUNDNES, J., LINES, G., TVEITO, A., 2002. ODE Solvers for a Stiff System Arising in the Modeling of the Electrical Activity of the Heart. *International Journal of Nonlinear Sciences and Numerical Simulation*. 3 (3).
- ten Tusscher, K. H. W. J., Noble, D., Noble, P. J., Panfilov, A. V., Apr. 2004. A model for human ventricular tissue. *American Journal of Physiology-Heart and Circulatory Physiology* 286 (4), H1573–H1589. Available at: <https://doi.org/10.1152/ajpheart.00794.2003>
- ten Tusscher, K. H. W. J., Panfilov, A. V., may 2006. Alternans and spiral breakup in

- a human ventricular tissue model. *AJP: Heart and Circulatory Physiology* 291 (3), H1088–H1100. Available at: <http://dx.doi.org/10.1152/ajpheart.00109.2006>
- Thompson, R., 2013. Using Delay-Differential Equations for Modeling Calcium Cycling in Cardiac Myocytes. Master Thesis, Rochester Institute of Technology, Rochester, NY.
- Timour, Q., Frassati, D., Descotes, J., Chevalier, P., Christé, G., Chahine, M., 2012. Sudden Death of Cardiac Origin and Psychotropic Drugs. *Frontiers in Pharmacology* 3. Available at: <https://doi.org/10.3389/fphar.2012.00076>
- Tolkacheva, E. G., Schaeffer, D. G., Gauthier, D. J., Krassowska, W., Mar. 2003. Condition for alternans and stability of the 1:1 response pattern in a “memory” model of paced cardiac dynamics. *Physical Review E* 67 (3). Available at: <https://doi.org/10.1103/physreve.67.031904>
- Tung, L., 1972. A Bi-domain Model for Describing Ischemic Myocardial D-C Potentials. Master Thesis, Massachusetts Institute of Technology, Cambridge, MA.
- Tusscher, K. H. W. J. T., Panfilov, A. V., nov 2006. Cell model for efficient simulation of wave propagation in human ventricular tissue under normal and pathological conditions. *Physics in Medicine and Biology* 51 (23), 6141–6156. Available at: <http://dx.doi.org/10.1088/0031-9155/51/23/014>
- Watanabe, M. A., Fenton, F. H., Evans, S. J., Hastings, H. M., Karma, A., Feb 2001. Mechanisms for discordant alternans. *Journal of cardiovascular electrophysiology* 12 (2), 196–206.
- Weiss, J. N., Chen, P.-S., Qu, Z., Karaguruzian, H. S., Lin, S.-F., Garfinkel, A., Mar. 2002. Electrical Restitution and Cardiac Fibrillation. *Journal of Cardiovascular Electrophysiology* 13 (3), 292–295. Available at: <https://doi.org/10.1046/j.1540-8167.2002.00292.x>
- Weiss, J. N., Nivala, M., Garfinkel, A., Qu, Z., Jan. 2011. Alternans and Arrhythmias. *Circulation Research* 108 (1), 98–112. Available at: <https://doi.org/10.1161/circresaha.110.223586>

Wilde, A. A. M., Bezzina, C. R., 2005. Genetics of cardiac arrhythmias. *Heart* 91 (10), 1352–1358. Available at: <http://heart.bmj.com/content/91/10/1352.short>

Wolfrum, M., Yanchuk, S., Hövel, P., Schöll, E., Dec. 2010. Complex dynamics in delay-differential equations with large delay. *The European Physical Journal Special Topics* 191 (1), 91–103. Available at: <https://doi.org/10.1140/epjst/e2010-01343-7>